UC Berkeley
UC Berkeley Electronic Theses and Dissertations

Title
Integrated molecular diagnostic platform

Permalink
https://escholarship.org/uc/item/38d2n8d8

Author
Cho, Byungrae

Publication Date
2017

Peer reviewed|Thesis/dissertation

Integrated molecular diagnostic platform

by

Byungrae Cho

A dissertation submitted in partial satisfaction of the requirement of the

requirements for the degree of

Joint Doctor of Philosophy

with University of California, San Francisco

in

Bioengineering

in the

Graduate division

of the

University of California, Berkeley

Committee in charge:

Professor Luke P. Lee, Chair
Professor Ming C. Wu
Professor Randall J. Lee

Fall 2017

Abstract

Integrated molecular diagnostic platform

by

Byungrae Cho

Joint Doctor of Philosophy in Bioengineering with

University of California, San Francisco

University of California, Berkeley

Professor Luke P. Lee, Chair

Infectious and non-communicable diseases impose a global burden of health on both developing and developed countries despite technological advancements in medicine and healthcare. In this perspective, point-of-care testing (POCT) has been paid attention as an area with enormous potential to solve this problem. Point-of-care molecular diagnostic enables to provide diagnoses from clinical samples to clinicians without wasting time such as sample transporting or sample preprocessing. However, most of nucleic acid diagnostics still are performed in central health facilities because they need top-notch equipment and well-trained personnel. To overcome these difficulties, the emergence of microfluidics has been attracted because of its inherent features including consuming small volume of sample and reagent, precise controllability of laminar flow, short processing time for analysis, and miniaturization of devices.

This dissertation is a part of effort to develop an integrated molecular diagnostic platform for improving global health care and the quality of life. Firstly, we developed a microfluidic device for sample preparation. The purpose of sample preparation is to enrich target cells, remove unnecessary cells, and lyse target cells for nucleic acid detection. The preconcentration and selective capture of cells are demonstrated in the microfluidic device by using porous materials and antibody without any external bulky equipment such as a centrifuge. Then, photonic PCR is presented as a new technology of thermal cycling. When light comes to gold (Au), Au can absorb light efficiently due to its plasmonic-assisted high optical absorption (~ 65% at 450 nm) and quickly release the light energy as a thermal energy. Using this simple principle, we demonstrate the target DNA amplification within 5

minutes on 30 cycles. In addition, a comprehensive heat transfer simulation of the photonic PCR is carried out to improve the performance of the photonic PCR. Simulation of heat transfer model demonstrates the importance of optical absorption of Au and thermal diffusivity of materials on heating and cooling ramping rates. Finally, the development of a new integrated molecular diagnostics is demonstrated for bacterial detection in urine samples.

TABLE OF CONTENTS

CHAPTER 4: ANALYSIS OF HEAT TRANSFER IN PHOTONIC PCR

CHAPTER 5: INTEGRATED MOLECULAR DIAGNOSTIC SYSTEM

CHAPTER 6: FUTURE DIRECTION

ACKNOWLEDGEMENTS

I am grateful to my advisor, Prof. Luke P. Lee for providing opportunities of research in diverse fields and enlarging my perspective. I learned a lot from his passionate attitude to his research. I appreciate his invaluable instruction and supervision. Also, I am thankful to my committee members, Prof. Dorian Liepmann, Prof. Ming Wu, and Prof. Randall Lee, who provided valuable feedback on my research. I would also like to thank my collaborators, Prof. Lee Riley, Dr. Sheila Adams-Sapper, Tiffany Wu, Prof. Niren Murthy, Dr. Santanu Maity, Dr. Giri Vegesna and Dr. Tara deBoer for our NIH project. Furthermore, I am grateful the Bioengineering faculty and staff at the Joint Graduate Group in Bioengineering at University of California, Berkeley and San Francisco.

I am very thankful to the BioPOETS lab members for helping me to grow and supporting my research. Especially I want to thank to my seniors, Dr. SoonGweon Hong, Dr. San Hun Lee, Dr. Jun Ho Son, Dr. Seung-min Park, and Prof. Inhee Choi. I also thank to my fellows Dr. Julian Diaz, Dr. Jonghwan Lee, Minsun Song, Soochan Chung, Dr. Jihwan Song, Dr. Jinho Lee, Dr. Doyeon Bang, and Dr. Qiong Pan. I am thankful to my undergraduates, Priya Bhattacharjee, Jeffrey Feng, and Bowen Wang for their dedicated efforts. I also thank to my friends, John Kim, Hector Neira, Bennett Ng, Philip Kang, Nicole Repina, and Elaine Su.

I am very grateful to my parents, Gwangje Cho and Jungju Yang for endless support and love. Without their dedication, I would not be here. Also, I thank to my parents-in-law, Uirak Kim and Eunja Kim for their support and love. I also thank to my sisters and their family, Kieun Cho, Seungju Lim, Donghyun Lim, Ahyeon Lim, Minjin Cho, Ujae Jin, Hyeonseo Jin and Yujeong Jin. Also, I am grateful to my sister-in-law and her family, Dayoung Kim, Dongcheol Suh, Jaewoo Suh, and Jaei Suh.

Lastly, but most importantly, I really thank to my wife, Nayoung Kim. Her devotion makes me finish my PhD. I always appreciate it and I will pay off my debt on her support during my entire life. Love you all the time.

CHAPTER 1

INTRODUCTION TO POINT-OF-CARE MOLECULAR DIAGNOSTICS

1.1 BACKGROUND AND MOTIVATION

The considerable progress on science and technology has made a great contribution to global human health and quality of life. The pace of biotechnology and medical innovation for the past several decades is incredibly faster than for the previous few hundred years[1]. Life expectancy, for instance, dramatically has increased for the past century due to the conquer against many infectious and parasitic diseases and better living standards - from less than 45 years in 1950 to more than 74 years in 2010[2]. However, despite technological advancements in medicine and healthcare, infectious and noncommunicable diseases still impose a global burden of health on both developing and developed countries[3]. In case of infectious diseases, there were estimated 1.1 million death from human immunodeficiency virus (HIV)-related diseases, approximately 1.4 million people died of Tuberculosis (TB), 1.3 million people of hepatitis, and 0.4 million people of malaria in 2015. Furthermore, in 2015, about 40 million people died due to noncommunicable diseases – cardiovascular diseases (17.7 million deaths), cancer (8.8 million deaths), chronic respiratory disease (3.9 million deaths), and diabetes (1.6 million deaths)[4]. Specifically, in high-income countries, the cause of die is mainly chronic diseases (cardiovascular disease, chronic obstructive pulmonary disease, cancer, diabetes or dementia). However, in low- and middle-income countries, infectious diseases such as lower respiratory infections, diarrheal diseases, HIV/AIDS, TB and malaria are the leading causes of death due to lack of well-equipped central hospitals providing sensitive medical imaging (MRI and CT) and various laboratory tests[5].

To address these issues, the trend of healthcare, especially diagnostics, has dramatically been shifting: from healthcare provider-centered to patient-centered[6]. Diagnostics have played an important role in health care. Diagnostics provide clinicians with appropriate information (such as early detection and monitoring on

progress of diseases) and allow them to make a more accurate decision on the patient. Therefore, timely diagnosis and subsequent treatment is essential in saving lives and cutting health costs. Over the past 50 years, laboratory testing in central hospitals has become high-throughput, automated, and high sensitive and accurate[7]. However, even now, we still have to go to hospital for any kind of diagnosis from simple primary care to complicated medical care such as magnetic resonance imaging (MRI) or computed tomography (CT) scanners. In this sense, diagnostic testing near the patient, called point-of-care testing (POCT), has been paid attention with the development of biomedical technology. POCT enables to provide diagnoses from clinical samples to clinicians without wasting time such as sample transporting or sample preprocessing[8]. In this chapter, I provide an overview of POCT, especially molecular diagnostics, as well as a review of the literature on integrated microfluidic molecular diagnostic system.

1.2   WHAT IS POINT-OF-CARE (POC) DIAGNOSTICS?

If your friend said that she felt a change in her body as she was pregnant, what would you say? Most people would tell her to test with a pregnancy test. Like a pregnancy test, when you fell any symptoms of diseases or changes in body, you can check the results for symptoms or changes with a simple test without visiting a hospital. That is called point-of-care testing (POCT), in-vitro diagnostics (IVD) or point-of-care (POC) diagnostics. It was in ancient Egyptian documents that one of the earliest records on IVD can be discovered[9]. In the Berlin Papyrus, there was a description of pregnancy test. Firstly, when a woman thought she was pregnant by herself, she urinated on wheat and barley seeds for several days. Then, if the wheat grew, it was thought that she had a body. If the barley grew, it was thought that she had a girl. If both didn't grow, she didn't bear at all. Scholars have considered this the first pregnancy test. During the Middle Ages, people tried to diagnose different health conditions from the color of urine. After that, it was not until 1956 that a simple and successful rapid diagnostic testing of rheumatoid arthritis was introduced[10].

As the interest in personal health as well as global health care has increased, there has been an escalated attention in POCT. There have been assorted definitions of point-of-care testing or diagnostics over the past 20 years shown in Table 1.1. Furthermore, in terms of terminology, various words with the same meaning were used. For example, to explain the meaning of point-of-care, authors and professional groups has used their unique words such as bedside testing, near patient test, off-

Table 1.1 Different definitions of POCT over the past 20 years

Definition of POCT	Reference
"Testing at or near the site of patient care whenever the medical care is needed"[11]	Kost, 1995
"The analysis of biochemical parameters at or near the patient's bedside"[12]	St-Louis, 2000
"Testing to produce a result at the point (physical and/or temporal dimension) at which a decision is made on the care of the patient"[13]	Price, 2002
"Integrated systems that can process clinical samples for a number of different types of biomarkers in a variety of settings, such as clinical laboratories, doctors' offices and eventually, at home"[14]	Soper et al., 2006
"A diagnostic test performed near the patient without needing a clinical lab"[15]	Sia et al., 2008
"Decentralized diagnostic analysis, which occurs directly at patients' beds, in operating theatres or outpatient clinics, or at sites of accidents"[16]	Luppa et al., 2011
"Point-of-care (POC) diagnostics, in vitro diagnostic (IVD) tests that do not involve the use of laboratory staff and facilities to provide the result"[15]	Gubala et al., 2012
"POC tests may have the ability to circumvent insufficiencies of traditional diagnostics, allowing patients to receive results and treatment before leaving the clinic or doctor's office."[18]	Gaydos et al., 2014
"Testing that is performed near or at the site of a patient with the result leading to possible change in the care of the patient"[19]	ISO 22870, 2016
"A point of care (POC) test is performed at or near the site where a patient initially encounters the health care system, has a rapid turnaround time (approximately 15 min), and provides actionable information that can lead to a change in patient management"[20]	Kozel et al., 2017

site testing, or decentralized testing. The lack of standardized terminology and a diversity of opinions on definition of POCT show the relatively immature field on both academy and industry. Especially, the mainstream of POCT is changing as the technology has incredibly advanced. In the early period, POCT was considered as just *testing* conducted near the patient. Away from central hospitals, people wanted

Table 1.2 ASSURED criteria of WHO

A = Affordable
S = Sensitive (avoid false negative results)
S = Specific (avoid false positive results)
U = User-friendly (simple to perform, uses non-invasive specimens)
R = Rapid and robust
E = Equipment-free
D = Delivered (accessible to end-users)

to get a result on their suspicious signs at home or local healthcare providers. However, it was still necessary to go to the hospital to diagnose and treat diseases with further detailed tests. On the other hand, recently, POCTs care *point-of-care* (at the place and the time of patient care). Not only do POCTs allow clinicians to test patients rapidly but also to make a clinical decision or change the management of patients. In other words, it is emphasized that POCTs can lead to an expeditious clinical decision.

What are ideally essential features of POCT? The World Health Organization (WHO) in 2004 announced the guidelines for developing POCT devices[21]. The acronym ASSURED (Table 1.2) summarized the ideal characteristics of a diagnostic test. However, nowadays, these criteria rather imposed the restrictions of POCT system and impeded the development of POCT field[22]. As a result, many modified criteria have been suggested[8,23,24]. For example, Pai et al. argued that criteria for POCT should be considered not just on the features of devices but on the diverse circumstances such as users (patients to trained people) and environments (homes, emergency room and hospitals)[24]. They categorized into five distinct settings: homes, communities, clinics, peripheral laboratories and hospitals. Depending on the different settings, the priority features of POCT may differ. At home, POCT should be easy-to-use even if low sensitive or less specific. However, in hospitals, POCT should be highly sensitive and specific in spite of not fully automated.

Recently, new technologies for next-generation POCT were emerged. Paper-based POCTs were emerging as a cost-effective, commercially available, and portable format[25]. Also, as the cell phone penetration has increased, cell phone-based POCTs were paid attention for personalized medicine, real-time monitoring and remote health-care management[26]. Especially, a high-performance camera module of a cell phone can be used for direct quantification of parasites[27], detection of virus[28] and food allergen testing[29]. Coupled with wireless communication, the

remote diagnose system will accelerate. Most recently, there has been a gigantic interest in wearable devices. Also, integrated with cell phones, the advance of wearable devices will make real-time monitoring possible such as multiplex sweat monitoring[30] and long-term cardiac electrophysiology[31].

1.3   POC NUCLEIC ACID TESTING (NAT)

Nucleic acids are the intercellular biomolecules containing genetic information through specific sequences. Thus, nucleic acids are high sensitive and specific biomarkers for infectious and genetic diseases[32]. To detect a small number of specific segments of nucleic acids, it is necessary to generate numerous copies of target nucleic acids. Polymerase chain reaction (PCR), a gold-standard technique of nucleic acid amplification developed by Kary Mullis in 1983[33], enabled to produce thousand millions of copies of nucleic acid in a few hours. Subsequently, demonstration of PCR with a thermostable DNA polymerase[34] opened new doors for various applications such as DNA sequencing[35], gene analysis[36], DNA fingerprinting[37] and NAT for infectious diseases.

In spite of these advances, most of NATs still are performed in central health facilities because they need top-notch equipment and well-trained personnel[38]. Specifically, there are three main steps for nucleic acid assays including sample preparation (cell lysis to extract nucleic acids inside cells, removal of other cell components and concentration of nucleic acids), nucleic acid amplification and detection of amplified target nucleic acids[39]. These steps involve long and complicated processes, which hinders the growth of POC NATs.

To overcome these difficulties, the emergence of microfluidics has been attracted because of its inherent features including consuming small volume of sample and reagent, precise controllability of laminar flow, short processing time for analysis, miniaturization of devices[40]. As a result, coupled with microfluidics, many POC NATs have been developed in both industrial and academic fields.

1.4 CURRENT MICROFLUIDIC POC NAT TECHNOLOGIES

PCR is the most popular and developed nucleic acid amplification techniques because of its simplicity. PCR consists of repeated three steps - denaturation, annealing and extension. Each step needs a different temperature (i.e. 95°C for denaturation, 55°C for annealing and 72°C for extension). Thus, manipulation of

heat is the most important core technology in developing a PCR system. Specifically, to miniaturize a PCR system as a POCT, there are desired conditions such as small
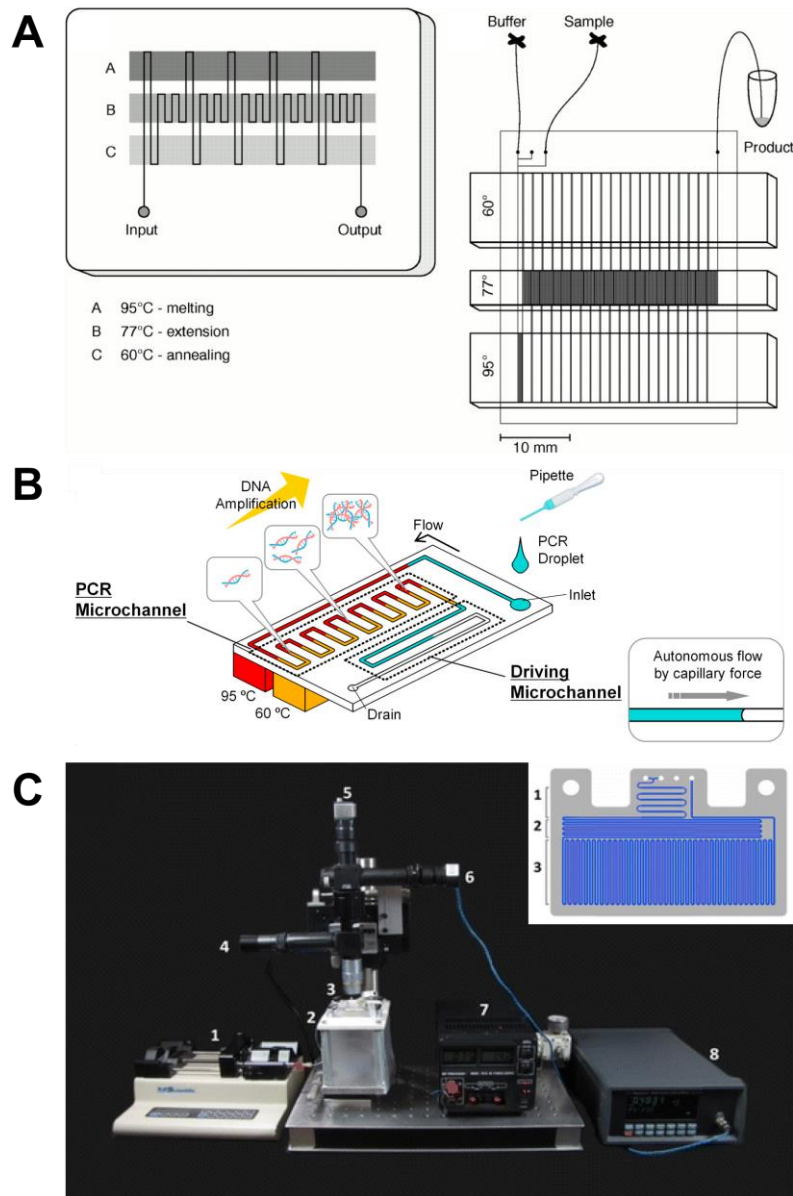
Figure 1.1 Continuous-flow PCR. (A) First demonstration of microfluidic continuous-flow PCR on a chip. Reprinted from ref. 41 with permission from AAAS. (B) Autonomously continuous-flow PCR on a chip due to capillary forces. Reprinted from ref. 50 with permission from Elsevier. (C) An image of set-up (syringe pump, heat blocks, microscope objective lens, a light source, camera, photodetector) for qPCR. Inset: microfluidic device for continuous-flow PCR. Reprinted from ref. 51 with permission from Springer.
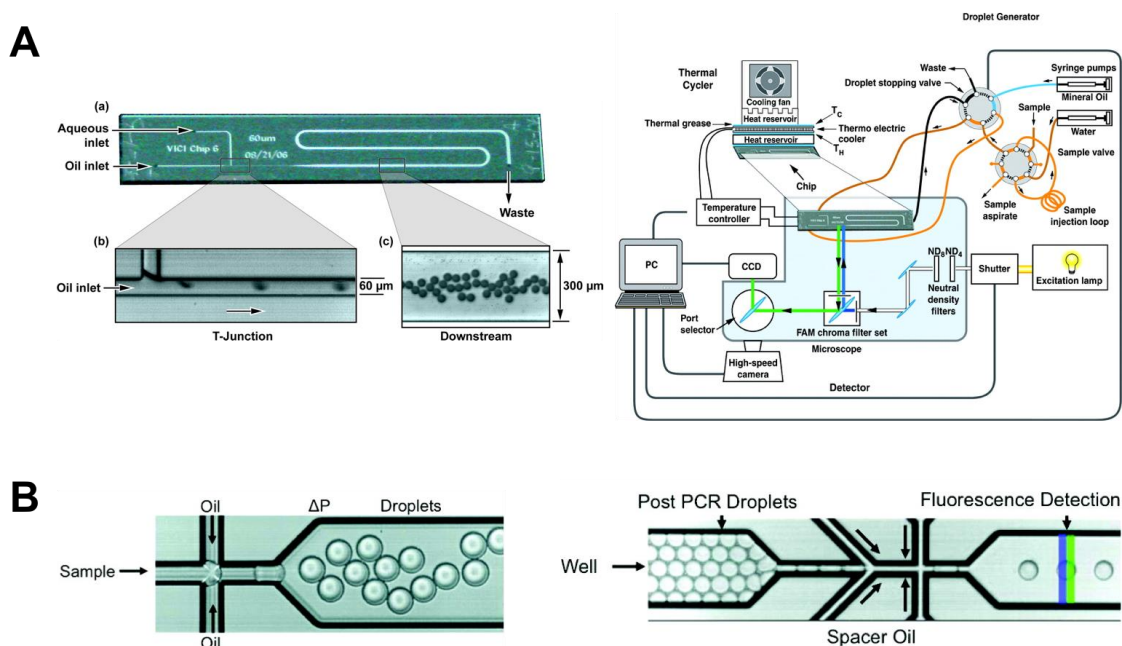
thermal mass, fast heat transfer and rapid temperature changes between PCR steps, which is fit with intrinsic characteristics of microfluidics. In the microfluidic field, obviously, there have been various attempts to execute on-chip PCR for miniaturizing the PCR device. Microfluidic PCR can be classified into three types of microfluidic designs: continuous-flow PCR, microfluidic droplet PCR, and reaction chamber based PCR.

Continuous-flow PCR is the method that demonstrated microfluidic PCR on a chip for the first time (Fig. 1.1 A)[41]. Generally, continuous-flow PCR consists of a single microfluidic channel and three fixed temperature zones for denaturation, annealing and extension. A microfluidic channel is located on top of three temperature zones. The temperature of sample is close to that of each temperature zone during sample flows through the zones repeatedly. Due to small thermal mass of sample in microfluidic channel, rapid temperature change of sample is possible and total PCR time can be also quite reduced. In addition, the reaction volume of sample is also flexible depending on channel size. For these reasons, there have been many research studies and improvements of continuous-flow PCR[42–49]. Tachibana et al. built an autonomously continuous-flow PCR platform, which a sample flew through microchannel without any external equipment due to capillary forces (Fig. 1.1 B)[50]. Recently, a real-time fluorescence-based PCR system with a continuous-flow device was demonstrated (Fig. 1.1 C)[51]. However, continuous-flow PCR poses several drawbacks: 1) Microbubble are easily produced in microchannels when the sample is heated. 2) The flow of sample through microchannels is difficult to control. Thus, PCR protocol is not flexible. 3) Three different temperature zones must be constant, which needs much energy to run PCR.

Microfluidic droplet PCR uses small droplets (a few pL to nL) as individual PCR chamber surrounded by oil. Droplets of samples are generated in microchannels due to high shear stress when sample meets the second immiscible liquid, oil. Then, many droplets of sample in oil experience thermocycling and the fluorescent signals of droplets are detected. When the number of target molecules is smaller than the number of droplets, zero or one target molecule is enclosed in a single droplet statistically. Furthermore, each droplet is independent and isolated reaction, which prevents cross-contamination. For these reasons, microfluidic droplet PCR has been utilized as a PCR platform for single molecule detection in the last 10 years. In 2007, droplet-based PCR on a chip was demonstrated for the first time (Fig. 1.2 A)[52]. In this paper, quantitative PCR (qPCR) amplification was carried out with fluorescent detection even if the size of droplet was not uniform (10 to 20 pL). In addition, the possibility of droplet digital PCR (ddPCR) was showed. After this feasibility, microfluidic ddPCR has been applied for pathogen

detection[53,54], copy number variation[55,56], microRNA detection for caner[57,58], next-generation DNA sequencing[59,60], and single cell gene expression[61,62]. However, droplets sometimes break up during thermal cycling or sample transfer due to liquid surfaces, which is unable to obtain accurate results. In addition, it requires several hours for analysis because of at least tens of thousands of droplets. Lastly, to generate droplets in microchannels, more than two syringe pumps are required. Collectively, microfluidic droplet PCR is a promising technology but is somewhat complicated for POCT.

Reaction chamber based PCR is an appealing substitution for microfluidic droplet PCR. Reaction chamber based PCR is similar of the conventional PCR but the size of chambers is much smaller than that of conventional PCR, which is better for sensitivity, specificity and quantification[63]. There are mainly two types of devices: microwell based PCR and microfluidic channel based PCR. Microwell

Figure 1.2 Microfluidic droplet PCR. (A) First demonstration of droplet PCR on a chip. left: The design of the microfluidic device generating droplets with T-shape channels. right: A schematic of equipment for operating microfluidic droplet PCR and detection system. Reprinted with permission from ref. 52. Copyright (2007) American Chemical Society. (B) Droplet digital PCR on a chip. left: generation of droplets in a cross-junction microchannel. right: Fluorescent detection of each droplet for analyzing of digital PCR after bench-top thermocycling. Reprinted with permission from ref. 55. Copyright (2011) American Chemical Society.
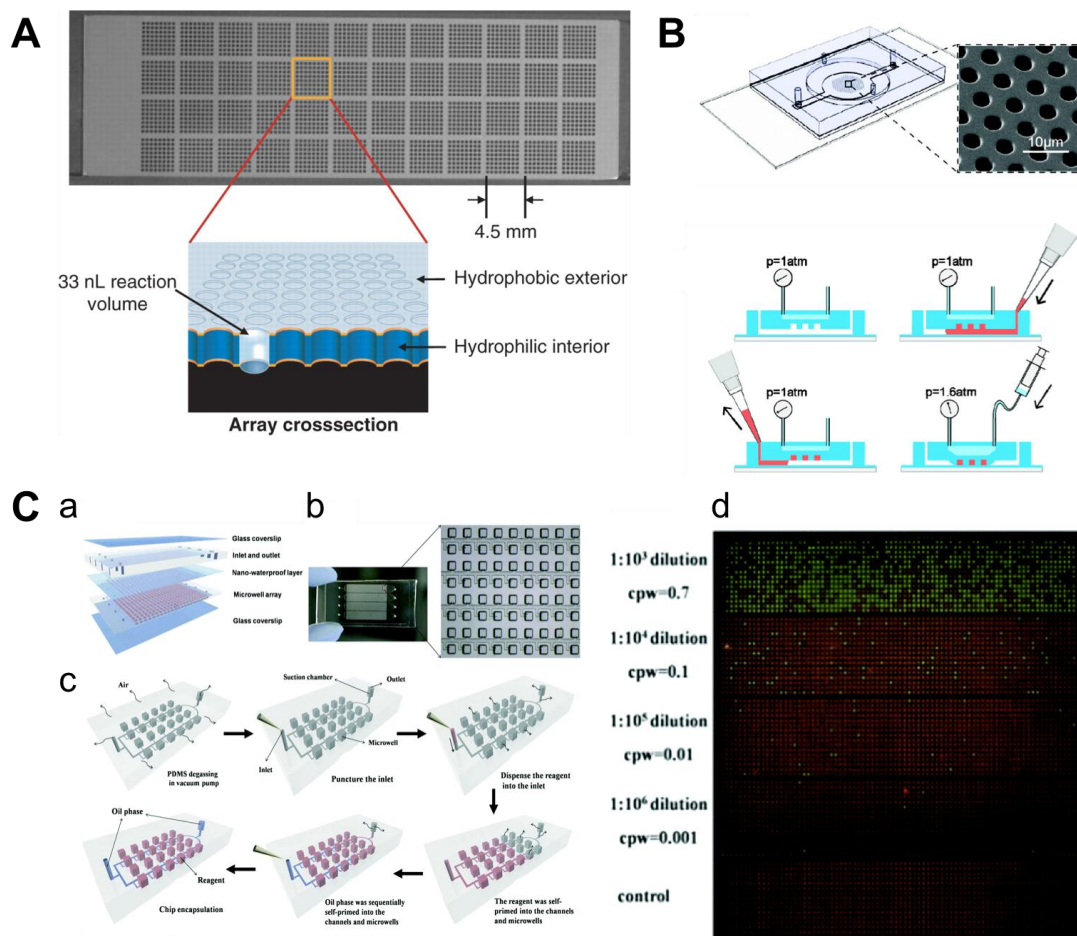
Figure 1.3 Reaction chamber based PCR. (A) A top-view of 3072 PCR nano-reactors made of stainless steel plate. Inside each hole, PEG was deposited to make its surface hydrophilic. Top and bottom surfaces of the plate were turned into hydrophobic using heptadecafluoretriethoxysilane. Reprinted from ref. 64 with permission from Oxford University Press. (B) Microfluidic channel based femtoliter dPCR. Top: An image of the PDMS based microfluidic device. The volume of each microwell is 36 ± 2 fL (3.3 ± 0.1 μm in diameter and 4.2 ± 0.1 μm deep). Bottom: the operation of the device. The sample was loaded to fill all the microwells. Then, pressurized water in the top chamber pushed the middle layer of PDMS to seal, separate all microwells. Reprinted with permission from ref. 65. Copyright (2012) American Chemical Society. (C) Self-priming compartmentalization (SPC) microfluidic PCR chips. The volume of each microwell is 5.625 nL. Solution was loaded, followed by loading of oil. It autonomously flew into the device due to the pressure difference between the device and its surroundings. Reprinted with permission from ref. 66. Copyright (2012 from The Royal Society of Chemistry.

based PCR are carried out in a solid chip that has dense micro-holes. After PCR, fluorescent image of the device is used for analysis. Physically isolated microwells between neighboring wells prevent the risk of cross-contamination, which means the reduced possibility of false-positive results. Morrison et al. demonstrated qPCR of 3072 microwells (diameter: 320 µm) in a microscope slide with the equivalent accuracy and dynamic range of 384 well plate[64] (Fig. 1.3 A). The inner surface of each hole was chemically treated as a hydrophilic surface and the exterior surface of the plate was treated as a hydrophobic surface. Thus, the solution was easy to move and stay inside the hole. This concept has been commercialized in 2013 by Thermofisher. Other type is microfluidic channel based PCR. A device consists of a microfluidic channel and thousands of micro-size chambers in series. Sample solution comes in a microfluidic channel and disperses uniformly into the chambers. Then, immiscible liquid (i.e. oil) fills in a microfluidic channel only, separating many chambers. Men et al. demonstrated digital PCR (dPCR) in an array of 82,000 wells with a volume of 33 fL[65] (Fig. 1.3 B). Water layer was used for prevention of evaporation of sample during thermocycling and compartmentation of reaction wells, which avoids the need of oil for compartmentation. Zhu et al. showed pump-free microchannel-based dPCR for lung cancer diagnostics[66] (Fig. 1.3 C). In a PDMS device, the gas solubility of PDMS produces a pressure difference between the chip and its surroundings to suck test solutions into the microfluidic channels and reaction chambers.

1.5 UNMET CHALLENGES FOR POC NAT

Integration of Sample Preparation

In the previous section, we discussed microfluidic NAT technologies which is able to widely used for POCT currently. However, only few of commercialized microfluidic POC NATs have been launched. One of major bottlenecks is the integration of sample preparation into NAT. Therefore, many solutions for the problem of sample preparation have been proposed. For example, the fully integrated microfluidic chip reported by Liu et al. included on-chip cell preparation, microfluidic mixers, PCR amplification and DNA microarray detection[67]. However, this platform was too complicated to be used at POC setting because of the need of several valves and pumps. Czilwik et al. demonstrated a centrifugal platform including sample preparation, PCR pre-amplification and nested PCR for bacterial detection[68]. Complex sample preparation steps were processed by only one centrifugal force with different rotation speeds. Although its superior performance, the centrifugal device has to give up its portability due to rotation system. In addition,

the fluorescent detection, which needs bulky optical system, makes the centrifugal system more far from portability. Cai et al. exploited dielectrophoretic forces to capture bacteria from diluted whole blood sample and detected them inside a chamber of microfluidic device using on-chip PCR[69]. However, the flow rate of sample had to be slow due to weak of dielectrophoresis. Also, conductive solution was needed to generate dielectrophoretic force.

In summary, sample preparation is an integral step for sample-to-answer POC NAT. However, sample preparation processes are different depending on the sample type (i.e. saliva, blood, urine, and water)[70]. In the case of whole blood, red blood cells (RBCs) should be removed because intercellular components of RBCs deteriorate a PCR reaction. NAT for urine or water sample necessitates sample enrichments due to low concentration of analytes. Hence, it is necessary to develop specialized integrated POC NAT system according to a specific sample type rather than a universal purpose system.

High Power Consumption

High power consumption on operating PCR system is another barrier to POCT[71]. PCR is a process in which target DNA increases exponentially while repeating high and low temperatures (i.e. 95 °C and 60 °C) so it needs a high-power thermal system. Peltier-based thermal systems have been widely used in microsystem because of its controllability, rapid thermal response and simplicity[72–74]. However, due to low energy efficiency, the Peltier-based thermal system requires a lot of energy. Also, the Peltier-based system should increase not only the temperature of the sample solution but also the microfluidic device. So, many ways to increase only the temperature of the sample solution have been proposed. Shaw et al. employed microwave to heat the solution with low power (~500 mW) and demonstrated an integrated microfluidic PCR[75]. Also, Because the feature of water absorbing infrared light, infrared heating for PCR has been investigated. For example, Saunders et al. demonstrated RT-qPCR of 1-μm samples for 1 hour using a 700 mW 1450 nm infrared laser diode[76]. Lounsbury et al. presented an integrated sample-to-answer microdevice using IR ramp under 45 minutes[77].

Collectively, high energy consumption is indispensable for PCR. Although the gold-standard method of nucleic acid amplification is PCR due to the high sensitive and reliability, it is difficult to apply to POCT applications. Conventional thermocyclers should heat up and cool down, not only the PCR solution but also the whole devices, which leads to bulky and complicated equipment and a long process time. Coupled with microfluidics, POC PCR system has been improved due to small

thermal mass of samples. Many innovative heating methods such as IR heating, microwave have been proposed, but most of them still required large and complicated instruments, which is not suitable for POCT.

1.6 ORGANIZATION OF DISSERTATION

Firstly, we developed microfluidic device for sample preparation. The purpose of sample preparation is to enrich target cells, remove unnecessary cells, and lyse cells for nucleic acid detection. The preconcentration and selective capture of cells are demonstrated in the microfluidic device by using porous materials and antibody without any external bulky equipment such as a centrifuge. Then, photonic PCR is presented as a new technology of thermal cycling. When light comes to gold (Au), Au can absorb light efficiently due to its plasmonic-assisted high optical absorption (~ 65% at 450 nm) and quickly release the light energy as a thermal energy. Using this simple principle, we demonstrate the target DNA amplification within 5 minutes on 30 cycles. In addition, a comprehensive heat transfer simulation of the photonic PCR is carried out to improve the performance of the photonic PCR. Simulation of heat transfer model demonstrates the importance of optical absorption of Au and thermal diffusivity of materials on heating and cooling ramping rates. Finally, the development of a new integrated molecular diagnostics is demonstrated for bacterial detection in urine samples.

1.7 REFERENCES

1. Sharma, S., Zapatero-Rodríguez, J., Estrela, P. & O'Kennedy, R. Point-of-Care diagnostics in low resource settings: Present status and future role of microfluidics. Biosensors 5, 577–601 (2015).
2. World Health Organization. Global Health and Aging. 1–26 (2011). at <http://www.who.int/ageing/publications/global_health/en/>
3. World Trade Organization, World Intellectual Property Organization & World Health Organization. Promoting Access to Medical Technologies and Innovation. 1–252 (2013). at <https://www.wto.org/english/tratop_e/trips_e/trilatweb_e/trilat_web_13_e.htm>
4. World Health Organization. World health statistics 2017: monitoring health for the SDGs, Sustainable Development Goals. 1–103 (2017). at <http://www.who.int/gho/publications/world_health_statistics/2017/en/>
5. Stevens, P. Diseases of poverty and the 90/10 gap. 16 (2004). at <http://www.who.int/entity/intellectualproperty/submissions/en/InternationalPolicyNetwork.pdf>
6. Epstein, R. M. & Street, R. L. The values and value of patient-centered care. Annals of Family Medicine 9, 100–103 (2011).

7. Abel, G. Current status and future prospects of point-of-care testing around the globe. Expert Rev. Mol. Diagn. 15, 853–855 (2015).

8. Drain, P. K. et al. Diagnostic point-of-care tests in resource-limited settings. Lancet Infect. Dis. 14, 239–249 (2014).

9. A Timeline of Pregnancy Testing. at <https://history.nih.gov/exhibits/thinblueline/timeline.html>

10. Singer, J. M. & Plotz, C. M. The latex fixation test I. Application to the serologic diagnosis of rheumatoid arthritis. Am. J. Med. 21, 888–892 (1956).

11. Kost, G. J. Guidelines for point-of-care testing: Improving patient outcomes. American Journal of Clinical Pathology 104, (1995).

12. St-Louis, P. Status of point-of-care testing: Promise, realities, and possibilities. Clin. Biochem. 33, 427–440 (2000).

13. Price, C. P. Point of care testing: potential for tracking disease management outcomes. Dis. Manag. Heal. Outcomes 10, 749–761 13p (2002).

14. Soper, S. A. et al. Point-of-care biosensor systems for cancer diagnostics/prognostics. in Biosensors and Bioelectronics 21, 1932–1942 (2006).

15. Sia, S. K. & Kricka, L. J. Microfluidics and point-of-care testing. Lab Chip 8, 1982 (2008).

16. Luppa, P. B., Müller, C., Schlichtiger, A. & Schlebusch, H. Point-of-care testing (POCT): Current techniques and future perspectives. TrAC - Trends in Analytical Chemistry 30, 887–898 (2011).

17. Gubala, V., Harris, L. F., Ricco, A. J., Tan, M. X. & Williams, D. E. Point of care diagnostics: Status and future. Analytical Chemistry 84, 487–515 (2012).

18. Gaydos, C. & Hardick, J. Point of care diagnostics for sexually transmitted infections: perspectives and advances. Expert Rev. Anti. Infect. Ther. 12, 657–672 (2014).

19. ISO (International Organization for Standardization). ISO 22870:2016 Point-of-care testing (POCT) - Requirements for quality and competence. (2016). at <https://www.iso.org/obp/ui/#iso:std:iso:22870:ed-2:v1:en>

20. Kozel, T. R. & Burnham-Marusich, A. R. Point of Care Testing for Infectious Diseases -- Past, Present and Future. J. Clin. Microbiol. JCM.00476-17 (2017). doi:10.1128/JCM.00476-17

21. Kettler, H., White, K. & Hawkes, S. Mapping the landscape of diagnostics for sexually transmitted infections: Key findings and recommandations. WHO 1–44 (2004). at <http://www.who.int/tdr/publications/tdr-research-publications/mapping-landscape-sti/en/index.html>

22. St John, A. & Price, C. P. Existing and Emerging Technologies for Point-of-Care Testing. Clin Biochem Rev 35, 155–167 (2014).

23. Hsieh, Y. H. et al. What qualities are most important to making a point of care test desirable for clinicians and others offering sexually transmitted infection testing? PLoS One 6, (2011).

24. Pai, N. P., Vadnais, C., Denkinger, C., Engel, N. & Pai, M. Point-of-Care Testing for Infectious Diseases: Diversity, Complexity, and Barriers in Low- And Middle-Income Countries. PLoS Med. 9, (2012).

25. Martinez, A. W., Phillips, S. T., Butte, M. J. & Whitesides, G. M. Patterned paper as a platform for inexpensive, low-volume, portable bioassays. Angew. Chemie - Int. Ed. 46, 1318–1320 (2007).

26. Vashist, S. K., Luppa, P. B., Yeo, L. Y., Ozcan, A. & Luong, J. H. T. Emerging Technologies for Next-Generation Point-of-Care Testing. Trends in Biotechnology 33, 692–705 (2015).

27. D'Ambrosio, M. V. et al. Point-of-care quantification of blood-borne filarial parasites with a mobile phone microscope. Sci. Transl. Med. 7, 286re4-286re4 (2015).

28. Wei, Q. et al. Fluorescent imaging of single nanoparticles and viruses on a smart phone. ACS Nano 7, 9147–9155 (2013).

29. Coskun, A. F. et al. A personalized food allergen testing platform on a cellphone. Lab Chip 13, 636–640 (2013).

30. Gao, W. et al. Fully integrated wearable sensor arrays for multiplexed in situ perspiration analysis. Nature 529, 509–514 (2016).

31. Fang, H. et al. Capacitively coupled arrays of multiplexed flexible silicon transistors for long-term cardiac electrophysiology. Nat. Biomed. Eng. 1, 38 (2017).

32. Craw, P. & Balachandran, W. Isothermal nucleic acid amplification technologies for point-of-care diagnostics: a critical review. Lab Chip 12, 2469 (2012).

33. Mullis, K. B. Process for amplifying nucleic acids. US Pat. App. 12 (1985). at <http://www.google.com/patents/US20110059868>

34. Saiki, R. K. et al. Primer-Directed Enzymatic Amplification of DNA With a Thermostable DNA-Polymerase. Science 239, 487–491 (1988).

35. Shendure, J. & Ji, H. Next-generation DNA sequencing. Nat. Biotechnol. 26, 1135–1145 (2008).

36. Giulietti, A. et al. An Overview of Real-Time Quantitative PCR: Applications to Quantify Cytokine Gene Expression. Methods 25, 386–401 (2001).

37. Vos, P. et al. AFLP: A new technique for DNA fingerprinting. Nucleic Acids Res. 23, 4407–4414 (1995).

38. Niemz, A., Ferguson, T. M. & Boyle, D. S. Point-of-care nucleic acid testing for infectious diseases. Trends in Biotechnology 29, 240–250 (2011).

39. Ebara, M. Biomaterials Nanoarchitectonics. Biomaterials Nanoarchitectonics (2016). doi:10.1016/C2014-0-02556-7

40. Whitesides, G. M. The origins and the future of microfluidics. Nature 442, 368–373 (2006).

41. Kopp, M. U. Chemical Amplification: Continuous-Flow PCR on a Chip. Science (80-.). 280, 1046–1048 (1998).

42. Sun, K., Yamaguchi, A., Ishida, Y., Matsuo, S. & Misawa, H. A heater-integrated transparent microchannel chip for continuous-flow PCR. Sensors Actuators, B Chem. 84, 283–289 (2002).

43. Hashimoto, M. et al. Rapid PCR in a continuous flow device. Lab Chip 4, 638–45 (2004).

44. Kim, J. A. et al. Fabrication and characterization of a PDMS-glass hybrid continuous-flow PCR chip. in Biochemical Engineering Journal 29, 91–97 (2006).

45. Crews, N., Wittwer, C. & Gale, B. Continuous-flow thermal gradient PCR. Biomed. Microdevices 10, 187–195 (2008).
46. Li, Y., Zhang, C. & Xing, D. Fast identification of foodborne pathogenic viruses using continuous-flow reverse transcription-PCR with fluorescence detection. Microfluid. Nanofluidics 10, 367–380 (2011).
47. Jiang, L. et al. Solar thermal polymerase chain reaction for smartphone-assisted molecular diagnostics. Sci. Rep. 4, 4137 (2014).
48. Moschou, D. et al. All-plastic, low-power, disposable, continuous-flow PCR chip with integrated microheaters for rapid DNA amplification. Sensors Actuators, B Chem. 199, 470–478 (2014).
49. Shu, B., Zhang, C. & Xing, D. A Handheld Flow Genetic Analysis System (FGAS): Towards Rapid, Sensitive, Quantitative, Multiplex Molecular Diagnosis at the Point-of-Care Level. Lab Chip 15, 2597–2605 (2015).
50. Tachibana, H. et al. On-chip quantitative detection of pathogen genes by autonomous microfluidic PCR platform. Biosens. Bioelectron. 74, 725–730 (2015).
51. Fernández-Carballo, B. L. et al. Low-cost, real-time, continuous flow PCR system for pathogen detection. Biomed. Microdevices 18, (2016).
52. Beer, N. R. et al. On-chip, real-time, single-copy polymerase chain reaction in picoliter droplets. Anal. Chem. 79, 8471–8475 (2007).
53. Kang, D.-K. et al. Rapid detection of single bacteria in unprocessed blood using Integrated Comprehensive Droplet Digital Detection. Nat. Commun. 5, 5427 (2014).
54. Strain, M. C. et al. Highly Precise Measurement of HIV DNA by Droplet Digital PCR. PLoS One 8, (2013).
55. Hindson, B. J. et al. High-throughput droplet digital PCR system for absolute quantitation of DNA copy number. Anal. Chem. 83, 8604–8610 (2011).
56. Pinheiro, L. B. et al. Evaluation of a droplet digital polymerase chain reaction format for DNA copy number quantification. Anal. Chem. 84, 1003–1011 (2012).
57. Hindson, C. M. et al. Absolute quantification by droplet digital PCR versus analog real-time PCR. Nat. Methods 10, 1003–5 (2013).
58. Ma, J., Li, N., Guarnera, M. & Jiang, F. Quantification of plasma miRNAs by digital PCR for cancer diagnosis. Biomark. Insights 8, 127–136 (2013).
59. Eastburn, D. J. et al. Microfluidic droplet enrichment for targeted sequencing. Nucleic Acids Res. 43, e86 (2015).
60. Oxnard, G. R. et al. Noninvasive detection of response and resistance in egfrmutant lung cancer using quantitative next-generation genotyping of cell-free plasma DNA. Clin. Cancer Res. 20, 1698–1705 (2014).
61. Klein, A. M. et al. Droplet barcoding for single-cell transcriptomics applied to embryonic stem cells. Cell 161, 1187–1201 (2015).
62. Brouzes, E. et al. Droplet microfluidic technology for single-cell high-throughput screening. Proc. Natl. Acad. Sci. 106, 14195–14200 (2009).
63. Cao, L. et al. Advances in digital polymerase chain reaction (dPCR) and its emerging biomedical applications. Biosensors and Bioelectronics 90, 459–474 (2017).
64. Morrison, T. et al. Nanoliter high throughput quantitative PCR. Nucleic Acids Res.

34, (2006).

65.   Men, Y. et al. Digital polymerase chain reaction in an array of femtoliter polydimethylsiloxane microreactors. Anal. Chem. 84, 4262–4266 (2012).

66.   Zhu, Q. et al. Digital PCR on an integrated self-priming compartmentalization chip. Lab Chip 14, 1176–85 (2014).

67.   Liu, R. H., Yang, J., Lenigk, R., Bonanno, J. & Grodzinski, P. Self-Contained, Fully Integrated Biochip for Sample Preparation, Polymerase Chain Reaction Amplification, and DNA Microarray Detection. Anal. Chem. 76, 1824–1831 (2004).

68.   Czilwik, G. et al. Rapid and fully automated bacterial pathogen detection on a centrifugal-microfluidic LabDisk using highly sensitive nested PCR with integrated sample preparation. Lab Chip 15, 3749–3759 (2015).

69.   Cai, D., Xiao, M., Xu, P., Xu, Y. & Du, W. An Integrated Microfluidic Device Utilizing Dielectrophoresis and Multiplex Array PCR for Point-of-Care Detection of Pathogens. Lab Chip 14, 3917–3924 (2014).

70.   Cui, F., Rhee, M., Singh, A. & Tripathi, A. Microfluidic Sample Preparation for Medical Diagnostics. Annu. Rev. Biomed. Eng. 17, 267–86 (2015).

71.   Jung, W., Han, J., Choi, J. W. & Ahn, C. H. Point-of-care testing (POCT) diagnostic systems using microfluidic lab-on-a-chip technologies. Microelectronic Engineering 132, 46–57 (2014).

72.   Khandurina, J. et al. Integrated system for rapid PCR-based DNA analysis in microfluidic devices. Anal. Chem. 72, 2995–3000 (2000).

73.   Yang, J. et al. High sensitivity PCR assay in plastic micro reactors. Lab Chip 2, 179–187 (2002).

74.   Maltezos, G. et al. Exploring the limits of ultrafast polymerase chain reaction using liquid for thermal heat exchange: A proof of principle. Appl. Phys. Lett. 97, (2010).

75.   Shaw, K. J. et al. Rapid PCR amplification using a microfluidic device with integrated microwave heating and air impingement cooling. Lab Chip 10, 1725–1728 (2010).

76.   Saunders, D. C. et al. Rapid, quantitative, reverse transcription PCR in a polymer microfluidic chip. Biosens. Bioelectron. 44, 222–8 (2013).

77.   Lounsbury, J. a et al. From sample to PCR product in under 45 minutes: a polymeric integrated microdevice for clinical and forensic DNA analysis. Lab Chip 13, 1384–93 (2013).

CHAPTER 2

SAMPLE PREPARATION FOR BACTERIAL ANALYSIS

In this capture, we presented a microfluidic device that concentrates and separates bacteria selectively with specific antibody in a continuous flow as shown
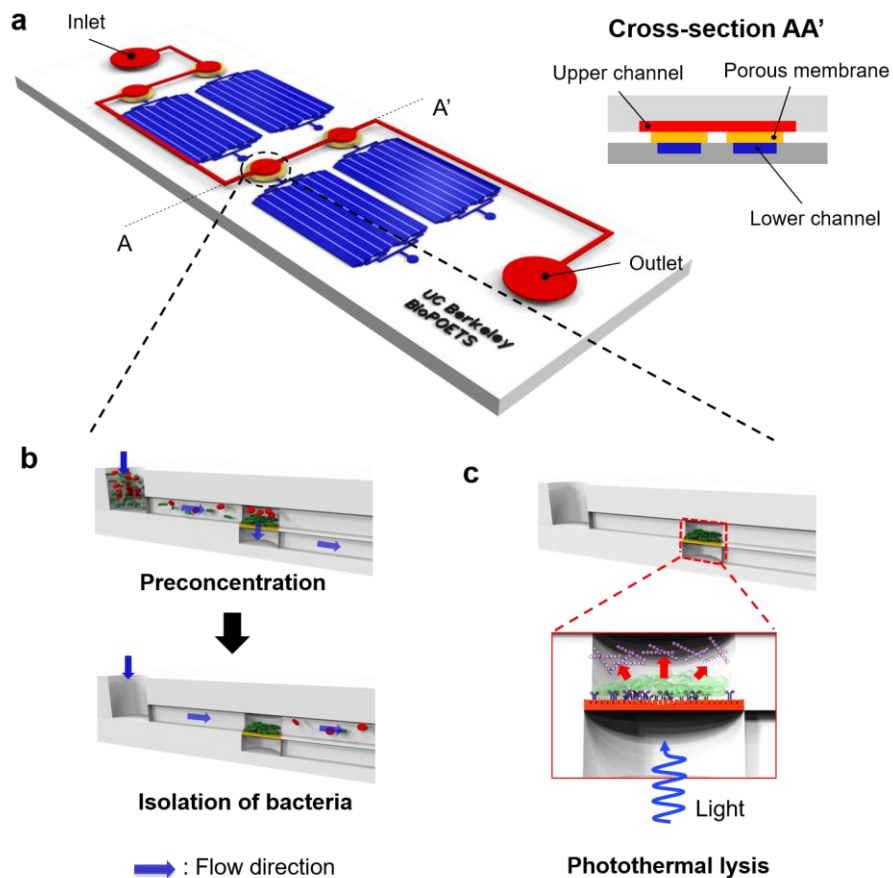

Figure 2.1 Overview of a microfluidic device for sample preparation (a) Schematic of the microfluidic device. It consists of top and lower channels and a porous membrane. (b) Preconcentration and isolation of bacteria by controlling the flow direction in the microchannel. (c) Photothermal lysis of bacteria for further analysis.

in Fig 2.1. Theoretical models were developed to predict velocity profile associated with the velocity through a porous wall.   Then, we demonstrated a two different lysis methods in the microfluidic device.

2.1 ANALYTICAL SOLUTION OF FLOW WITH ONE POROUS WALL IN MICROCHANNEL FOR ENRICHMENT OF BACTERIA ON A CHIP

In this chapter, we start by seeking a similarity solution of separable form for the power-law fluid flow problem in a porous walled geometry as a basis for further work in subsequent chapters. We then construct a small Reynolds number expansion of the flow function coming from the similarity solution.

We consider two parallel plates which has one porous wall (Fig. 2.2). The dimension of the channel is length L, width W, and height H. Fluid enters at x = 0 and either passes through the channel at x = L or the porous wall along the channel. The list of assumptions required to obtain an analytical solution is as follows:

- Physical properties of fluid are invariable: constant ρ (density), υ (viscosity)
- Newtonian, isotropic fluid: $\tau_{ij} = \mu(\frac{\partial v_i}{\partial x_j} + \frac{\partial v_j}{\partial x_i})$
- Incompressible fluid: $\frac{D\rho}{Dt} \rightarrow 0$
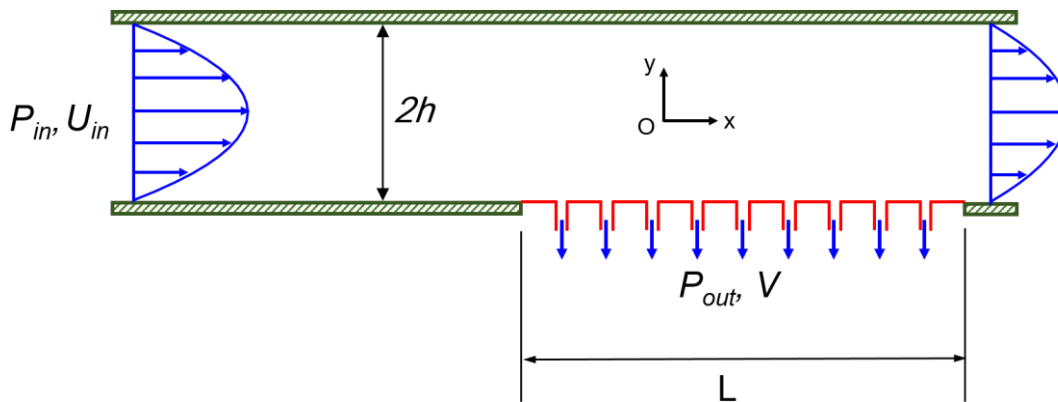- Fully developed flow at x = 0: u = u(x) only, parabolic velocity profile.
- Laminar flow

Figure 2.2 Schematic of flow with a porous wall in microchannel. P_{in} and U_{in} are the pressure and the velocity at the inlet of the channel. P_{out} and V are the pressure and the velocity at the outlet of the porous wall, respectively.

- Uniform porosity
- Constant suction

General governing equations are set as the following:

1. Continuity equation: $\frac{D\rho}{Dt} = 0$
2. Momentum equation: $\frac{D(\rho U)}{Dt} = \nabla P + \mu \nabla^2 U$

Applying assumptions above, the equations are simplified:

$$\frac{\partial u}{\partial x} + \frac{\partial v}{\partial y} = 0, \tag{2.1}$$

$$\rho \left(u \frac{\partial u}{\partial x} + v \frac{\partial u}{\partial y} \right) = -\frac{\partial P}{\partial x} + \mu \left(\frac{\partial^2 u}{\partial x^2} + \frac{\partial^2 u}{\partial y^2} \right), \tag{2.2}$$

$$\rho \left(u \frac{\partial v}{\partial x} + v \frac{\partial u}{\partial y} \right) = -\frac{\partial P}{\partial y} + \mu \left(\frac{\partial^2 v}{\partial x^2} + \frac{\partial^2 v}{\partial y^2} \right). \tag{2.3}$$

We introduce a stream function (ψ) that is defined as follows:

$$u = \frac{\partial \psi}{\partial y} \,, v = -\frac{\partial \psi}{\partial x} \tag{2.4}$$

The continuity equation (2.1) is automatically satisfied with this stream function. Also, we introduce non-dimensional variables and number,

$$x^* = \frac{x}{h}, \quad y^* = \frac{y}{h}, \quad u^* = \frac{u}{V}, \quad v^* = \frac{v}{V}, \quad \mathrm{Re}_v = \frac{\rho V h}{\mu} \tag{2.5}$$

, where Re_v is the Reynolds number. Using dimensionless variables and the Reynolds number, we can rewrite (2.2) and (2.3) as

$$u^* \frac{\partial u^*}{\partial x^*} + v^* \frac{\partial u^*}{\partial y^*} = -\frac{h}{\rho V^2} \frac{\partial P}{\partial x} + \frac{1}{Re_v} \left(\frac{\partial^2 u^*}{\partial x^{*2}} + \frac{\partial^2 u^*}{\partial y^{*2}} \right), \tag{2.6}$$

$$u^* \frac{\partial v^*}{\partial x^*} + v^* \frac{\partial v^*}{\partial y^*} = -\frac{h}{\rho V^2} \frac{\partial P}{\partial y} + \frac{1}{Re_v} \left(\frac{\partial^2 v^*}{\partial x^{*2}} + \frac{\partial^2 v^*}{\partial y^{*2}} \right), \tag{2.7}$$

19

To obtain analytical solution, we will use the similarity solution suggested by Berman[1].

$$\psi\,(x^*, y^*) = x^* G(y^*) \tag{2.8}$$

The velocity components (2.4) in terms of the similarity solution (2.5) are

$$u^* = \frac{\partial\psi}{\partial y^*} = x^* G'(y^*), \quad v^* = -\frac{\partial\psi}{\partial x^*} = -G(y^*) \tag{2.9}$$

Using (2.9), the momentum equations (2.6), (2.7) are reduced after the following manipulation,

$$x^* G'(y^*)\frac{\partial(x^* G'(y^*))}{\partial x^*} + \left(-G(y^*)\frac{\partial(x^* G'(y^*))}{\partial y^*}\right) = -\frac{h}{\rho V^2}\frac{\partial P}{\partial x^*} + \frac{1}{Re_v}\left(\frac{\partial^2(x^* G'(y^*))}{\partial x^{*2}} + \frac{\partial^2(x^* G'(y^*))}{\partial y^{*2}}\right),$$

$$\tag{2.10a}$$

$$x^*(G'(y^*))^2 - x^* G(y^*)G''(y^*) = -\frac{h}{\rho V^2}\frac{\partial P}{\partial x^*} + \frac{1}{Re_v}(x^* G'''(y^*)), \tag{2.10b}$$

$$\frac{h}{\rho V^2}\frac{\partial P}{\partial x^*} = -(G'(y^*))^2 + G(y^*)G''(y^*) + \frac{1}{Re_v}G'''(y^*), \tag{2.10c}$$

$$x^* G'(y^*)\frac{\partial(-G(y^*))}{\partial x^*} + \left(-G(y^*)\frac{\partial(-G(y^*))}{\partial y^*}\right) = -\frac{h}{\rho V^2}\frac{\partial P}{\partial y^*} + \frac{1}{Re_v}\left(\frac{\partial^2(-G(y^*))}{\partial x^{*2}} + \frac{\partial^2(-G(y^*))}{\partial y^{*2}}\right),$$

$$\tag{2.11a}$$

$$G(y^*)G'(y^*) = -\frac{h}{\rho V^2}\frac{\partial P}{\partial y^*} - \frac{1}{Re_v}G''(y^*), \tag{2.11b}$$

$$-\frac{h}{\rho V^2}\frac{\partial P}{\partial y^*} = G(y^*)G'(y^*) + \frac{1}{Re_v}G''(y^*), \tag{2.11c}$$

The right side of (2.10c) is a function of x only. Therefore, by Differentiation of (2.10c) with respect to y^*, we obtain

$$\frac{\partial}{\partial y^*}\left(\frac{h}{\rho V^2 x^*}\frac{\partial P}{\partial x}\right) = 0 = \frac{\partial}{\partial y^*}\left(-(G'(y^*))^2 + G(y^*)G''(y^*) + \frac{1}{Re_v}G'''(y^*)\right),$$

(2.12a)

$$-2G'(y^*)G''(y^*) + G'(y^*)G''(y^*) + G(y^*)G'''(y^*) + \frac{1}{Re_v}G''''(y^*) = 0,$$

(2.12b)

$$\therefore \ Re_v(G(y^*)G'''(y^*) - G'(y^*)G''(y^*)) + G''''(y^*) = 0, \text{ or} \qquad (2.12c)$$

$$Re_v(G(y^*)G''(y^*) - (G'(y^*))^2) + G'''(y^*) = k. \qquad (2.12d)$$

The boundary conditions are

$$v^* = -G(y^* = -1) = -1, \qquad (2.13a)$$

$$u^* = x^*G'(y^* = +1) = 0, \quad v^* = -G(y^* = +1) = 0, \qquad (2.13b)$$

$$\frac{\partial u^*}{\partial y^*} = -G''(y^* = 0) = 0 \qquad (2.13c)$$

Now, for very small Re, we try to obtain a steady solution using perturbation expansion[2].

$$G(y^*) = \sum_{n=0}^{\infty}\frac{1}{n!}Re_v^{\ n}g_n(y^*), \ \ k = \sum_{n=0}^{\infty}\frac{1}{n!}Re_v^{\ n}k_n, \qquad (2.14)$$

We substitute (2.14) into (2.12d) and compare the coefficients of the power series. Because of low Re, we utilize the perturbation expansion up to the second order:

$$Re_v\left(\left(g_0(y^*) + Re_vg_1(y^*) + \frac{1}{2}Re_v^{\ 2}g_2(y^*) + \cdots\right)\left(g_0''(y^*) + Re_vg_1''(y^*) + \right.\right.$$

$$\left.Re_v^{\ 2}g_2''(y^*) + +\cdots\right) - \left(g_0'(y^*) + Re_vg_1'(y^*) + \frac{1}{2}Re_v^{\ 2}g_2'(y^*) + \cdots\right)^2\right) +$$

$$g_0'''(y^*) + Re_vg_1'''(y^*) + Re_v^{\ 2}g_2'''(y^*) + \ldots = k_0 + Re_vk_1 + \frac{1}{2}Re_v^{\ 2}k_2 + \cdots,$$

(2.15a)

$$g_0'''(y^*) = k_0, \tag{2.15b}$$

$$Re_v(g_o(y^*)g_o''(y^*) - g_o'^2(y^*) + g_1'''(y^*)) = Re_v k_1, \tag{2.15c}$$

$$Re_v^2(g_o(y^*)g_1''(y^*) + g_o''(y^*)g_1(y^*) - 2g_0'g_1' + \tfrac{1}{2}g_2'''(y^*)) = \tfrac{1}{2}Re_v^2 k_2, \tag{2.15d}$$

Boundary conditions can be rewritten from (2.13):

$$g_0(y^* = -1) = -1, \tag{2.16a}$$

$$g_n'(y^* = +1) = 0 \ , g_0(y^* = +1) = 0, \tag{2.16b}$$

$$g_n''(y^* = 0) = 0. \tag{2.16c}$$

From (2.15b), we can obtain solutions up to second order with boundary conditions (2.16):

$$g_0(y^*) = -\tfrac{1}{4}y^{*3} + \tfrac{3}{4}y^* - \tfrac{1}{2}, \tag{2.17a}$$

$$g_1(y^*) = \tfrac{1}{1120}y^{*7} - \tfrac{1}{32}y^{*4} + \tfrac{1}{32}y^{*4} + \tfrac{67}{1120}y^{*3} - \tfrac{17}{280}y^* + \tfrac{1}{32}, \tag{2.17b}$$

$$k = -\tfrac{3}{2} - \tfrac{57}{280}Re_v + \cdots, \tag{2.18d}$$

Now, based on flow velocity profile, we consider mass concentration polarization during crossflow as shown in Fig. 2.3. The higher polarized concentration means that most of bacteria moves toward the surface of the porous membrane. First, the governing equation of diffusion is following:

$$u\frac{\partial c}{\partial x} + v\frac{\partial c}{\partial y} = D_0\left(\frac{\partial^2 c}{\partial x^2} + \frac{\partial^2 c}{\partial y^2}\right). \tag{2.19}$$

When the Re_v is small, diffusion along with x is negligible compared with transverse diffusion:

$$\frac{\partial^2 c}{\partial x^2} = 0. \tag{2.20}$$

We introduce non-dimensional variables and number:

$$x^* = \frac{x}{h}, \quad y^* = \frac{y}{h}, \quad u^* = \frac{u}{U}, \quad v^* = \frac{v}{U}, \quad \text{Pe}_t = \frac{Uh}{D_0} \qquad (2.21)$$

, where Pe_t is the transverse Peclet number and D_0 is diffusivity. Using (2.21), we simplify (2.19) into

$$Pe_t(u^* \frac{\partial C}{\partial x^*} + v^* \frac{\partial C}{\partial y^*}) = \frac{\partial^2 C}{\partial x^{*2}} + \frac{\partial^2 C}{\partial y^{*2}} . \qquad (2.22)$$

The boundary conditions are

$$Pe_t C = \frac{\partial C}{\partial y^*} \ (@y^* = -1), \qquad (2.23a)$$

$$\frac{\partial C}{\partial y^*} = 0 \ (@y^* = 1), \qquad (2.23b)$$
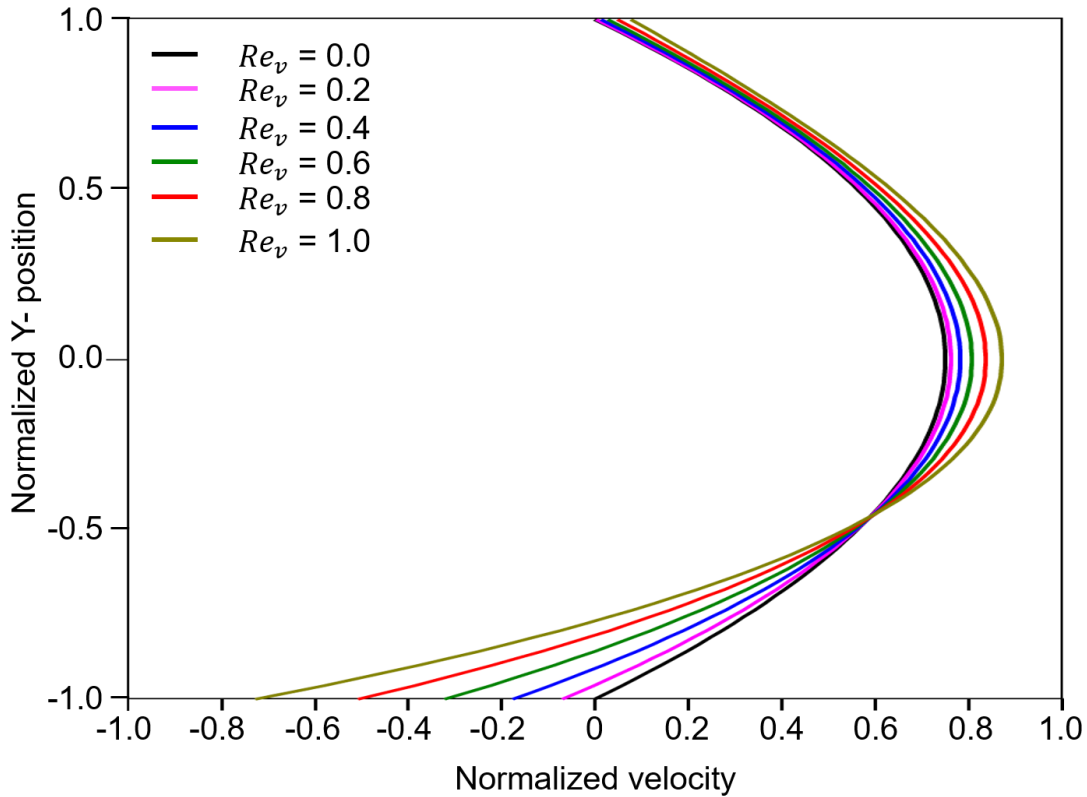
Figure 2.3 The velocity profiles with different Re_v.

We assume

$$C(x^*, y^*) = A(x^*)B(y^*). \tag{2.24}$$

Substituting (2.9) and (2.24) into (2.22), we obtain:

$$Pe_t\big(x^*G'(y^*)B(y^*)A'(x^*) - G(y^*)A(x^*)B'(y^*)\big) = A(x^*)B''(y^*),$$

$$x^* \frac{A'(x^*)}{A(x^*)} = \frac{1}{G'(y^*)B(y^*)}\left(G(y^*)B'(y^*) + \frac{1}{Pe_t}B''(y^*)\right). \tag{2.25}$$

The left side of (2.25) is a function of x only and the right side of (2.25) is a function of y only. Therefore, (2.25) should be equal to constant (a). We can rewrite (2.25) as:

$$aG'(y^*)B(y^*) = G(y^*)B'(y^*) + \frac{1}{Pe_t}B''(y^*),$$

$$Pe_t(a+1)G'(y^*)B(y^*) = \frac{d}{dy^*}\Big(B'(y^*) + Pe_t G(y^*)B(y^*)\Big). \tag{2.26}$$

Integrating (2.26) on interval [-1,1] yields:

$$Pe_t(a+1)\int_{-1}^{1} G'(y^*)B(y^*)dy^* = \Big[B'(y^*) + Pe_t G(y^*)B(y^*)\Big]_{-1}^{1}. \tag{2.27}$$

Using boundary conditions of $B'(y^*)$, $G(y^*)$, and $B(y^*)$, the right side of (2.27) is zero. Therefore, the left side of (2.26) is zero:

$$(a+1)\int_{-1}^{1} G'(y^*)B(y^*)dy^* = 0. \tag{2.28}$$

In (2.27), a must be -1 because $G'(y^*)$ and $B(y^*)$ are non-zero terms. Thus, in (2.26),

$$B'(y^*) + Pe_t G(y^*)B(y^*) = 0,$$

$$\frac{B'(y^*)}{B(y^*)} + Pe_t G(y^*) = 0. \tag{2.29}$$

Integrating (2.29) yields:

$$\ln B(y^*) - \ln B(-1) = -Pe_t \int_{-1}^{y^*} G(y^*)dy^*,$$

$$B(y^*) = B(-1)\exp(Pe_t \int_{-1}^{y^*} G(y^*)dy^*). \tag{2.30}$$

Using (2.14) and (2.17), we obtain

$$\int_{-1}^{y^*} G(y^*)dy^* = \sum_{n=0}^{\infty} \frac{1}{n!} Re_v^{\ n} \int_{-1}^{y^*} g_n(y^*)dy^* = -\frac{1}{16}y^{*4} + \frac{3}{8}y^{*2} - \frac{1}{2}y^* + \frac{13}{16} + Re_v(\cdots).$$

$$\tag{2.31}$$

By the way, we obtain $A(x^*)$ from (2.25) and $a = -1$:

$$A(x^*) = -\frac{A(0)}{x^*}. \tag{2.32}$$

Therefore, we obtain

$$C(x^*, y^*) = A(0)B(0) = -\frac{A(0)}{x^*} \exp(Pe_t(\frac{1}{16}y^{*4} - \frac{3}{8}y^{*2} + \frac{1}{2}y^* + \frac{13}{16} + Re_v(\cdots))). \tag{2.33}$$

We assess the concentration at the wall ($y^* = -1$) as follows:

$$C_w(x^*, -1) \approx -\frac{A(0)}{x^*} \exp(\frac{13}{8} Pe_t). \tag{2.34}$$

Therefore, we normalize concentration profile using (2.33) and (2.34):

$$\frac{C(x^*, y^*)}{C_w(x^*, -1)} \approx \exp(Pe_t \left(-\frac{1}{16}y^{*4} + \frac{3}{8}y^{*2} - \frac{1}{2}y^* - \frac{13}{16} \right)). \tag{2.35}$$

25

As shown in Fig. 2.4, we found that concentration near the wall is higher as Pe_t is bigger.

In this chapter we have found a similarity solution for the flow of a power-law fluid in a channel driven by fluid injection or suction through the porous channel walls. We have then used this solution as a basis for a small Re expansion of the solution, for linear spatial and temporal stability problems and then presented the equivalent regularized problems for flow and stability calculations. In subsequent chapters we restrict attention to the power-law fluid with exponent $n \in (0, 2)$. Flowing materials modelled by power-law fluid viscosity models are more commonly found with their power-law exponents in this range than for $n > 2$. We shall further restrict attention of the fluid flow to that within a one porous walled channel, corresponding to the problem selection parameter $E = 1$.
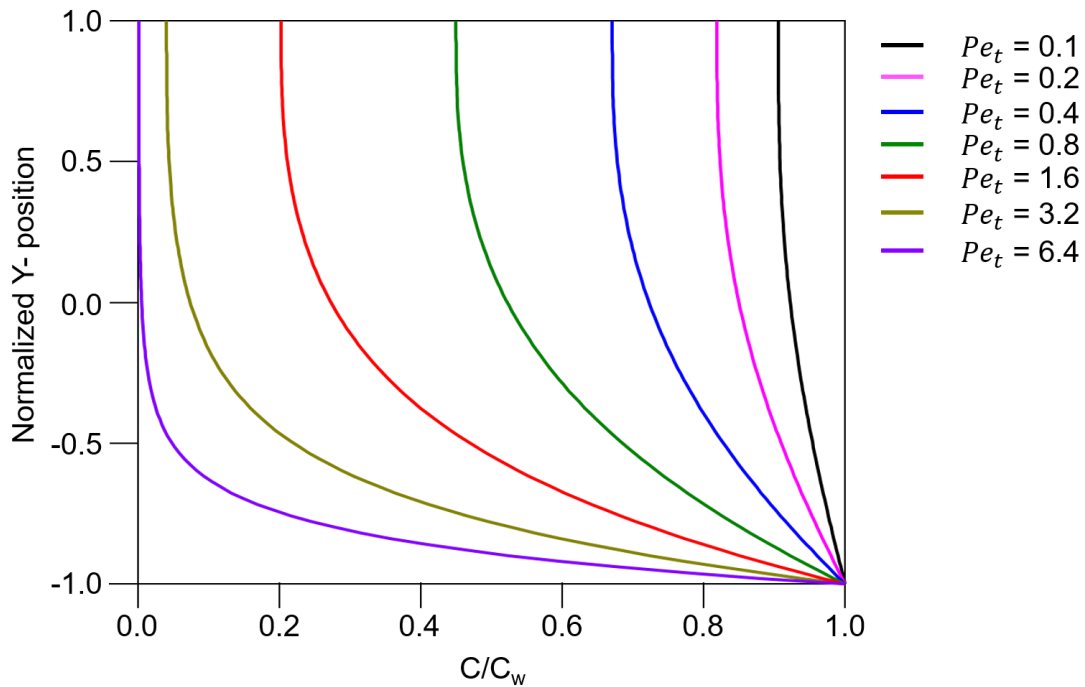
Figure 2.4 Normalized mass concentration profile.

2.2   FABRICATION OF MICROFLUIDIC DEVICES FOR SAMPLE PREPARATION AND SELECTIVE BACTERIA CAPTURE

The microfluidic device for sample preparation and selective bacteria capture consists of a top layer made by poly (dimethylsiloxane) (PDMS) bonded to a glass substrate. The PDMS layer is fabricated using soft lithography techniques in Fig 2.5. The fabrication process began with wafer cleaning. A wafer was ultrasonicated with acetone for 5 minutes due to removing organic contamination. Then, a wafer was ultrasonicated with isopropyl alcohol (IPA) for 5 minutes followed by DI water rinsing and blowing with nitrogen gas. Rinsed wafer was placed on a hot plate at
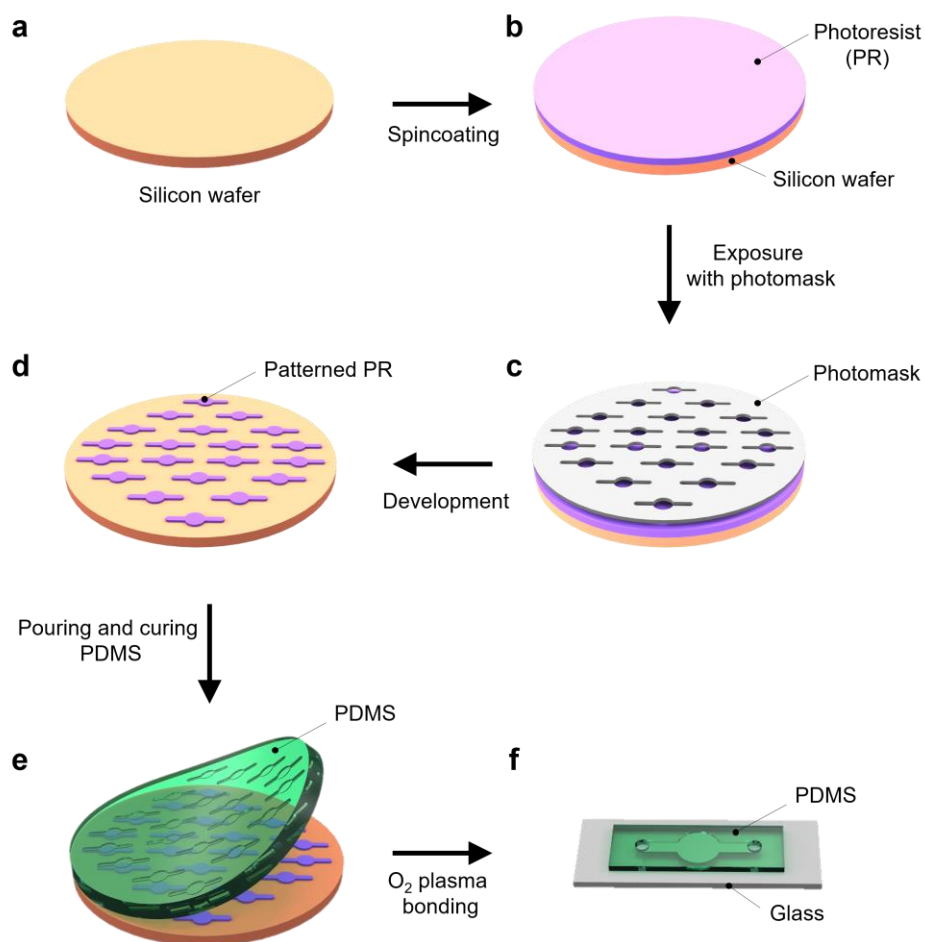
Figure 2.5 Fabrication of a PDMS device using photolithography. (a) Cleaning of silicon wafer. (b) Spincoating of photoresist on a silicon wafer. (c) UV exposure on a silicon wafer and a photomask. (d) Master mold of a PDMS layer. (e) Pouring, curing, and peeling off a PDMS layer. (f) Bonding of the PDMS layer on a glass substrate using oxygen plasma treatment.

200 °C for 15 minutes for dehydration. After dehydration, the wafer was treated with oxygen plasma for 1 minute as an extra cleaning. Then, SU-8 3035 photoresist (MicroChem, MA) was spread on the wafer at 500 rpm for 15 seconds and then, spin-coated at 2000 rpm for 30 seconds to produce a 50-µm layer. The wafer was transferred to a hot plate with 95 °C for 30 minutes as a soft bake step. Soft bake reduces the remaining solvent of photoresist, which allows to avoid mask contamination, improve resist adhesion, prevent bubbling, and make photoresist uniform[3]. Next, the soft-baked wafer was placed below the mask and exposed to the ultraviolet light for 15 seconds. Then, the exposed wafer transferred to a hot plate with 95 °C for 10 minutes as a post exposure bake step in order to reduce mechanical stress generated during soft bake and exposure steps and improve resist adhesion[4]. The wafer cooled down to room temperature and was immersed in SU-8 developer (MicroChem, MA) and gently shook for 15 minutes. After development, the wafer was rinsed with IPA and DI water followed by drying with nitrogen gas. The photoresist-patterned wafer was coated with (3-Mercaptopropyl) trimethoxysilane for 3 hours in a vacuum chamber in order to prevent PDMS from adhering to the wafer. PDMS polymer and curing agent (Sylgard 184, Dow Corning) were prepared at 10:1 (w/w) ratio, poured on the wafer, degassed in a vacuum chamber for 2 hours, and cured in a 65 °C oven overnight to make a PDMS fluidic layer. The PDMS layer was carefully peeled off from the wafer and cut into each piece. Fluidic inlets and outlets were punched through with a 0.75 mm puncher. Then, the PDMS layer and a glass layer were treated with O_2 plasma for 40 seconds, bonded to each other and stored in a 65 °C oven for 1 hour. The microfluidic device was degassed overnight for removing unnecessary bubble in microfluidic channels.

2.3 ENRICHMENT AND EFFICIENT SELECTIVE BACTERIAL CAPTURE FROM WHOLE BLOOD IN A 3D MICROCHANNEL

Enrichment of green fluorescent protein (GFP)-expressing *E. coli*.

In order to perform bacterial enrichment in a microfluidic device without a centrifuge, we designed and used membrane-based preconcentration module in the microfluidic device. In this experiment, the microfluidic device was investigated under a fluorescent microscope to image the enrichment of GFP-expressing *E. coli*. When observing under a bright-field conventional microscope, it was difficult to distinguish between the pores of porous membranes and *E. coli*. The sizes of *E. coli* (1-2 µm in length) are larger than the pore size of porous membrane (less than 1 µm). Figure 2.6 shows that sequential fluorescent images of E. coli on the porous

membrane within 3 minutes from 1-ml of bacterial suspension in PBS. Bacterial concentration was 10^6 cells/ml. Due to the size difference between *E. coli* and pores, most of *E. coli* didn't go through pores of the membrane even if the flow rate was high enough. To estimate the enrichment factor, we assumed that all *E. coli* were covered on the porous membrane only. The volume which all *E. coli* occupy was 0.0565 µl ($V_{E.coli} = \frac{\pi}{4} D_{chamber}{}^2 h$, $D_{chamber}$ is the diameter of the chamber, h is the length of *E.coli*.) and the sample volume was 1 ml. Therefore, the enrichment was estimated as about 17,700.

Selective capture of Bacteria in 3D microchannel.

In the previous experiment, we were able to preconcentrate bacteria on the porous membrane in the 3D microfluidic device. To capture specific species of bacteria selectively, we used monoclonal antibodies (MAbs) on the surface of the chamber. Abs-based methods of capturing and separating bacteria have been well developed due to high specificity and sensitivity[5–8]. However, most 2D microfluidic device needed high bacterial concentrations because the chance for bacteria and antibody to bind was low, which was a major limitation of antibody-mediate methods (Fig. 2.7a). To overcome this limitation, we designed and tested a 3D microfluidic device including porous membrane (Fig. 2.7b). As shown in Fig. 2.7b, during incubation and preconcentration step, bacterial suspension entered in a top layer, flew through the porous membrane, and went out to the bottom layer only.
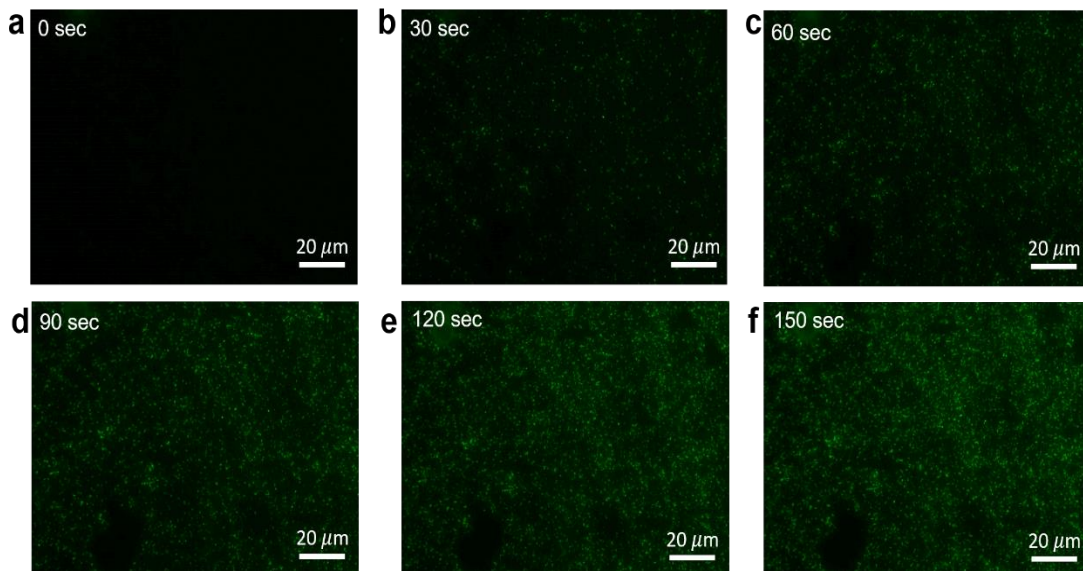

Figure 2.6 Enrichment of *E. coli* on the porous membrane in the microfluidic device. (a) – (f) Sequential fluorescent images of GFP-expressed *E. coli* every 30 seconds.

Then, unbound bacteria were washed out through the top layer. To verify this concept, we tested a 2D microfluidic device and a 3D microfluidic device with the same channel design. We used monoclonal anti-*E. Coli* antibody (CH1810, Silver lake research, CA). Figure 2.8 shows that the number of   bacteria measured on the surface of the porous membrane over the total injected cells in chip. Comparing 2D conventional microfluidic device, the 3D microfluidic device was able to detect the bacteria at two order lower bacterial concentration. Then, we applied the 3D microfluidic device for different Gram-negative bacteria, *Klebsiella pneumoniae* (*K. pneumoniae*). We incubated polyclonal anti-*K. Pneumoniae* antibody (PA1-7226,
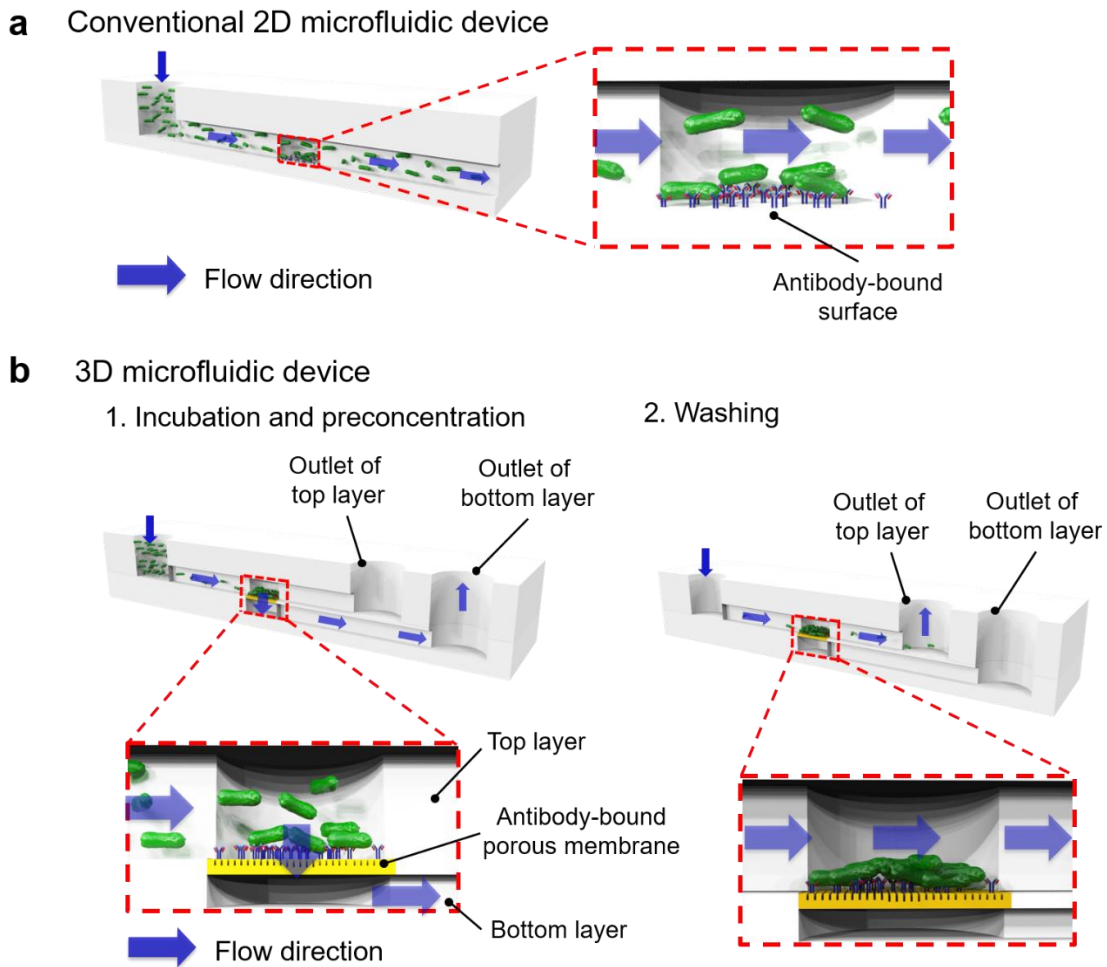
Figure 2.7 Schematic representation of on-chip immunoassay. (a) Conventional 2D microfluidic device for immunoassay. (b) 3D microfluidic device for this experiment. 1) Incubation and preconcentration of bacteria for binding bacteria to the surface of porous membrane. (Only outlet of bottom layer opens.) 2) Washing of unbound bacteria and other components. (Only outlet of top layer opens.)

Thermo fisher scientific) on the surface of the porous membrane. As shown in Figure 2.9, we also detected *K. pneumoniae* on the surface as low as 10^4 cells/ml. Capture efficiency was about 10 %.
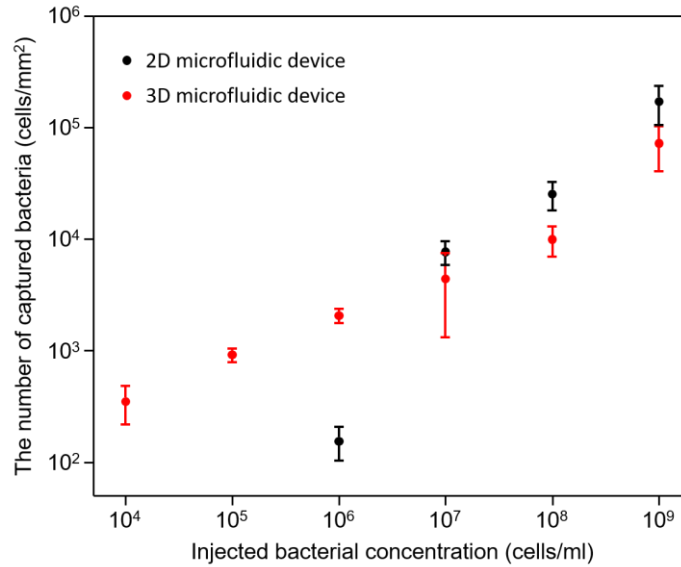

Figure 2. The number of captured *E. coli* on the porous membrane in the microfluidic device comparing between 2D and 3D microfluidic device.
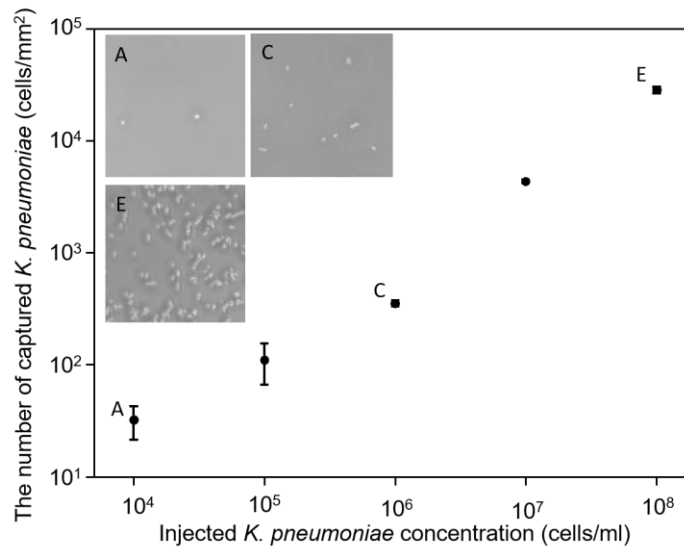

Figure 2.9 The number of captured *K. pneumoniae* on the porous membrane in the microfluidic device.

Preconcentration and selective capture of bacteria from whole blood in 3D microchannel.

In a blood sample, there are many components such as white blood cells, red blood cells, proteins, and platelet. Due to interfere of other components in blood, it is difficult to detect bacteria from a blood sample. Thus the bacteria should be selectively isolated and captured from blood[9,10]. In addition, in sepsis, because the number of bacteria in a blood sample is low, preconcentration of bacteria is also an
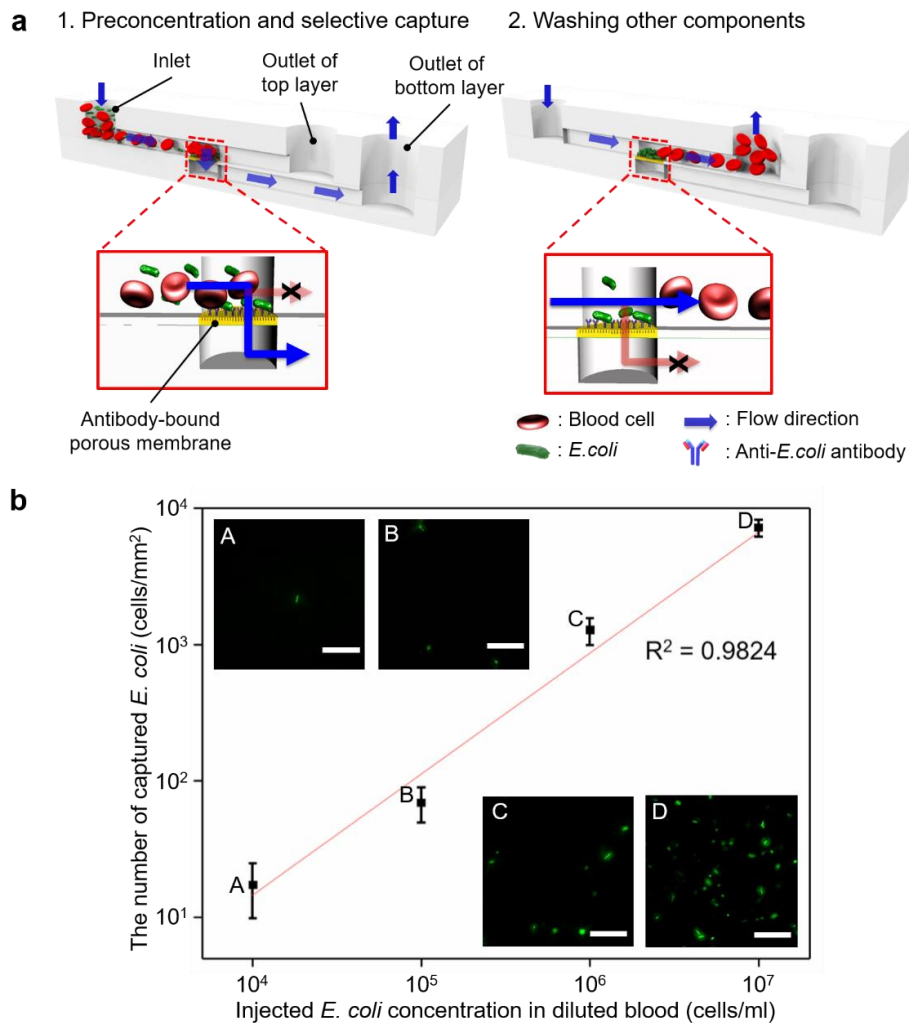
Figure 2.10 Isolation of bacteria from diluted whole blood (a) Procedure of sample preparation. 1) Preconcentration and selective capture of bacteria on the antibody-mediated porous membrane. 2) Washing of unbound bacteria and other blood components. (b) The number of captured *E.coli* on the porous membrane.

important step. Therefore, without a step of sample preparation, we demonstrated a simple 3D microfluidic device with porous membrane to preconcentrate, isolate, and capture bacteria from a blood sample. Figure 2.10 shows how the 3D microfluidic device works. A blood sample comes from the inlet and the outlet of the lower layer only closes. Thus, all of the blood sample pass though the porous membrane. While sample flows through the membrane, bacteria are captured by antibodies on the surface of the membrane. In this case, bacteria have more opportunities to meet antibody than sample flows parallel to the surface of the porous membrane. In addition, we can handle a large volume of sample and preconcentrate bacteria on the surface. After capturing bacteria, the outlet of the bottom layer closes and the outlet of the top layer opens. Flow direction changes parallel to the surface of the porous membrane. Thus, unbound bacteria and blood cells come out to the outlet of the top layer and only bacteria on the surface of the porous membrane are captured by antibody. A total of $10^4 - 10^7$ GFP-expressing E. coli cells per ml were spiked into 1:20 diluted blood and isolated at a flow rate of 10 μl/min. Bacteria were captured on the surface as low as 10^4 cells/ml.

2.4 CHEMICAL LYSIS OF BACTERIA ON A CHIP

After capturing bacteria in the chamber of the device, chemical lysis of bacteria was performed in Fig. 2.11a. Chemical lysis is one of the most popular methods using lysis buffer to solubilize lipids and proteins in the membrane, which forms pores on the membrane and eventually breaks the membrane[11–13]. Here, we tested and compared two popular lysis buffers, polymyxin B and lysozyme. To characterize chemical lysis of bacteria in the device, the porous membrane of the 3D devices was incubated with anti-*E. Coli* antibody for 2 hours at 37 ℃. After washing the device with PBS, GFP-expressed *E. coli* suspension flew into the device as shown in Fig. 2.11b. Then, the bacterial suspension was replaced with different concentration of polymyxin B and lysozyme[14–16] (Fig. 2.6a). Fluorescent images of the captured cells on the surface of the porous membrane were taken using a stereo zoom microscope (Axio Zoom.V16, Car Zeiss Microscopy, USA). In Figure 2.11b and c, we found that the fluorescent intensities of GFP-expressing *E. coli* were decreased over time due to breaking the membrane of *E. coli*. Then, we quantified the fluorescent intensities of GFP-expressing *E. coli* (Fig 2.11 d and e). In polymyxin B, fluorescent intensities of GFP-expressing *E. coli* were reduced to 20% of the original intensities after 5 minutes. By comparison, in lysozyme, it took
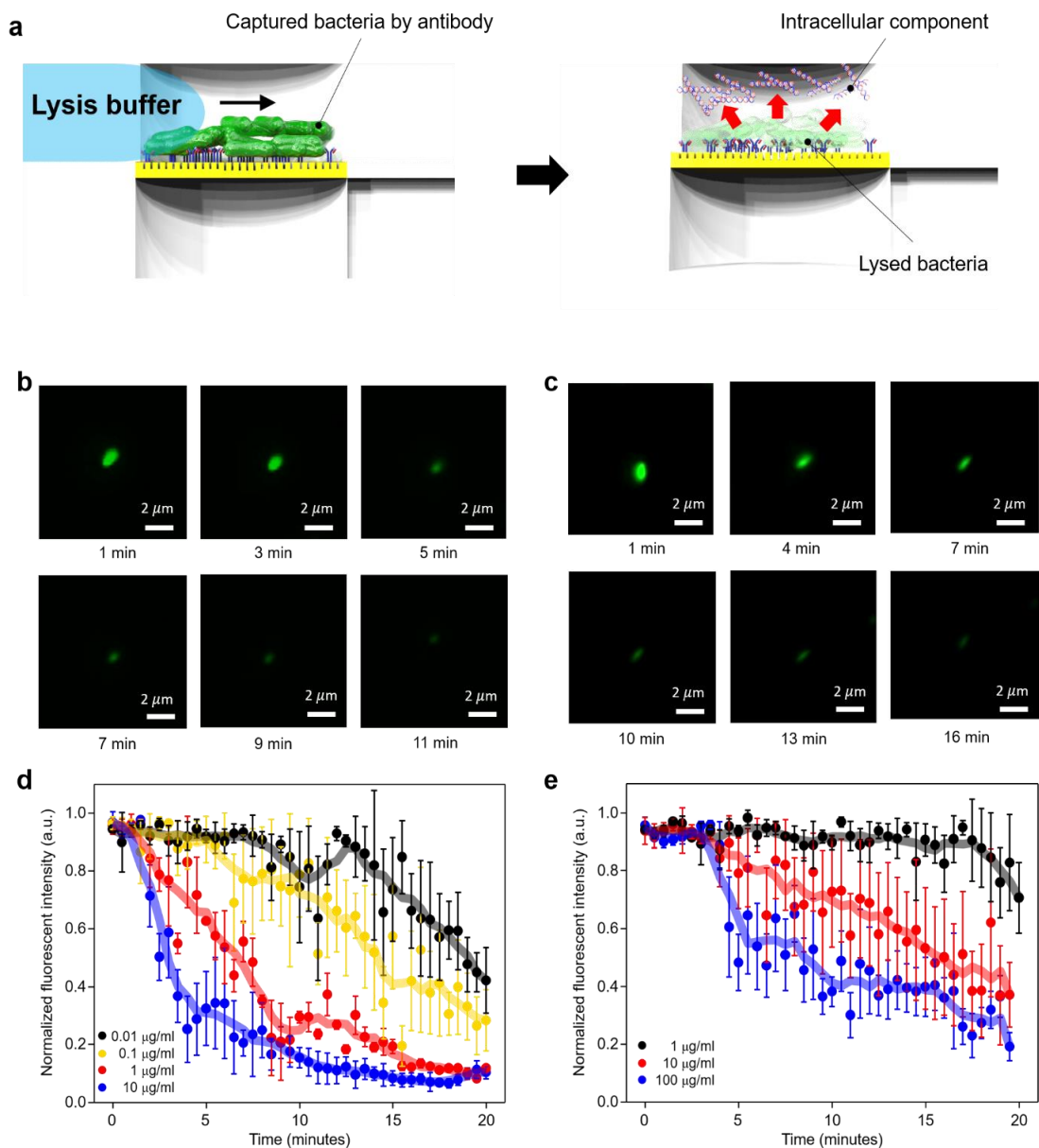
Figure 2.11 Chemical lysis of bacteria in the microfluidic device. (a) Schematic illustration of the chemical lysis of bacteria. (b), (d) Representative sequential fluorescent images of a single GEP-expressing *E. coli* (concentration of polymyxin B: 10 μg/ml) and the fluorescent intensity of a single *E. coli* over time after the introduction of polymyxin B (n = 3). (c), (e) Representative sequential fluorescent images of a single GEP-expressing *E. coli* (contentration of lysozyme: 100 μg/ml) and the fluorescent intensity of a single *E. coli* over time after the introduction of lysozyme (n = 3).

about 20 minutes for the fluorescent intensities to decrease to 20% of the original intensities. Thus, polymyxin B was more effective in lysing *E. coli* than lysozyme in the microfluidic device. The main target of polymyxin B is lipopolysaccharide of outer membrane of Gram-negative bacteria, whereas it may be little effective in lysing Gram-positive bacteria[16].

2.5 ULTRAFAST PHOTOTHERMAL LYSIS OF BACTERIA ON A CHIP

Figure 2.12a shows the schematic illustration of photothermal lysis on the device. After capturing bacteria in the chamber of the device, a blue light comes to the gold (Au)-deposited porous membrane. The Au-deposited porous membrane converts electromagnetic energy (light) to thermal energy (heat), which increases the temperature of the chamber and lyses bacteria. Under plasmonic resonance, this phenomenon is enhanced, which called a photothermal effect. Au-deposited porous membrane absorbs electromagnetic energy efficiently in the wavelength of 400 - 500 nm (Fig. 2.12b). To verify the photothermal lysis of bacteria, we deposited 80-nm of Au on the polycarbonate porous membrane (GE Healthcare Bio-Sciences, USA) using an e-beam evaporator (Rocky Mountain Vacuum Tech,
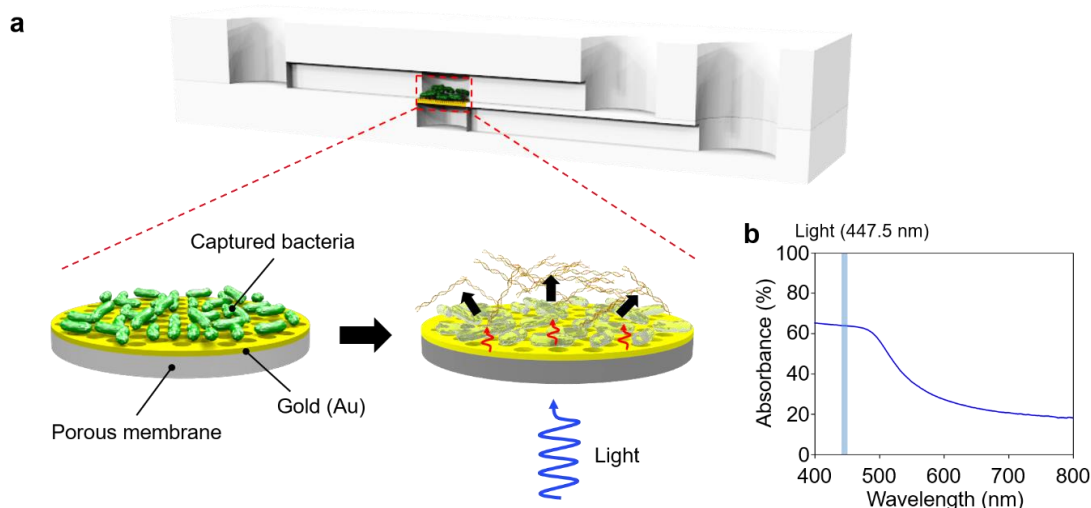

Figure 2.12 Schematic illustration of photothermal lysis of bacteria in the microfluidic device. (a) Procedure of photothermal lysis of bacteria with a blue light ($\lambda = 447.5$ nm). Au-deposited porous membrane absorbs the light and generates heat from the absorbed light. (b) UV-vis spectrum of an Au-deposited polycarbonate porous membrane. The peak wavelength of the light was 447.5 nm.

USA). After bonding the porous membrane to the device using O_2 plasma, *E. coli* were captured on the membrane. Then, we irradiated the Au-deposited porous membrane using a 447.5 nm LED (Luxeon star LEDs, Canada). Then, viability tests were performed on bacteria using a LIVE/DEAD bacterial viability kit (Thermo fisher scientific, USA) to quantify live and dead bacteria on fluorescence stereo zoom microscopy (Axio Zoom.V16, Car Zeiss Microscopy, USA). Firstly, we investigated the temperature profile of the chamber with the Au-deposited porous membrane at different input powers (Fig. 2.13b). With 0.5 W of input
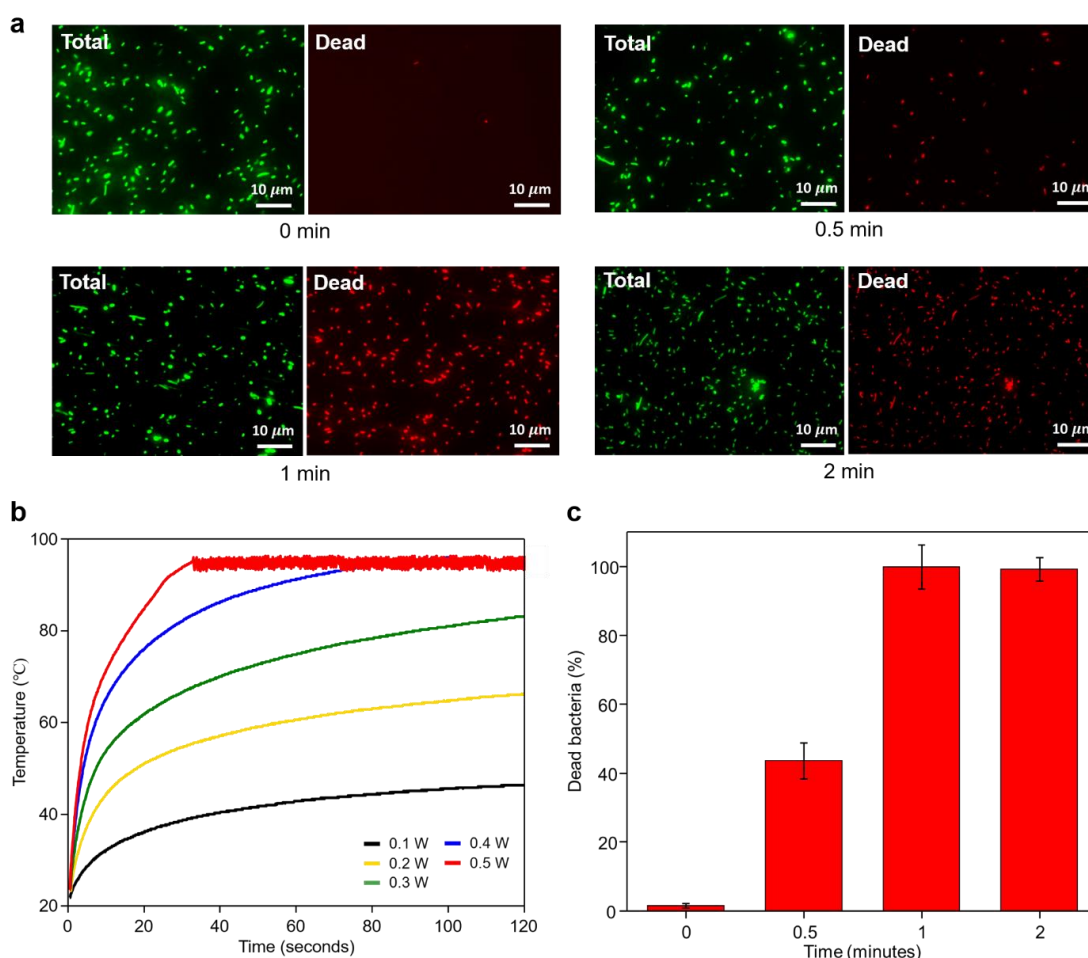
Figure 2.13 Photothermal lysis of bacteria in the microfluidic device. (a) Fluorescent images of *E. coli* after the introduction of a blue light ($\lambda = 447.5$ nm) for the time below images. Green dye: all bacteria (SYTO 9 stain), Red dye: dead bacteria (propidium iodide stain). (b)Temperature profile of photothermal lysis at different input powers of a LED. (c) Viability of *E. coli* after photothermal lysis after the introduction of a light for the time. The power of light was 0.5 W.

power, the temperature of the chamber reached 95 ℃ for 35 seconds, which is high enough to lyse intact bacteria using light and Au-deposited porous membrane. Figure 2.13a shows the fluorescent images of bacteria stained by SYTO9 and propidium iodide for 20 minutes after the irradiation of the LED for the time below. SYTO 9 is a dye small enough to penetrate the cell membrane and stain the nucleic acids of both dead and live bacteria in green, while propidium iodide is too large to penetrate live cells. Thus, propidium iodide stains only dead bacteria in red. Thus, all live and dead bacteria look green while photothermally lysed one look red. Fig. 13c shows the number of dead cell following irradiation for various lengths of time.

2.6   BACTERIAL LYSIS WITH PULSED LIGHT

Photothermal lysis is a good candidate for lysing bacteria. However, due to high temperature, it is not good for detecting proteins or enzymes inside cells. Therefore, we demonstrated the bacterial lysis not increasing the entire temperature much. Figure 2.14a and b show the time schedule to turn on and off the light and their temperature profiles, respectively. In case of 0.6s/15s, the maximum temperature of the chamber was below 35 ℃. Also, comparing to Fig. 2.13a, the temperature of the chamber with pulsed light was at least more than 30 ℃ than the case of continuous light. Figure 2.15a shows the fluorescent images of bacteria stained by SYTO9 and propidium iodide for 20 minutes after the irradiation of the LED for the time schedules shown in Figure 2.14b. Even if the short time of turning
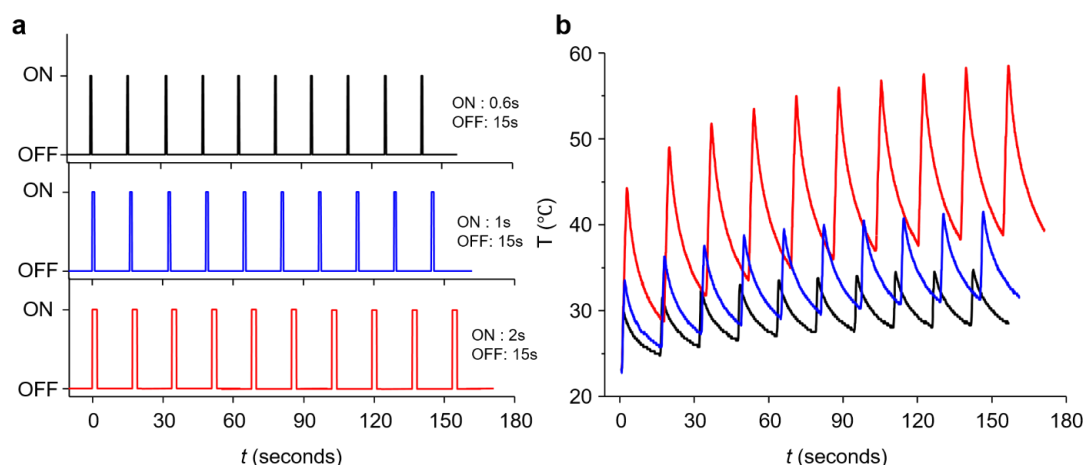

Figure 2.14 Photothermal lysis of bacteria with pulsed light. (a) The time schedule of turning on and off light. (b) The temperature profiles of (a).

on, some bacteria began to be dead. In addition, in the case of 2s/15s (on/off), more than 80 % of bacteria were dead in 3 minutes (Fig. 2.15b).
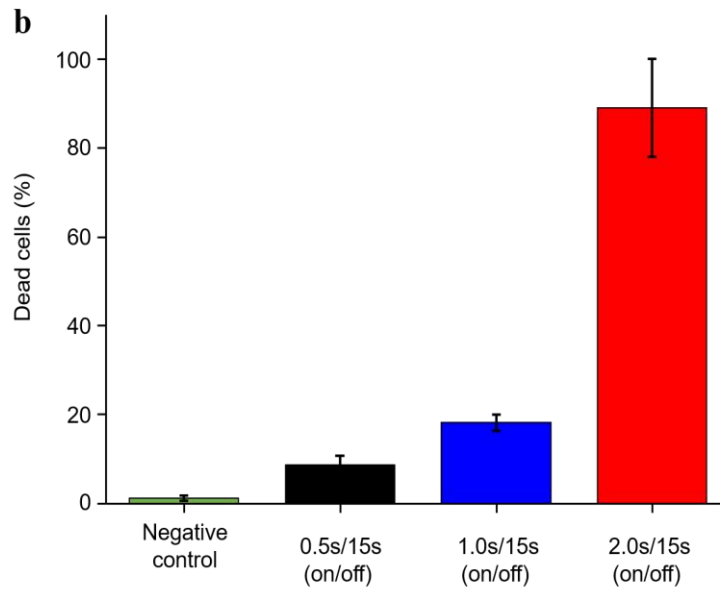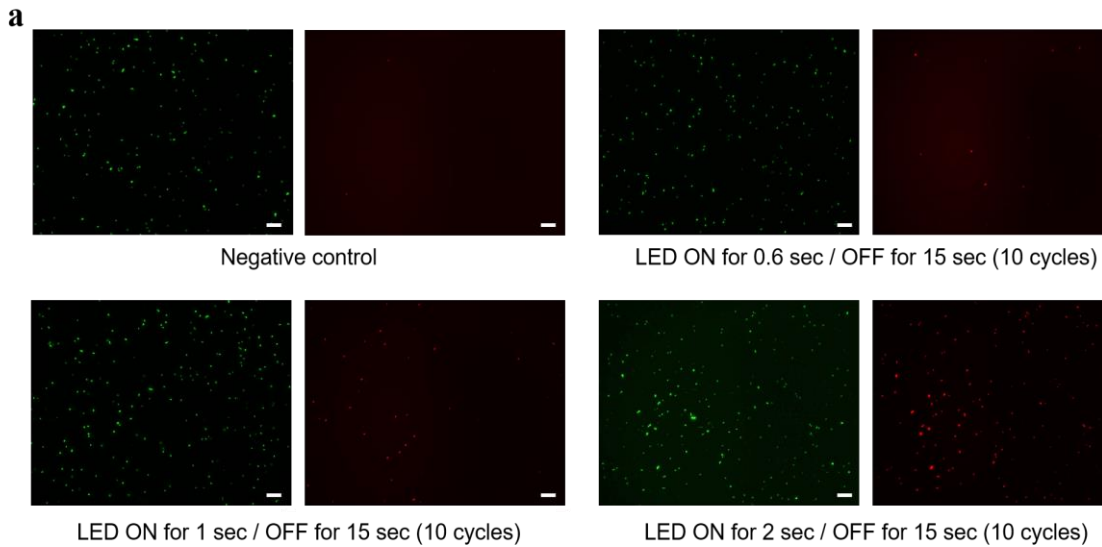

Figure 2.12 Viability test of bacteria after photothermal lysis with pulsed light. Fluorescent images of *E. coli* after the introduction of pulsed light ($\lambda = 447.5$ nm). Green dye: all bacteria (SYTO 9 stain), Red dye: dead bacteria (propidium iodide stain). (b) Viability of *E. coli* after photothermal lysis after the introduction of a light for the time. The power of light was 0.5 W.

2.7 CONCLUSION

In this chapter, we demonstrated a microfluidic device for sample preparation. Firstly, we analytically calculated the flow in microchannel with a porous wall. The lateral velocity profile is a function of Reynolds number of the escaping flow though the porous wall, which affects the distribution of bacteria on the porous wall. Then we demonstrated 3D microfluidic device with porous surfaces. By controlling the flow direction, we could preconcentrate and selectively capture bacteria on the surface of the porous membrane. Furthermore, unbound bacteria and blood cells were washed out as shown in Fig. 2.10. We decreased limit of detection by two orders comparing to a 2D microfluidic device. Then, we integrated chemical lysis and photothermal lysis with the microfluidic device. Especially, photothermal lysis enabled us to lyse bacteria in 1 minute.

2.8 REFERENCES

1.   Berman, A. S. Laminar flow in channels with porous walls. J. Appl. Phys. 24, 1232–1235 (1953).
2.   Haldenwang, P. Laminar flow in a two-dimensional plane channel with local pressure-dependent crossflow. J. Fluid Mech. 593, 463–473 (2007).
3.   Liu, J. et al. Process research of high aspect ratio microstructure using SU-8 resist. Microsyst. Technol. 10, 265–268 (2004).
4.   Mata, A., Fleischman, A. J. & Roy, S. Fabrication of multi-layer SU-8 microstructures. J. Micromechanics Microengineering 16, 276–284 (2006).
5.   Qiu, J., Zhou, Y., Chen, H. & Lin, J. M. Immunomagnetic separation and rapid detection of bacteria using bioluminescence and microfluidics. Talanta 79, 787–795 (2009).
6.   Laczka, O. et al. Improved bacteria detection by coupling magneto-immunocapture and amperometry at flow-channel microband electrodes. Biosens. Bioelectron. 26, 3633–3640 (2011).
7.   Sung, Y. J. et al. Novel antibody/gold nanoparticle/magnetic nanoparticle nanocomposites for immunomagnetic separation and rapid colorimetric detection of Staphylococcus aureus in milk. Biosens. Bioelectron. 43, 432–439 (2013).
8.   Li, Y. et al. Agarose-based microfluidic device for point-of-care concentration and detection of pathogen. Anal. Chem. 86, 10653–10659 (2014).

9.   Wellinghausen, N. et al. Diagnosis of bacteremia in whole-blood samples by use of a commercial universal 16S rRNA gene-based PCR and sequence analysis. J. Clin. Microbiol. 47, 2759–2765 (2009).

10.   I-Fang Cheng, Chang, H.-C., Chen, T.-Y., Hu, C. & Yang, F.-L. Rapid identification of pathogen in human blood by electrokinetic concentration and surface-enhanced Raman spectroscopy. Sci. Rep. 3, 2365 (2013).

11.   Mahalanabis, M., Al-Muayad, H., Kulinski, M. D., Altman, D. & Klapperich, C. M. Cell lysis and DNA extraction of gram-positive and gram-negative bacteria from whole blood in a disposable microfluidic chip. Lab Chip 9, 2811 (2009).

12.   Jen, C. P., Hsiao, J. H. & Maslov, N. A. Single-cell chemical lysis on microfluidic chips with arrays of microwells. Sensors 12, 347–358 (2012).

13.   Cichova, M., Proksova, M., Tothova, L., Santha, H. & Mayer, V. On-line cell lysis of bacteria and its spores using a microfluidic biochip. Cent. Eur. J. Biol. 7, 230–240 (2012).

14.   Prinz, C., Tegenfeldt, J. O., Austin, R. H., Cox, E. C. & Sturm, J. C. Bacterial chromosome extraction and isolation. Lab Chip 2, 207 (2002).

15.   Hall, J. A. et al. Evaluation of cell lysis procedures and use of a micro fluidic system for an automated DNA-based cell identification in interplanetary missions. Planet. Space Sci. 54, 1600–1611 (2006).

16.   Yu, Z., Qin, W., Lin, J., Fang, S. & Qiu, J. Antibacterial mechanisms of polymyxin and bacterial resistance. BioMed Research International 2015, (2015).

CHAPTER 3

ULTRAFAST PHOTONIC PCR AT POC SETTINGS

3.1 ABSTRACT

Polymerase chain reaction (PCR) is one of the most sensitive and powerful tools for clinical laboratories, precision medicine, personalized medicine, agricultural science, forensic science, and environmental science. Rapid and portable PCR, characterized by low power consumption, compact size and simple operation, is ideal for timely diagnosis at the point-of-care (POC). Although several fast/ultrafast PCR methods have been proposed, the use of a simple and robust PCR thermal cycler remains challenging for POC testing. Here we present an ultrafast photonic PCR method using plasmonic photothermal light-to-heat conversion via photon-electron-phonon coupling. We demonstrate an efficient photonic heat converter using a thin gold (Au) film due to its plasmon-assisted high optical absorption (~65 % at 450 nm, peak wavelength of heat source LEDs). The plasmon-excited Au film is capable of rapidly heating the surrounding solution to over 150 °C within 3 min. Using this method, ultrafast thermal cycling (30 cycles; heating and cooling rate of 12.79 ± 0.93 °C/sec and 6.6 ± 0.29 °C/sec, respectively) from 55 °C (temperature of annealing) to 95 °C/sec (temperature of denaturation) is accomplished within 5 minutes. Using photonic PCR thermal cycles, we demonstrate successful nucleic acid amplification. Our simple, robust and low cost-approach to ultrafast PCR using an efficient photonic-based heating procedure could be generally integrated into a variety of devices or procedures, including on-chip thermal lysis and heating for isothermal amplifications.

3.2 INTRODUCTION

After its initial invention in 1983 by Kary Mullis, polymerase chain reaction (PCR) has become an essential technique in the field of clinical laboratories, agricultural science, environmental science, and forensic science[1–5]. PCR requires thermal cycling, or repeated temperature changes between 2 or 3 discrete temperatures to amplify specific nucleic acid target sequences. To achieve such thermal cycling, conventional bench-top thermal cyclers

generally use the metal heating block powered by Peltier elements. While commercial PCR systems are improving heating and cooling rates to reduce amplification time, they are still relatively time-consuming (typically requiring an hour or more per amplification). This can be attributed to the larger thermal capacitance of a system that requires uniform heating 96- or 384-well plastic PCR plates and reaction volumes of several tens of microliters per well. Since fast/ultrafast PCR is highly desirable for applications such as timely diagnosis of infectious diseases, cardiac diseases, cancer, neurological disorder diseases, and rapid biowarfare and pathogen identification at the point-of-care (POC) level, many academic and industrial groups have been improving PCR systems[6–8], One commercial PCR system (LightCycler® 2.0) using air heating/cooling and capillary tubes can perform 30 thermal cycles from a minimum of 10 minutes to a maximum of 60 minutes, depending on sample volume. However, this system is not suitable for POC testing due to high power consumption (800 W maximum) and heavy weight (~22 kg). For POC diagnostics for global healthcare in resource-limited environments like in developing countries, a fast PCR system should be portable, robust, simple, and easy-to-use and characterized by low power consumption through miniaturization and integration. To date, the microfluidic-based fast/ultrafast PCR systems have been extensively investigated to reduce amplification time by decreasing sample sizes as well as by increasing heat transfer rates. Resistive heating with micro-fabricated thin film heaters is most commonly used to control temperature in the static microfluidic-based PCR system, in which the PCR runs in the microfluidic chamber[9–11]. However, this method requires a complicated fabrication process to integrate the thin film heater and resistance temperature detection sensor on chip. In the case of continuous-flow PCR on a chip, the PCR amplification occurs when the reaction samples pass thorough three discrete temperature zones. This method can produce faster thermal cycling for PCR, but requires an external syringe pump for continuous-flow control and lacks the ability to perform multiple reactions at the same time. Another approach includes infrared (IR) mediated non-contact selective heating of water droplets (pico- or nanoliter sample volume) for ultrafast thermal cycles using an IR laser or filament lamp, which harnesses the strong absorbance of water at wavelengths over 1000 nm[8]. However, droplet formation of the PCR mixture is a precise process prone to human error, a drawback of this method for POC testing.

More recently, efforts have been made to utilize the advantages of plasmonic photothermal heating of gold nanoparticles (AuNPs), using pulsed or continuous-wave laser excitation for photothermal therapy of cancer[12] and fast PCR[13], for example. But this arrangement is not ideal for POC testing, as it requires not only expensive lasers and detection systems, but also has a problem of controlling reliable AuNPs-based sample preparation.

In this chapter, we present a novel ultrafast photonic PCR method which combines the use of thin Au film as a light-to-heat converter and light-emitting diodes (LEDs) as a heat source Using this method, ultrafast thermal cycling (30 cycles; heating and cooling

rate of 12.79 ± 0.93 °C/sec and 6.6 ± 0.29 °C/sec, respectively) from 55 °C (temperature of annealing) to 95 °C/sec (temperature of denaturation) is accomplished within 5 minutes. Strong light absorption of the thin Au film generates heat due to the plasmonic photothermal light-to-heat conversion by photon- electron-phonon coupling at the thin Au film, followed by heating of surrounding solution with a maximum temperature of over 150 °C within 3 min. Ultrafast thermal cycling (30 cycles; heating and cooling rate of 12.79 ± 0.93 °C/sec and 6.6 ± 0.29 °C/sec, respectively) from 55 °C (temperature of annealing) to 95 °C/sec (temperature of denaturation) is accomplished within 5 minutes. Using this technique, we successfully demonstrate the amplification of λ- DNA. We propose that our PCR system would be ideal for POC diagnostics due to its ultrafast thermal cycling capability, multiplex PCR, low power consumption for the PCR thermal cycling (in current set-up, up to ~3.5 W), low cost and simple configuration for system level integration. Furthermore, our efficient photonic-based heating procedure could be generally integrated into a variety of devices or procedures, including on-chip thermal lysis and heating for isothermal amplifications.

3.3 PRINCIPLE OF PHOTOTHERMAL HEATING

Analytical study of the optical properties of metals

Metals have enormous densities of free electrons which do not experience resilience from the medium when interacting with light[14]. Furthermore, metals can be considered as plasmas because they consist of equal numbers of fixed positive ions in their centers and free electrons – An electrically neutral medium of charged particles is called a plasma. Especially, the noble metals such as copper (Cu), silver (Ag) and gold (Au) are in 11th group of the periodic table. The electron configuration of gold, for example, is $[Xe]4f^{14}5d^{10}6s^1$. The valence electrons in half-filled 6s bands cause the characteristic properties of gold such as electrical and thermal conductivity.

The electrons in half-filled 6s bands can be treated as plasmas and described by Drude-Lorentz model. We begin to consider the oscillation equation of a free electron in an external electric field $\varepsilon(t) = \varepsilon_0 e^{-i\omega t}$,

$$m_0 \frac{d^2x}{dt^2} + m_0\gamma \frac{dx}{dt} = -e\varepsilon(t) = -e\varepsilon_0 e^{-i\omega t}, \qquad (3.1)$$

where, m_0 is an electron of mass, x is the displacement of the electron, γ is a damping constant. Using $x = x_0 e^{-i\omega t}$ and equation 3.1, we obtain

$$x = \frac{e\varepsilon}{m_0(\omega^2 + i\gamma\omega)}. \qquad (3.2)$$

The dipole moment of a single electron is defined by $p = -ex$ and the polarization of the gas is equal to $P = Np = -Nex = -N\dfrac{e^2\varepsilon}{m_0(\omega^2+i\gamma\omega)}$, with the number of electrons per unit volume, N. From the definition of the electric displacement D, we can rewrite

$$\mathrm{D} = \epsilon_r\epsilon_0\varepsilon \tag{3.3}$$
$$= \epsilon_0\varepsilon + P \tag{3.4}$$
$$= \epsilon_0\varepsilon - \frac{Ne^2\varepsilon}{m_0(\omega^2+i\gamma\omega)}. \tag{3.5}$$

Using equation 3.3 and 3.5, we can obtain

$$\epsilon_r(\omega) = \epsilon_1(\omega) + i\epsilon_2(\omega) = 1 - \frac{Ne^2}{\epsilon_0 m_0}\frac{1}{(\omega^2+i\gamma\omega)} = 1 - \frac{\omega_p^2}{(\omega^2+i\gamma\omega)}, \tag{3.6}$$

where
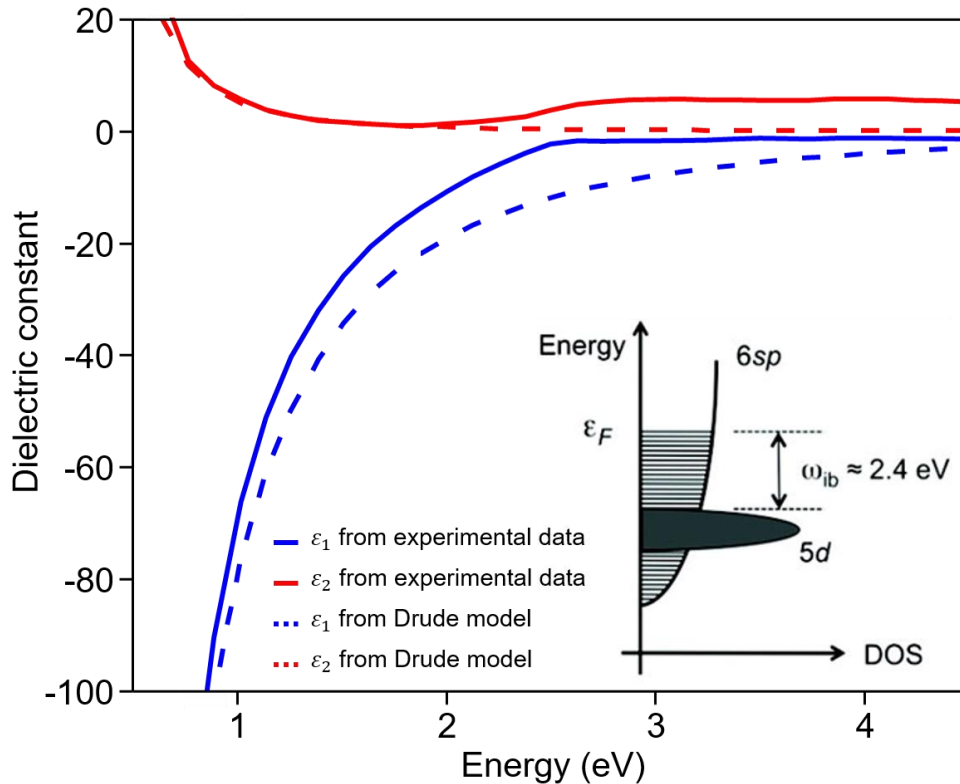
Figure 3.1 Complex dielectric constant of Au using the experimental data[17] and Drude model. Inset figure: Schematic representation of the band structure of Au. ε_F is the energy of Fermi level and ω_{ib} is the interband frequency of gold. Inset figure adapted from ref. 16 with permission. Copyright (2011) American Chemical Society.

$$\omega_p = \left(\frac{Ne^2}{\epsilon_0 m_0}\right)^{1/2}. \tag{3.7}$$

The Drude model explains the dielectric constants well in the near-IR region of spectrum, but it doesn't in near-UV and visible region due to interband transitions[15]. The interband transition energy is 2.4 eV. Thus, the dielectric constant of Au can be modified as

$$\epsilon_r(\omega) = \epsilon_{ib} + 1 - \frac{\omega_p^2}{(\omega^2 + i\gamma\omega)} = \epsilon_{ib,1} + 1 - \frac{\omega_p^2}{\omega^2 + \gamma^2} + i\left(\epsilon_{ib,2} + \frac{\omega_p^2\gamma}{\omega(\omega^2 + \gamma^2)}\right), \tag{3.8}$$

where ϵ_{ib} is the interband contribution[16]. Figure 3.1 shows the real and imaginary components of the dielectric constant for bulk Au and the experimental ϵ_2 is higher than that of the Drude model above 2.4 eV (≈ 516 nm of light) due to the interband transition[17]. From Beer's law, we can obtain the absorption coefficient:
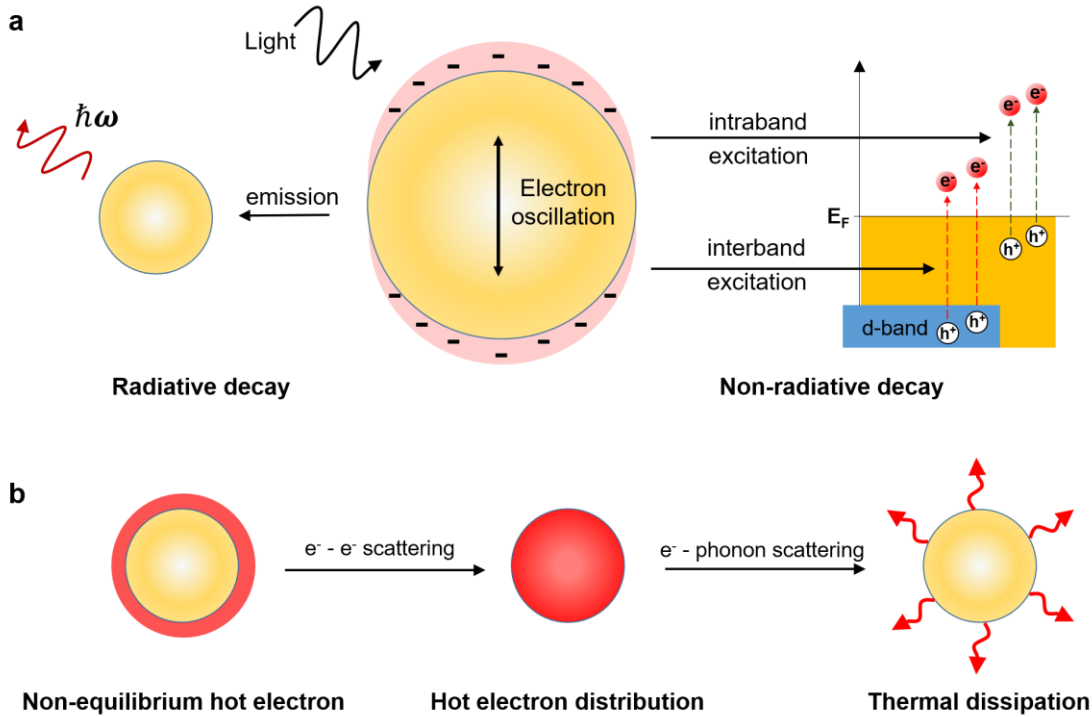
Figure 3.2 Schematic process of excitation and relaxation of metals after light absorption. (a) Illustration of radiative and non-radiative decay in metals following light absorption. (b) Schematic representations of non-radiative decay (photothermal process).

$$\alpha = \frac{4\pi\kappa}{\lambda} = \frac{2\pi\epsilon_2}{\lambda\sqrt{\epsilon_1}}, \tag{3.9}$$

,where λ is the vacuum wavelength of the light. Thus, the absorption is mainly determined by ϵ_2 and as shown in Fig. 3.1, the absorption of Au increases over 2.4 eV because the interband transition occurs.

Photothermal effect of Au

When metals are irradiated with a highly energetic light, light can be trapped efficiently, called the plasmon resonances[18]. Excited plasmons can decay either through radiative or non-radiative processes[19] as shown in Fig. 3.2a. Radiative decay can occur through re-emission of photons when the energy of electrons exceeds the work function of metals[20]. Because the work function for thin Au film was about 5.3 eV[21], the probability of radiative decay is quite low. Non-radiative decay happens by transferring the energy to hot electrons. Transfer of the energy falls into two processes, interband excitation within the conduction band and intraband excitation from other band to the conduction band[22]. Figure 3.2b shows the processes of non-radiative relaxation after generating hot electrons. The energy of hot electrons is distributed to lower-energy electrons via electron-electron scattering (i.e. Auger transitions) on a relaxation timescale in a range from 100 fs to 1 ps[23]. Then, these excited electrons interact with the phonons on several picosecond time scale, described well by the two-temperature model (TTM)[24]. Finally, the energy is transferred to the environment as a heat dissipation.

3.4 SIMULATION OF OPTICAL PROPERTIES ON THIN AU FILM

We performed a set of electromagnetic simulations to theoretically characterize the plasmonic photothermal light-to-heat conversion of our Au films. We used COMSOL Multiphysics software for electromagnetic simulation. The detailed materials properties and geometry for simulation are shown in Table 3.1 and Fig. 3.3. Thin Au film was placed

	Density, ρ (kg/m^3)	Heat capacity, C (J/kg · °C)	Thermal conductivity, k (W/m · °C)
Gold	19,300	129	317
PMMA	1,180	1,420	0.19
Water	998	4,180	0.6

Table 3.1 Physical properties of material used in the simulation.

on a PMMA substrate and water was on the top of Au film. Different thicknesses (10, 20, 40, 80, and 120 nm) of thin Au film were applied to the simulation to calculate the absorption of the Au films and subsequent resistive heat generation. The plane wave with x-polarized Electric field traveled in the positive z direction in the coordinate (Fig. 3.3). The permittivity of Au used in this study was referred from Johnson and Christy[17]. The permittivity of PMMA and water were 3 and 1.77, respectively. We calculated the electromagnetic (EM) field and resistive heat distributions for 10 nm and 120 nm thick Au films on a PMMA substrate. As expected from skin depth, $\delta = \sqrt{\dfrac{2}{\mu\omega\sigma}}$ (ω: angular frequency, μ: permeability, σ: conductivity), the thickness of thin Au film determines the amount of light to heat conversion. Upon a normal incidence of a 450 nm wavelength light source, the 10 nm thick Au film transmitted an enormous amount of EM energy (Fig. 3.4a), and the heat conversion energy was saturated along the film depth (Fig. 3.4c). However, the 120 nm thick Au film absorbs most of the incident light (Fig. 3.4b) and subsequently generates more heat in the Au film by converting light into heat (Fig. 3.4d). Dissipative heat was obtained by using the heat source density given by $q(r) = \dfrac{1}{2}Re[J \cdot E]$, where J is
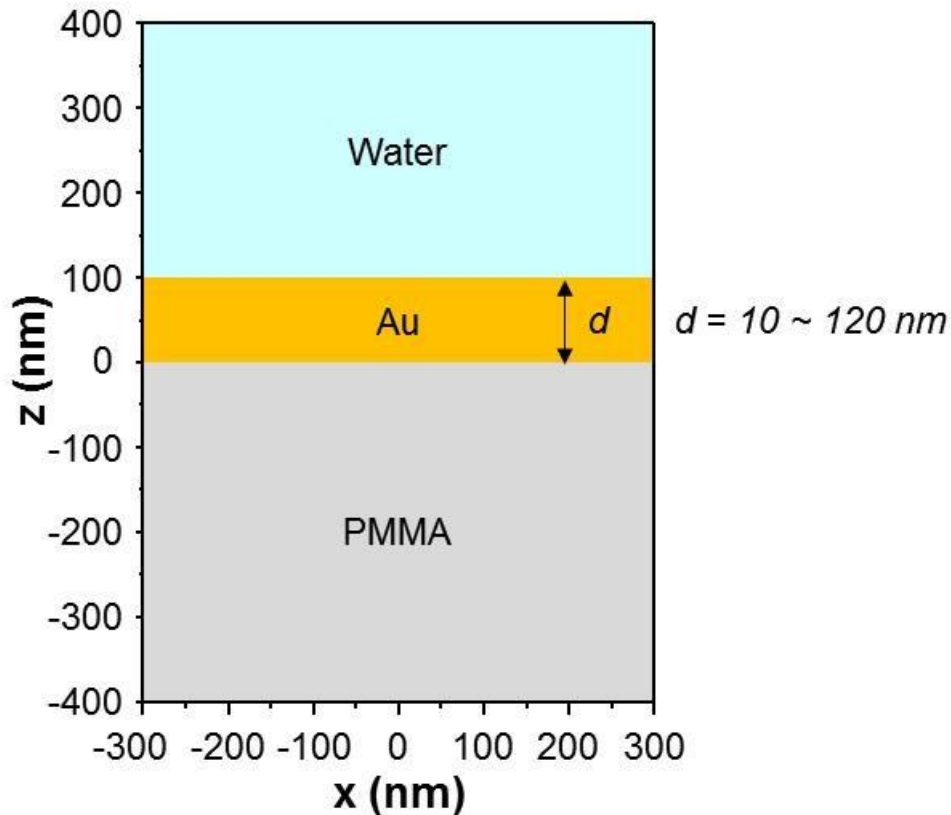

Figure 3.3 Geometry for the simulation of electromagnetic field and resistive heat distribution in the thin Au film with electromagnetic radiation. The thickness of thin Au film was varied ranging from 10 to 120 nm.
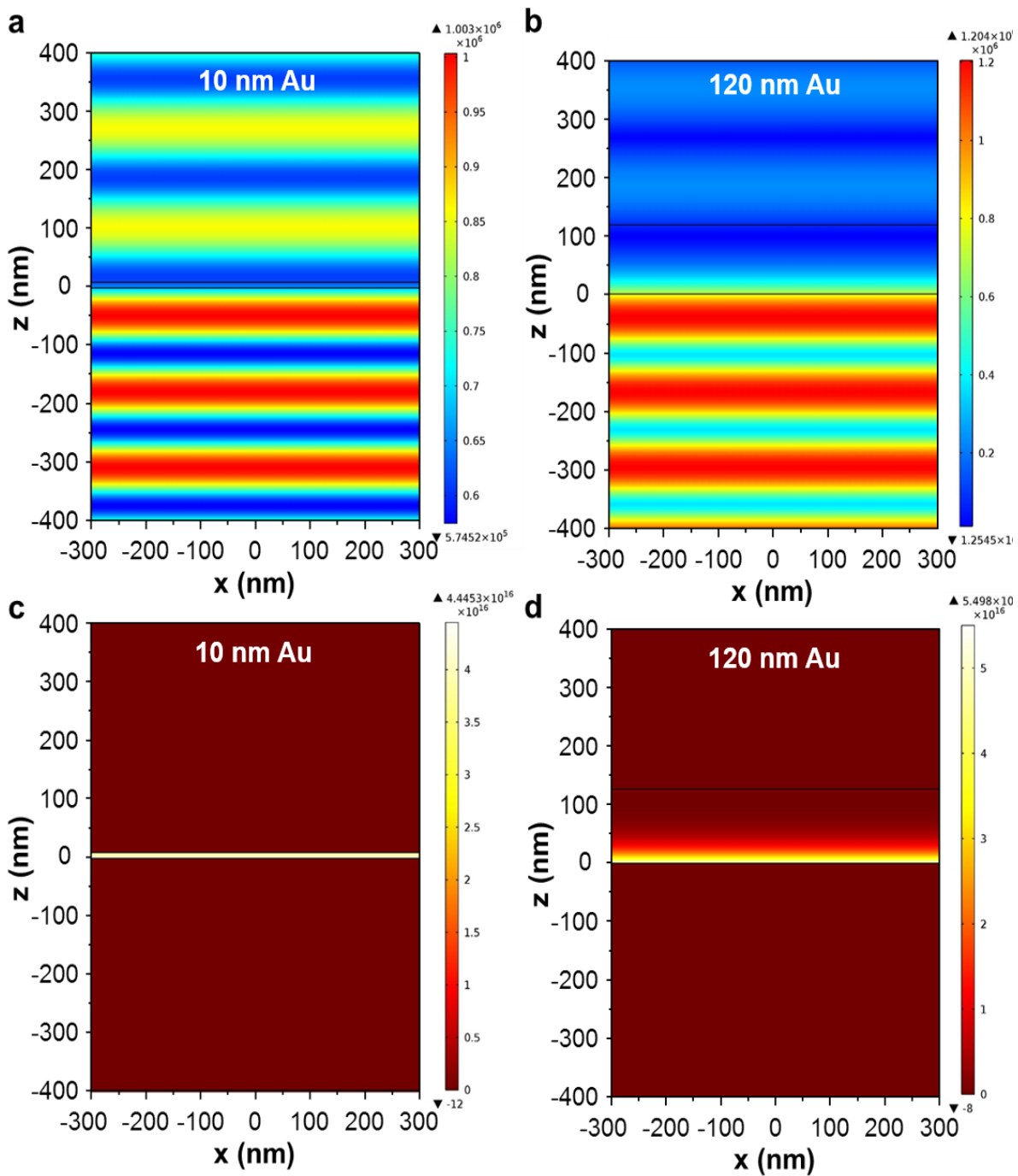
Figure 3.4 Simulation for the heat generation on the thin Au films following electromagnetic radiation. (a – b) Calculated electromagnetic field distributions for the 10 nm (a) and 120 nm (b) thickness of Au films on PMMA substrate. The wavelength of light is 450 nm with the normal incident angle. (c – d) Corresponding resistive heat distribution for the 10 nm (c) and 120 nm (d) thick Au films on PMMA substrate..
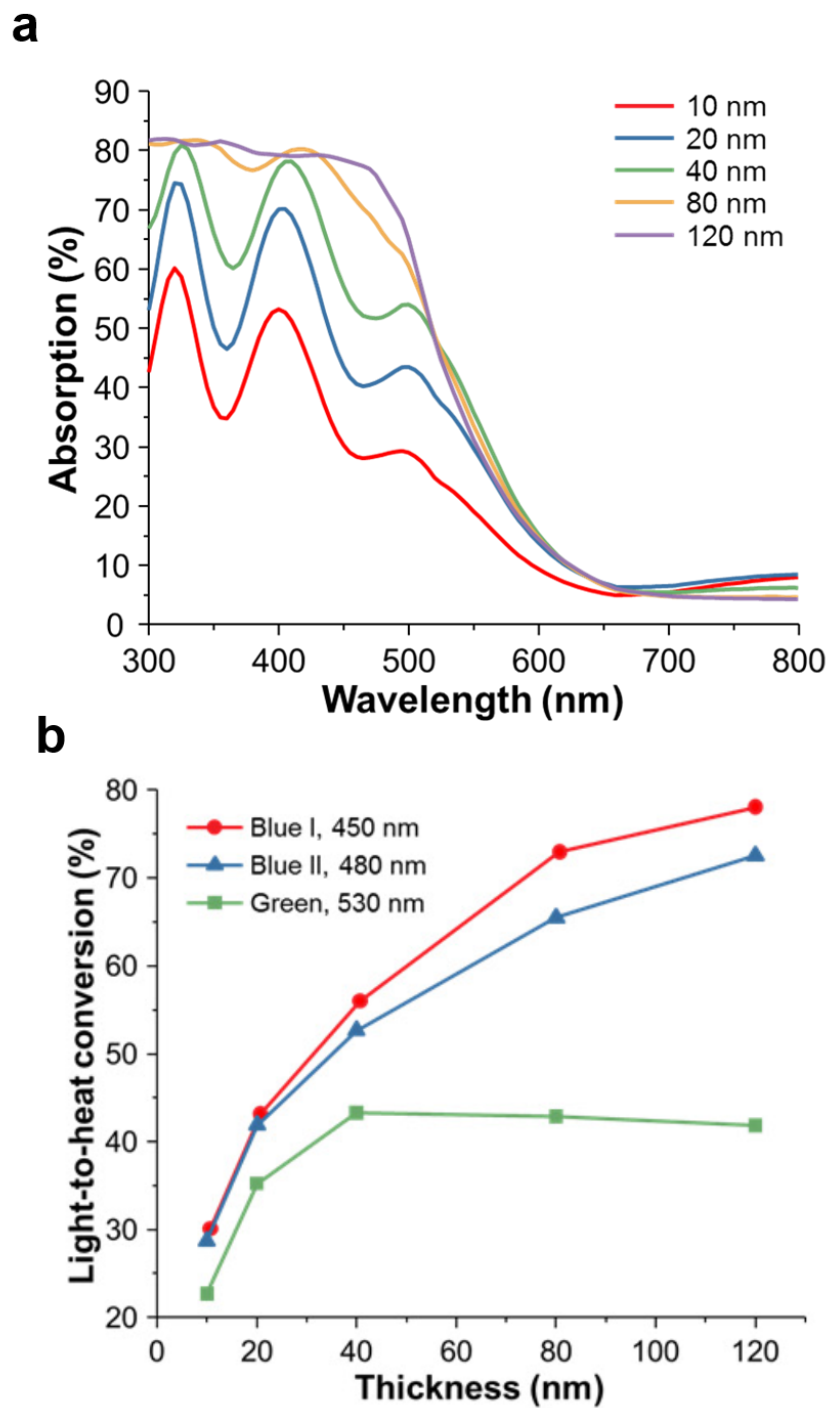
Figure 3.5 (a) Calculated absorption spectra of the thin Au films with different thickness. (b) Light-to-heat conversion efficiency of the thin Au films averaged over emission wavelength from 3 different LEDs as a function of Au films thickness.

the current density and E is the electric field. Figure 3.5a shows that an increase in thickness of thin Au film, ranging from 10 to 120 nm, corresponds to an increase in optical absorption. Significant increase of optical absorption below 540 nm wavelength could be attributed to the plasmonic electron resonance of gold[25]. As a result, the averaged light-to-heat conversion efficiency over emission wavelength from each LEDs increased with increased Au film thickness for 3 different LEDs as shown in Fig. 3.5b. It is noteworthy that the blue LEDs with peak emission wavelength of 450 nm showed highest light-to-heat conversion efficiency with thin Au film.

3.5   EXPERIMENTS OF PHOTOTHERMAL HEATING ON THE AU-COATED PMMA PCR WELLS

Fabrication and set-up of the thin Au film deposited PMMA PCR wells

Our photonic PCR thermal cycler used a LEDs as a heating source, PMMA PCR wells deposited with thin Au film, and a lens to focus the excitation shown in Fig. 3.6. 4 mm-thick poly(methyl methacrylate) (PMMA) sheets were cut with a laser cutting system (Universal Laser System, Inc., USA) to make a reaction well with a 4-mm diameter. The
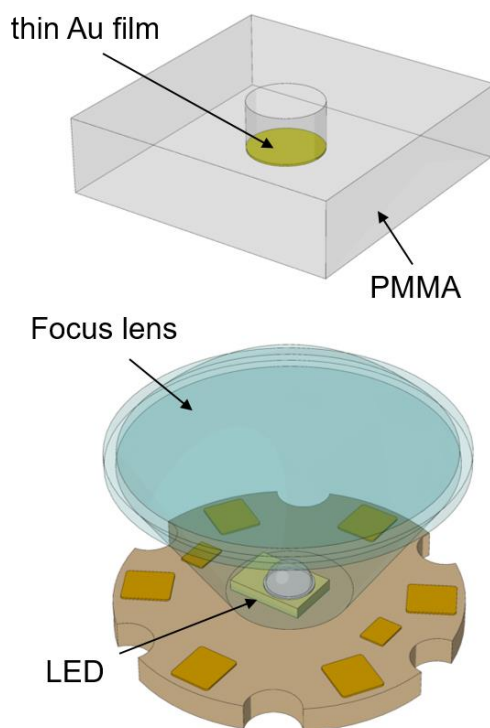

Figure 3.6 Schematic illustration of an experimental setup for the LED-driven ultrafast photonic PCR. Continuous-wave light from the blue LEDs is focused on the thin Au film through the focus lens. The peak wavelength of LEDs was 450 nm.

1.5 mm-thick bottom PMMA sheet and top reaction wells were bonded together using the thermal bonding. Thermal bonding was performed at 84 ℃ with pressure of 1.0 metric ton after UV/Ozone treatment of PMMA sheet for 10 minutes. The thin Au films of different thicknesses were deposited by electron beam evaporation under base pressure of 2×10^{-7} Torr.

Experiments of photothermal heating of Au-coated PMMA

The optical absorption spectra of thin Au films with different thicknesses deposited on PMMA substrate is shown in Fig. 3.7. Our simulation results could help us determine when the strongest light absorption occurs, as this is critical to maximizing photothermal heating. As the thickness of thin Au film increases, the optical absorption also increases, showing 65 % absorption at the peak wavelength (450 nm) of excitation LEDs in the 120 nm-thick Au film. The light from the LEDs was continuous-wave and randomly polarized. Therefore, the efficiency of light-to-heat conversion would be lower in this case than a pulsed laser, because as electrons are excited to higher energy states, the probability of further excitation decreases. Despite its possible lower light-to-heat conversion efficiency than a pulsed light source, however, LEDs require minimal power consumption and are extremely low in cost compared to laser sources, making LEDs an ideal PCR heating source for POC testing. The maximum power consumption of an LED is around 3.5 W at 1,000 mA injection current. Figure 3.8a shows the temperature profiles of a 10 μl volume of solution (here, glycerol was used to show maximum heating temperature) with different thickness thin Au films at a fixed injection current of 500 mA. The maximum temperatures are increased as the thickness of thin Au film increases from 10 nm to 120 nm due to the increasing optical absorption. The photothermal heating of the 120 nm-thick Au film was further characterized as a function of injection current as shown in Fig. 3.8b, because the heating rate is determined by the amount of dissipated power (i.e., an injection current of LEDs). Figure 3.9 summarizes the temperature of a solution after heating with different thickness Au films and varying injection current for 3 minutes. These results clearly indicated that the maximum temperatures are increased with an increase of Au film thickness to 120 nm and an increase of injection current to 1,000 mA.
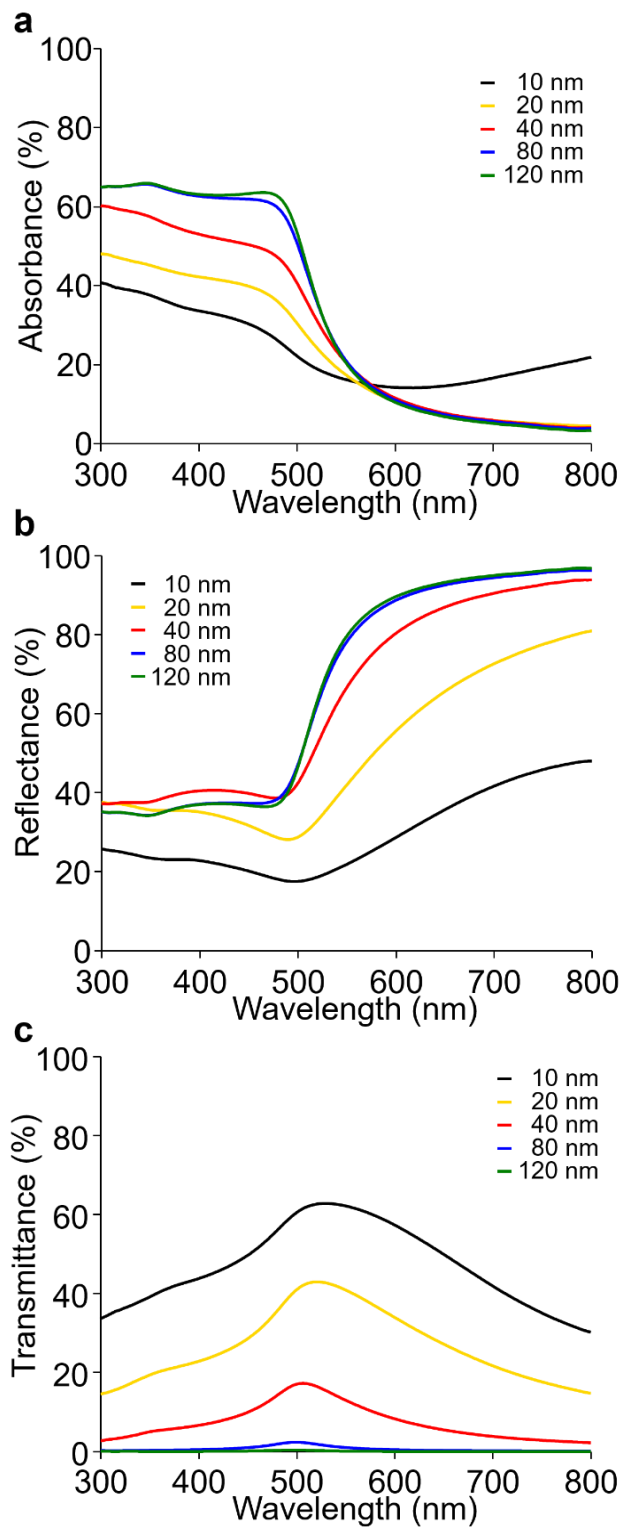
Figure 3.7 Absorption (a), Reflectance (b), and Transmittance (c) spectra of thin Au films on PMMA with different thicknesses of Au.
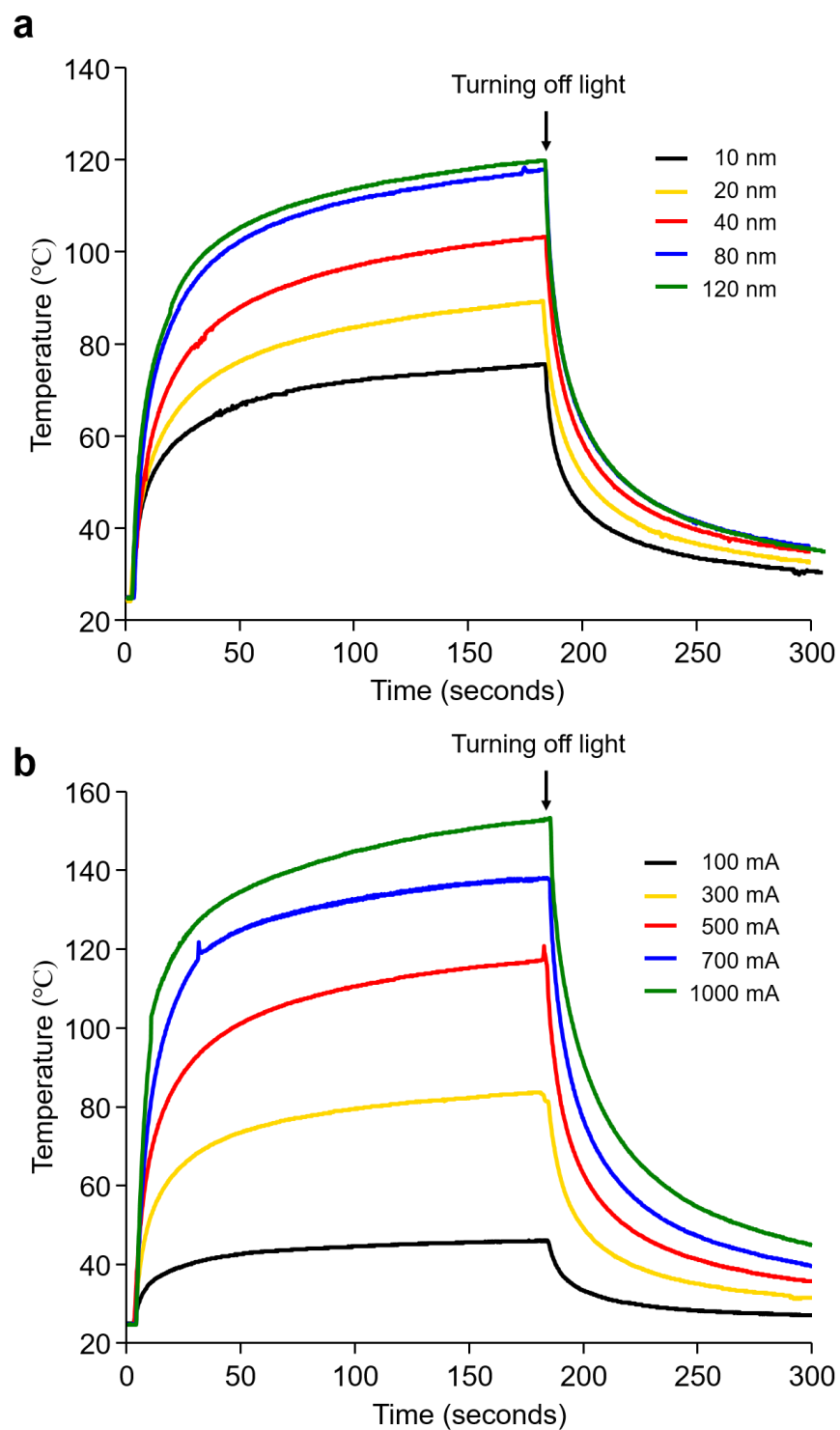
Figure 3.8 (a) Temperature profiles of liquids with different thicknesses of Au film illuminated by the blue LED at 500 mA injection current. (b) Temperature profiles of liquids on a 120 nm-thick Au film with different injection current of LEDs at 120 nm-thick Au film. The peak wavelength of blue LED we used was 450 nm.
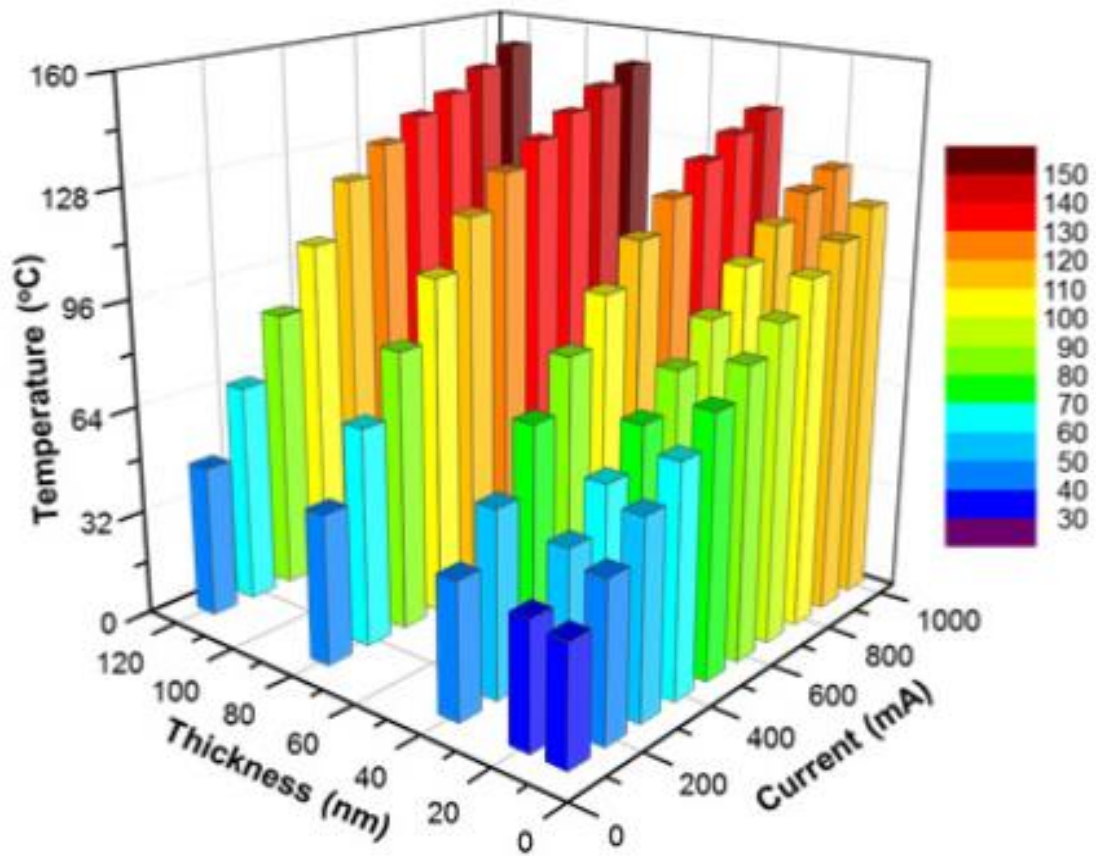
Figure 3.9 Comprehensive 2D map showing the distribution of liquid temperature with different thickness of the thin Au film and injection current of LEDs after heating for 3 minutes.

3.6 LED-DRIVEN PHOTONIC PCR THERMAL CYCLER AND NUCLEIC ACID AMPLIFICATION

Preparation of the PCR reagent and DNA template

The forward (GCCTAACACATGCAAGTCGAA) and reverse (CAGGCAGTTTCCC AGACATTAC) primers were purchased from Integrated DNA technologies. KAPA2G Fast DNA polymerase (5 U/μl), 5× KAPA2G Buffer A and dNTP Mixture (10×10^{-3} M) were purchased from KAPA Biosystems. DNA extraction protocols were followed as instructed in the DNeasy Blood & Tissue Kit (QIAGEN, CA, USA) after culturing *E. coli* at 37 ℃ for 16 hours. The PCR reagents for this system comprised of 1 μl KAPA2G DNA polymerase, 4 μl 5× KAPA2G buffer A, 1 μl dNTP mixture,), 2 μl of dNTP mixture, 1 μl each of forward and reverse primers (final concentration: 500 nM), 2 μl of BSA (final concentration: 3 mg/ml), and 9 μl of PCR grade water The 20 μL of PCR mixture was placed within an Au- coated PMMA PCR wells for photonic PCR, and then covered with 30 μL of mineral oil to prevent evaporation during thermal cycling. After amplification, the amplification of amplicons was determined by gel electrophoresis using E-Gel® 2 % agarose gels with SYBR Safe (Invitrogen, USA).

Ultrafast photonic PCR cycles

The LEDs (a peak wavelength of 447.5 nm, Luxeon Inc., CANADA) were used for plasmonic photothermal heating of the thin Au film with a Keithley 2400 source meter. To focus the light from the LEDs, the Carclo 20 mm fiber coupling optic (part number: 510356) was employed. The temperature of a solution was monitored and recorded in real time by the type-K insulated thermocouple purchased from OMEGA Engineering (part number, 5SC-TT-K-40-36) for thermal cycling. Temperature cycling using an LED, 80 mm cooling fan, source meter and thermocouple was controlled through a microcontroller (Arduino UNO, USA).

In order to determine maximum heating and cooling rates, a thermal cycle was performed whereby the solution (here, 5 μl of PCR mixture covered with 30 μl of mineral oil) temperature was rapidly cycled between 55 ℃ and 95 ℃. The temperature range mirrors the same denaturation (95 ℃) and annealing (55 ℃) temperatures. Fig. 4a shows the ultrafast photonic 30 cycles within 5 minutes. Using the thermal cycling result, heating and cooling rates were calculated by measuring the temperature difference between successive temperature maxima and minima, then dividing by the time interval between them. The average rates and sample standard deviations were obtained as shown in Fig. 4b. The average heating and cooling rates obtained are 12.79 ± 0.93 ℃/sec and 6.6 ± 0.29 ℃/sec, respectively. The amplification of extracted DNA was performed to verify our photonic PCR method. After running PCR reactions as shown in Fig. 4c, the amplicons were visualized by E-Gel® 2 % agarose gels with SYBR Safe. Lane 1 represents the DNA
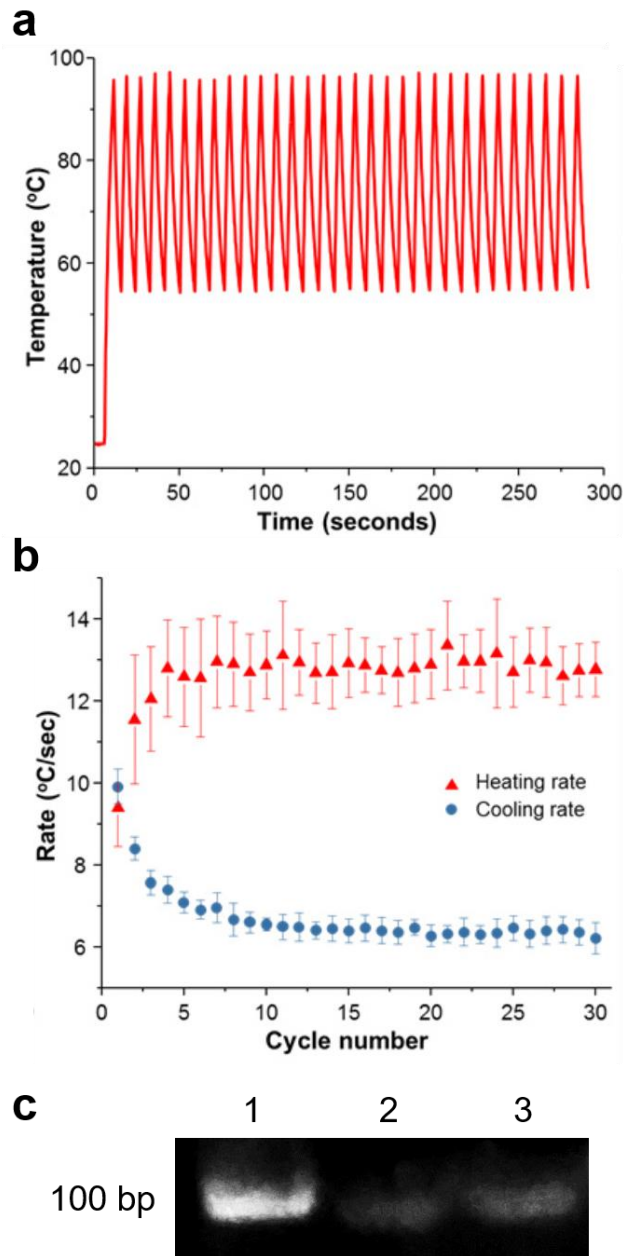
Figure 3.10 Ultrafast thermal cycling and DNA amplification. (a) Representative temperature profiles of 30 ultrafast photonic PCR thermal cycles from 95 ℃ (denaturation) to 55 ℃ (annealing and extension). The 5 µL of PCR buffer was covered with 20 µL of mineral oil to prevent evaporation during thermal cycling. (b) Heating and cooling rates obtained from the ultrafast photonic thermal cycling. Heating and cooling rate were 12.79 ± 0.93 ℃/sec and 6.6 ± 0.29 ℃/sec, respectively. (c) 2 % agarose gel results demonstrating the formation of product from the photonic PCR thermal cycler in comparison with bench-top thermal cycler using extracted DNA.

marker, lane 2 was the PCR product from ultrafast photonic PCR with different cycle numbers (94 for 0 sec, 62 for 0 sec), lane 3 contained positive controls produced from a standard thermal cycle condition (94 or 1 sec, 62 for 1 sec, 60 cycles) by a bench-top thermocycler (Bio-Rad C1000 Thermal Cycler). A single major band (100 bp) was detected near 100 bp in photonic PCR. This indicated that the amplicon was successfully amplified using our ultrafast photonic PCR method. The weak band intensity from the PCR product amplified by photonic PCR could be attributed to the lower amplification efficiency compared to a traditional bench-top thermal cycler. Currently, only thin Au film acts as a 2-dimensional photothermal heater, leading to a temperature gradient of the solution, leading to potentially lower amplification efficiency of PCR. This limitation can be improved by utilizing 3-dimensional substrate in the PCR chamber for uniform photothermal heating of PCR mixture. Amplification time as well as reagent consumption could be further reduced, simultaneously improving the efficiency of the PCR reaction by faster molecular diffusion and uniform solution temperature.

3.7 CONCLUSION

In conclusion, we demonstrate a novel ultrafast photonic PCR through plasmonic photothermal heating of thin Au films driven by LEDs. We designed and fabricated a thin Au film-based light-to-heat converter to heat a PCR solution over 150 by harnessing gold plasmon-assisted high optical absorption. We achieved ultrafast thermal cycling from 55 °C (annealing) to 95 °C (denaturation) within 5 minutes for 30 cycles with ultrafast heating (12.79 ± 0.93 °C/sec) and cooling (6.6 ± 0.29 °C/sec) rates. Nucleic acid amplification using our ultrafast photonic PCR thermal cycler was successfully demonstrated. We propose that this simple, robust and low cost photonic PCR technique, with ultrafast thermal cycling capability, would be ideal for POC molecular diagnostics, because the photonic PCR technique can meet the "ASSURED" criteria[26]: 1. Affordable: cheaper system with a LED and lens. 2. Smaller: compact and light PCR system without a heating block. 3. Simple step with disposable PCR chip. 4. User-friendly interface with LED driver and display. 5. Rapid and robust PCR without environmental stress. 6. Equipment-free: only LED and microcontroller modules with cellphone camera. 7. Durable in harsh environments & low power consumption. As the current set-up is based on only one PCR well, future work should focus on integrating more wells and LED array to allow for high-throughput and multiplexed amplification, as well as optimizing the PCR reaction chamber for uniform heating.

3.8 REFERENCES

1.   Postollec, F., Falentin, H., Pavan, S., Combrisson, J. & Sohier, D. Recent advances in quantitative PCR (qPCR) applications in food microbiology. Food Microbiology 28, 848–861 (2011).

2.   Horsman, K. M., Bienvenue, J. M., Blasier, K. R. & Landers, J. P. Forensic DNA analysis on microfluidic devices: A review. Journal of Forensic Sciences 52, 784–799 (2007).

3.   Zhang, C. & Xing, D. Miniaturized PCR chips for nucleic acid amplification and analysis: Latest advances and future trends. Nucleic Acids Res. 35, 4223–4237 (2007).

4.   Ottesen, E. A., Hong, J. W., Quake, S. R. & Leadbetter, J. R. Microfluidic Digital PCR Enables Multigene Analysis of Individual Environmental Bacteria. Science (80-.). 314, 1464–1467 (2006).

5.   Heyries, K. A. et al. Megapixel digital PCR. Nat. Methods 8, 649–651 (2011).

6.   Lyon, E. & Wittwer, C. T. LightCycler Technology in Molecular Diagnostics. J. Mol. Diagnostics 11, 93–101 (2009).

7.   Pak, N., Saunders, D. C., Phaneuf, C. R. & Forest, C. R. Plug-and-play, infrared, laser-mediated PCR in a microfluidic chip. Biomed. Microdevices 14, 427–433 (2012).

8.   Huhmer, A. F. R. & Landers, J. P. Noncontact infrared-mediated thermocycling for effective polymerase chain reaction amplification of DNA in nanoliter volumes. Anal. Chem. 72, 5507–5512 (2000).

9.   Selva, B., Mary, P. & Jullien, M. C. Integration of a uniform and rapid heating source into microfluidic systems. Microfluid. Nanofluidics 8, 755–765 (2010).

10.   Jiao, Z. J., Huang, X. Y. & Nguyen, N.-T. Manipulation of a droplet in a planar channel by periodic thermocapillary actuation. J. Micromechanics Microengineering 18, 45027 (2008).

11.   Lagally, E. T., Medintz, I. & Mathies, R. A. Single-molecule DNA amplification and analysis in an integrated microfluidic device. Anal. Chem. 73, 565–570 (2001).

12.   Huang, X., El-Sayed, I. H., Qian, W. & El-Sayed, M. A. Cancer cell imaging and photothermal therapy in the near-infrared region by using gold nanorods. J. Am. Chem. Soc. 128, 2115–2120 (2006).

13.   Roche, P. J. R. et al. Demonstration of a plasmonic thermocycler for the amplification of human androgen receptor DNA. Analyst 137, 4475–81 (2012).

14.   Fox, M. Optical properties of solids. Oxford master series in condensed matter physics (2001). doi:10.1103/PhysRevB.4.3425

15.   Hartland, G. V. Optical studies of dynamics in noble metal nanostructures. Chemical Reviews 111, 3858–3887 (2011).

16.   Alvarez, M. M. et al. Optical Absorption Spectra of Nanocrystal Gold Molecules. J. Phys. Chem. B 101, 3706–3712 (1997).

17.   Johnson, P. B. & Christy, R. W. Optical constants of the noble metals. Phys. Rev. B 6, 4370–4379 (1972).

18.   Clavero, C. Plasmon-induced hot-electron generation at nanoparticle/metal-oxide interfaces for photovoltaic and photocatalytic devices. Nat. Photonics 8, 95–103 (2014).

19.   Li, X., Xiao, D. & Zhang, Z. Landau damping of quantum plasmons in metal nanostructures. New J. Phys. 15, (2013).

20. Inagaki, T., Kagami, K. & Arakawa, E. T. Photoacoustic observation of nonradiative decay of surface plasmons in silver. Phys. Rev. B 24, 3644–3646 (1981).
21. Sachtler, W. M. H., Dorgelo, G. J. H., Holscher, A. A. The work fuction of gold. Surf. Sci. 5, 221–229 (1966).
22. Brongersma, M. L., Halas, N. J. & Nordlander, P. Plasmon-induced hot carrier science and technology. Nat. Nanotechnol. 10, 25–34 (2015).
23. Watanabe, K., Menzel, D., Nilius, N. & Freund, H. J. Photochemistry on metal nanoparticles. Chem. Rev. 106, 4301–4320 (2006).
24. Sun, C. K., Vallée, F., Acioli, L. H., Ippen, E. P. & Fujimoto, J. G. Femtosecond-tunable measurement of electron thermalization in gold. Phys. Rev. B 50, 15337–15348 (1994).
25. Jain, P. K., Lee, K. S., El-Sayed, I. H. & El-Sayed, M. A. Calculated Absorption and Scattering Properties of Gold Nanoparticles of Different Size, Shape, and Composition: Applications in Biological Imaging and Biomedicine. J. Phys. Chem. B 110, 7238–7248 (2006).
26. Peeling, R. W. & Mabey, D. Point-of-care tests for diagnosing infections in the developing world. Clinical Microbiology and Infection 16, 1062–1069 (2010).

CHAPTER 4

ANALYSIS OF HEAT TRANSFER IN PHOTONIC PCR

4.1 INTRODUCTION

A comprehensive heat transfer simulation of the photonic PCR was carried out to improve the performance of the photonic PCR. Control of temperature is one of important issues for PCR. In PCR, repeating the three discrete steps – DNA denaturation, annealing of primer and polymerase extension – results in exponential amplification of a target DNA[1]. PCR generally took 1-2 hours for amplification but there has been an extensive interested in research on rapid PCR[2–5]. In the early stage of researches, not biochemistry but instrumentation was considered a limitation of rapid PCR[6]. With emerging microfluidics,
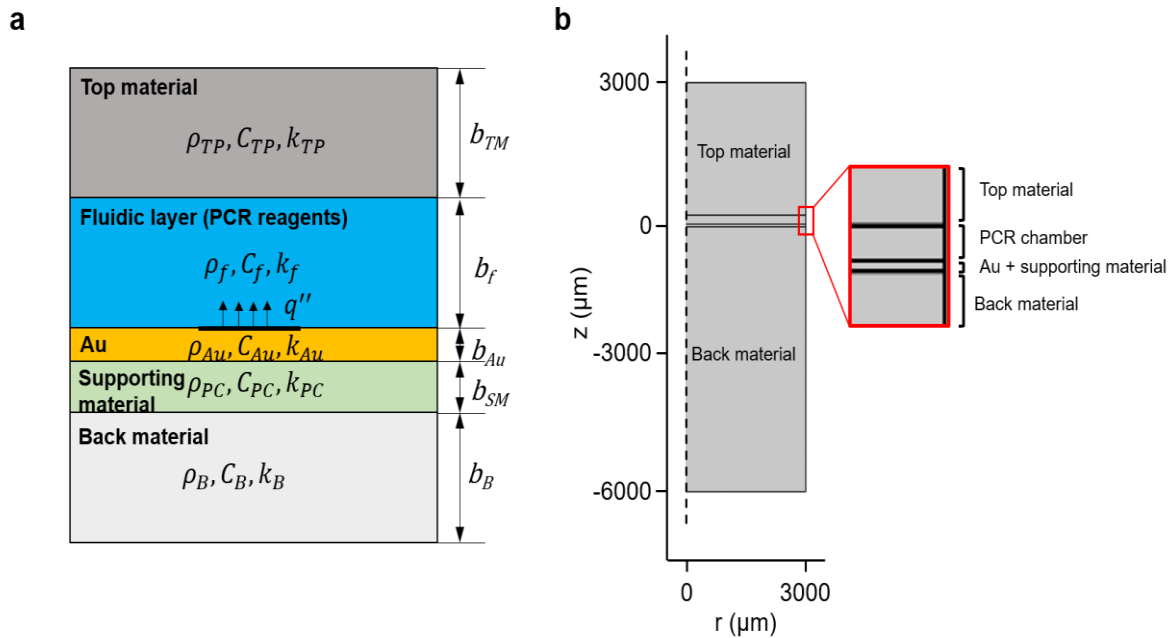
Figure 4.1 Geometry for the simulation of heat transfer in photonic PCR. (a) Schematic of the phonic PCR configuration (not scaled). (b) Schematic of physical model of photonic PCR. $b_{TM} = 3000$ μm, $b_f = 200$ μm, $b_{Au} = 0.08$ μm, $b_{SM} = 80$ μm, and $b_B = 6000$ μm.

however, precise manipulation of sub-nanoliter fluidic volume can reduce the reaction volume of PCR, which enables to reduce the total time of PCR reaction[7–10]. For example, 1-µl sample was amplified on 35 cycles in 30 seconds[6]. However, to amplify 1-µl sample, two different 4.26-liters of hot water (95.5 °C and 75 °C) were used for temperature control and a stepper motor was required for moving samples, which is not efficient method for scalability and Point-of-Care settings. Thus, the challenging of rapid PCR is not only to simply accomplish rapid thermocycling, but also to consider simple configuration of instrumentation, physical extensibility for diverse applications. In this meaning, photonic PCR opened up new possibilities for rapid PCR. However, as thermal cycle increases, heating and cooling rates get slow. Thus, comprehensive understanding of the heat transport mechanisms in the photonic PCR is critical for optimization. The photonic PCR requires a light source, an optical heat converter, precise temperature control, and cooling materials. Therefore, one of the most crucial modeling parameters investigated in this chapter is the temperature of fluid with time when heat flux is generated from the thin metal film. In addition, the dissipation of heat is evaluated when the light is turned off. Unlike mass transport analysis, the simulation of heat transfer in microfluidics involves some challenges[11–14]. Due to thermal diffusion, the modeling domain should be extended from the region of interest such as the fluidic domain to the materials surrounded the area of interest. Consequently, a comprehensive, thermal computational model of the photonic PCR was carried out.

	Density, ρ (kg/m^3)	Heat capacity, C (J/kg · °C)	Thermal conductivity, k (W/m · °C)	Thermal diffusivity, α (mm^2/s)
AAO	2840	867	1.3	0.528
Air	1.205	1005	0.0257	21.2
Aluminum	2700	896	167	69.0
Gold	19300	129	317	127
Oil	800	1670	0.1	0.0749
PMMA	1180	1420	0.19	0.113
Polycarbonate	1200	1215	0.21	0.144
Water	998	4180	0.6	0.143

Table 4.1 Thermal properties of materials.

4.2   THERMAL MODELING OF PHOTONIC PCR

The configuration of photonic PCR was illustrated in Fig. 4.1. In summary, the chamber of photonic PCR was made by top material and Au was deposited on the supporting material. For efficient heat exchange, the back material was placed below supporting material for thermal isolation (when heating) and cooling material (when cooling). A thin Au film below fluidic layer (PCR reagents) generated heat energy (q'') when the light came to Au. Then, heat energy was transmitted to from Au to fluidic layer and supporting material. The governing equations are as follows:

$$\rho_i C_i \frac{\partial T}{\partial t} + \rho_i C_i \boldsymbol{V} \cdot \nabla T = \nabla \cdot (k_i \cdot \nabla T) \tag{4.1}$$

where ρ is the density of material, C the heat capacity, T is the temperature, k is the thermal conductivity, $\boldsymbol{V}$ the velocity vector, and subscript i describes the specific materials. The thermal properties of the materials can be found in Table 4.1. Due to no flow in fluidic domain, the equation 4.1 can be simply written as:

$$\frac{1}{\alpha_i} \frac{\partial T}{\partial t} = \nabla^2 T \tag{4.2}$$

, where α is the thermal diffusivity.

4.3   EVALUATION OF EFFECTS OF OPTICAL ABSORPTION OF PHOTONIC PCR

We investigated the effect of optical absorption of Au on thermal cycle of photonic PCR. When light comes from the bottom of the photonic PCR, light is absorbed by Au at the interface between Au and supporting materials. Thus, the absorption is related to the thickness of gold and the supporting materials[15]. The energy absorbed by Au a function of the Poynting vector and can be calculated by

$$P_{abs} = \frac{1}{2} \omega \varepsilon'' |E|^2 \tag{4.2}$$

, where ω is the frequency of the incident electromagnetic wave, ε'' is the imaginary dielectric function, and $|E|^2$ is the magnitude of the electromagnetic field[16]. We simulated the 2D heat transfer model of the photonic PCR with the representative three cases: 25, 50, and 100 % absorption of Au. Top material, supportive material, and back material were taken as PMMA, AAO, and oil, respectively.

As seen in Fig. 4.2, the cycling time reduced as the absorption of Au increased. First of all, with higher absorption of Au, Au generated more heat energy, which decreased the heating thermal cycling time. That is, the heating ramping rate increased as the absorption of Au increased as shown in Fig. 4.3a and Fig 4.4. Interestingly, the cooling ramping rate also increased as the absorption of Au increased even though the all materials in system were unchanged in Fig. 4.3b. This is related the spatial temperature distribution of the photonic PCR. As the absorption of Au increased, the time required for the heating thermal cycle decreased. As a result, the total energy transferred from the PCR chamber to the back material decreased. Thus, the temperature gradient around the PCR chamber became steeper as the absorption of Au increased as shown in Fig 4.5.
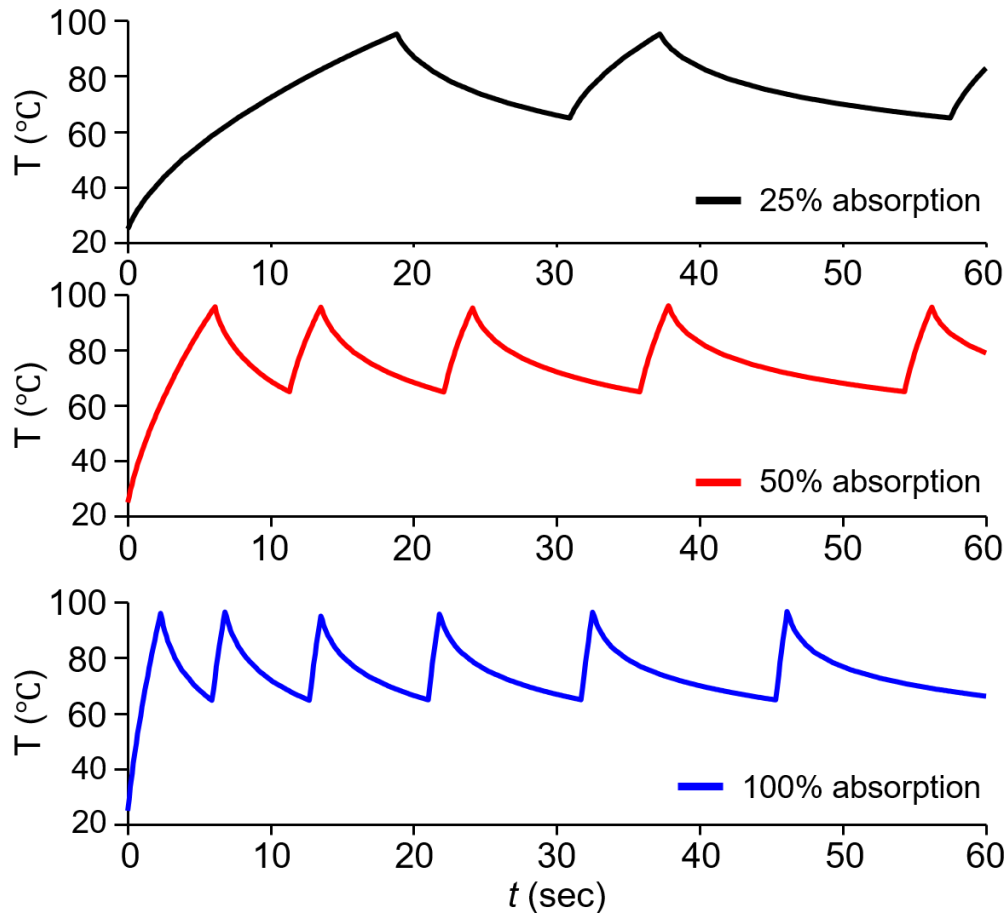
Figure 4.2 Calculated temperature profiles with different absorption (25 %, 50 %, and 100 %) of Au from 95 ℃ (denaturation) and 65 ℃ (annealing / extension) in 1 minute.
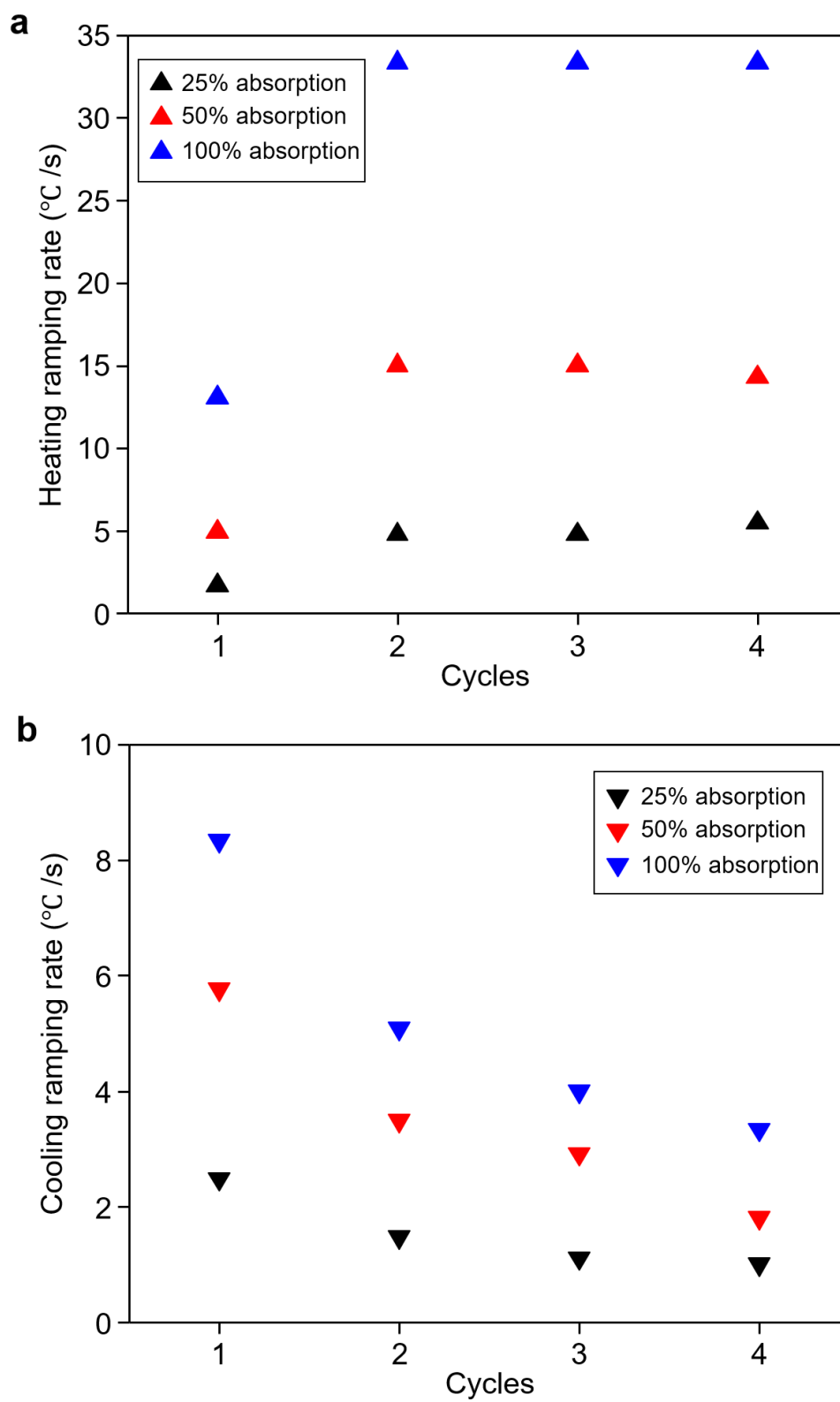
Figure 4.3 The heating ramping rate (a) and the cooling ramping rate (b) of the photonic PCR with different absorption of Au

a 25 % absorption
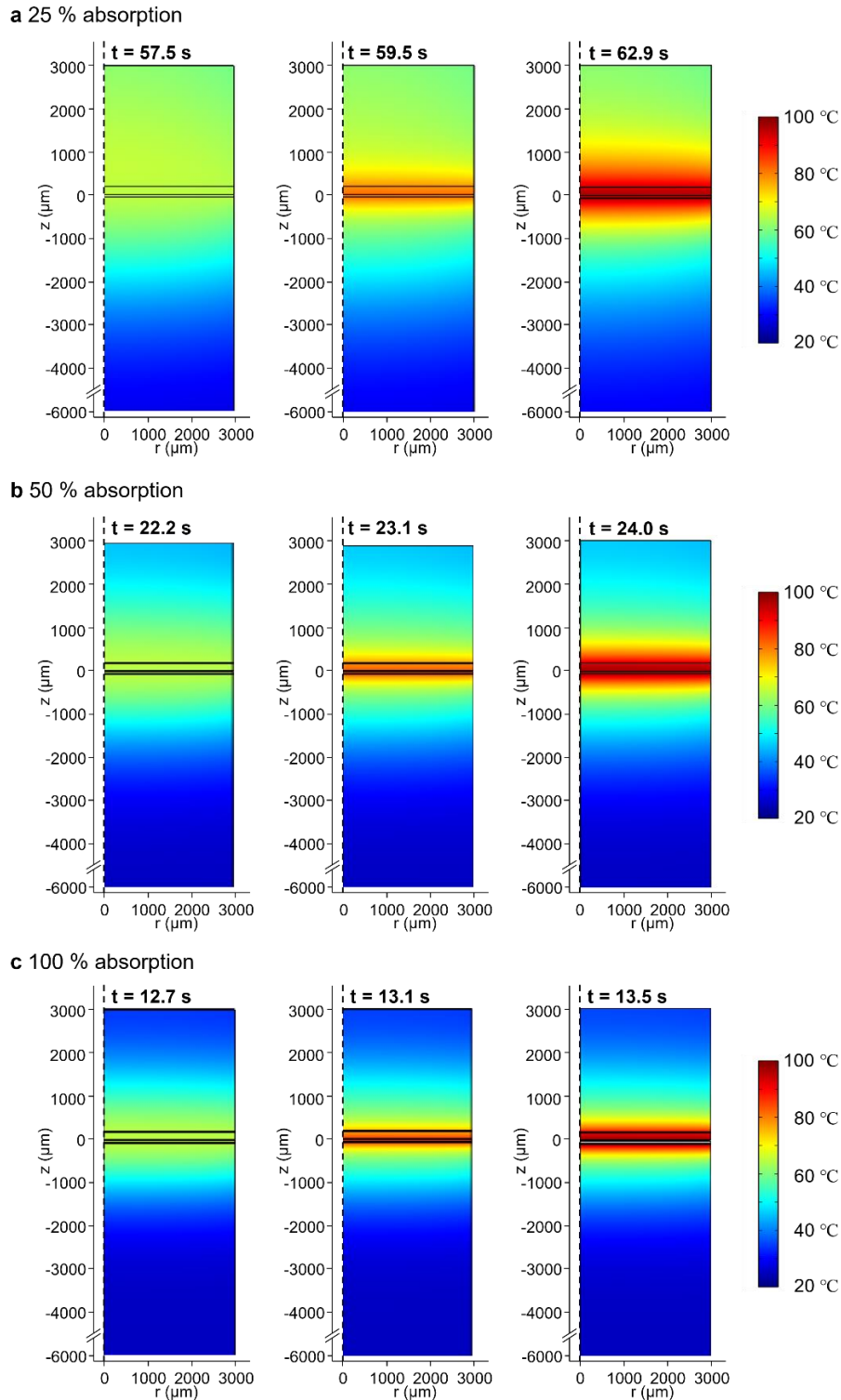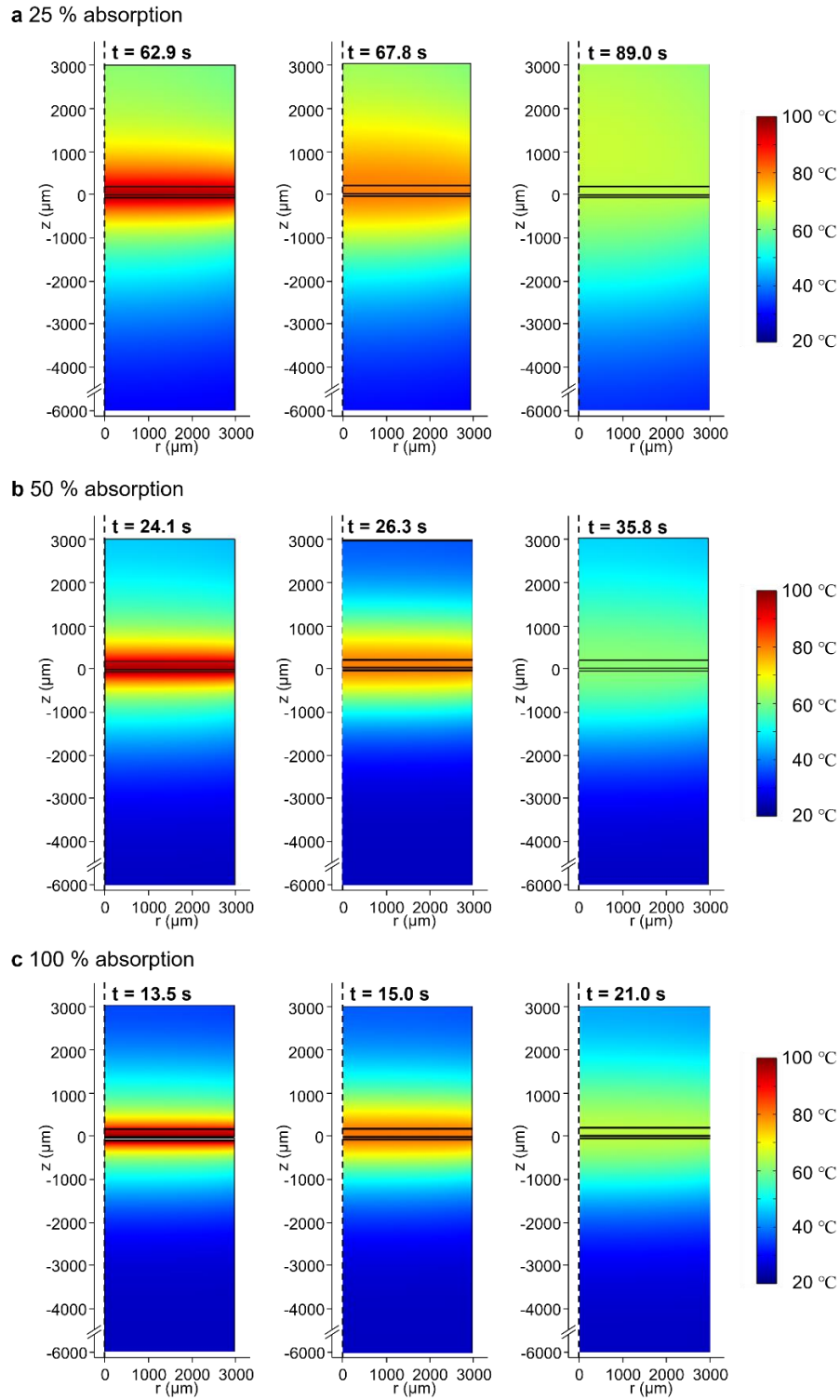
b 50 % absorption

c 100 % absorption

Figure 4.4 Temperature distribution of the photonic PCR in the third heating thermal cycle with different absorptions of Au – 25 % (a), 50% (b), and 100 % (c) when the center of the chamber (r = 0 μm, z = 100 μm) was 95 °C (first column), 80 °C (second column), and 65 °C (third column).

Figure 4.5 Temperature distribution of the photonic PCR in the third heating thermal cycle with different absorptions of Au – 25 % (a), 50% (b), and 100 % (c) when the center of the chamber (r = 0 μm, z = 100 μm) was 95 ℃ (first column), 80 ℃ (second column), and 65 ℃ (third column).

4.4   EVALUATION OF THERMAL EFFECTS OF BACK MATERIALS

For rapid thermal cycling, the photonic PCR device design needs to be optimized to minimize the time required for the heating and cooling step in thermal cycling. Firstly, we investigated the influence of back materials for optimization. Top material was taken as PMMA. Figure 4.6 shows the temperature profiles of photonic PCR device with different back materials for 1 minute. The time of air required for the 1st cycle was the shortest among the four different materials. However, as thermal cycles progress, the thermal cycle of oil got faster than those of other materials due to faster cooling ramping rate of oil. As shown in Figure 4.4a and b, the heating ramping rates of air, oil and polycarbonate (PC) were 20 °C /s, 15 °C /s and 12.5 °C /s, respectively. The cooling ramping rate of air, oil, and PC were 0.70 °C /s, 1.81 °C /s, and 1.80 °C /s, respectively. In this simulation, the denaturation and annealing /extension temperature was set as 95 and 65 °C, respectively. Figure 4.7 shows the time required for heating and
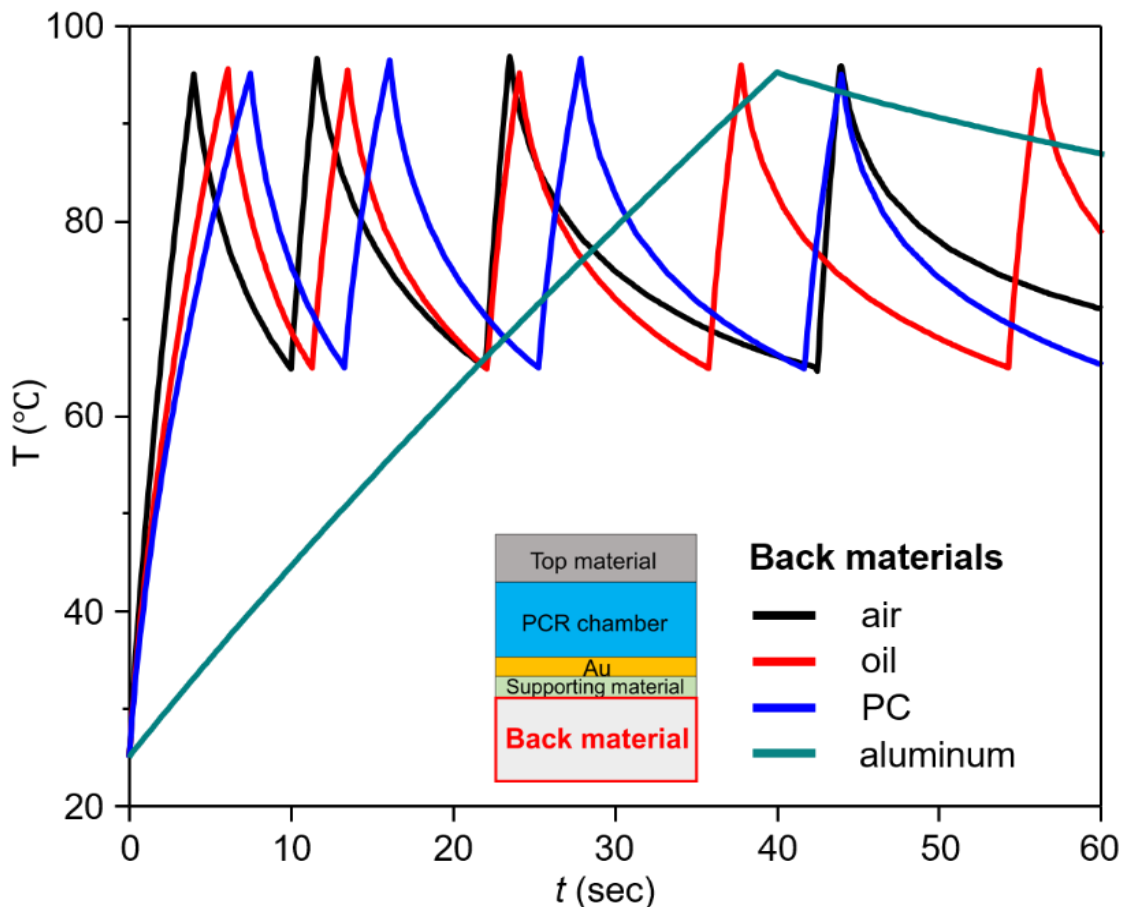

Figure 4.6 Calculated temperature profiles with different back materials of Au from 95 °C (denaturation) and 65 °C (annealing / extension) in 1 minute.
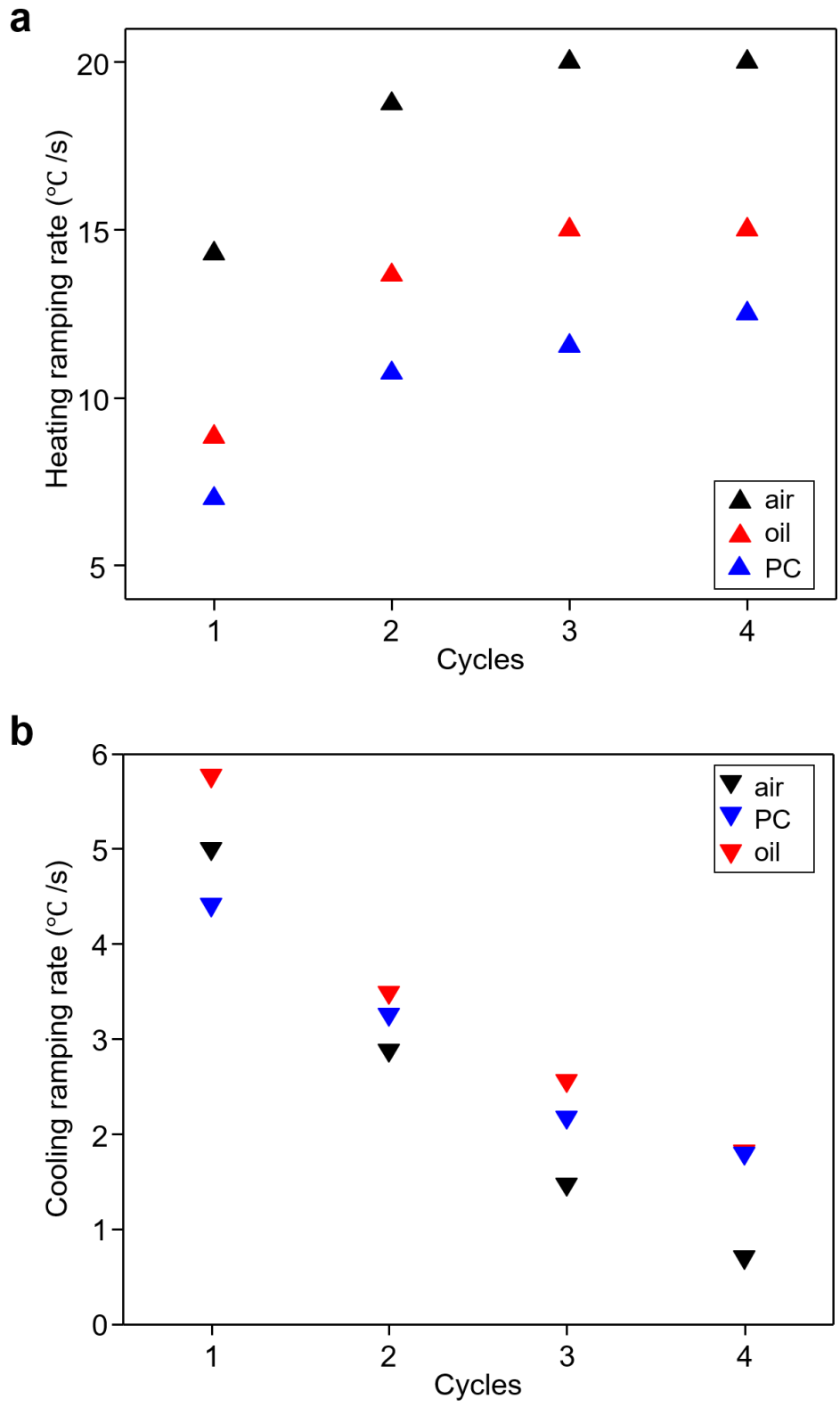
Figure 4.7 The heating ramping rate (a) and the cooling ramping rate (b) of the photonic PCR with different back materials.
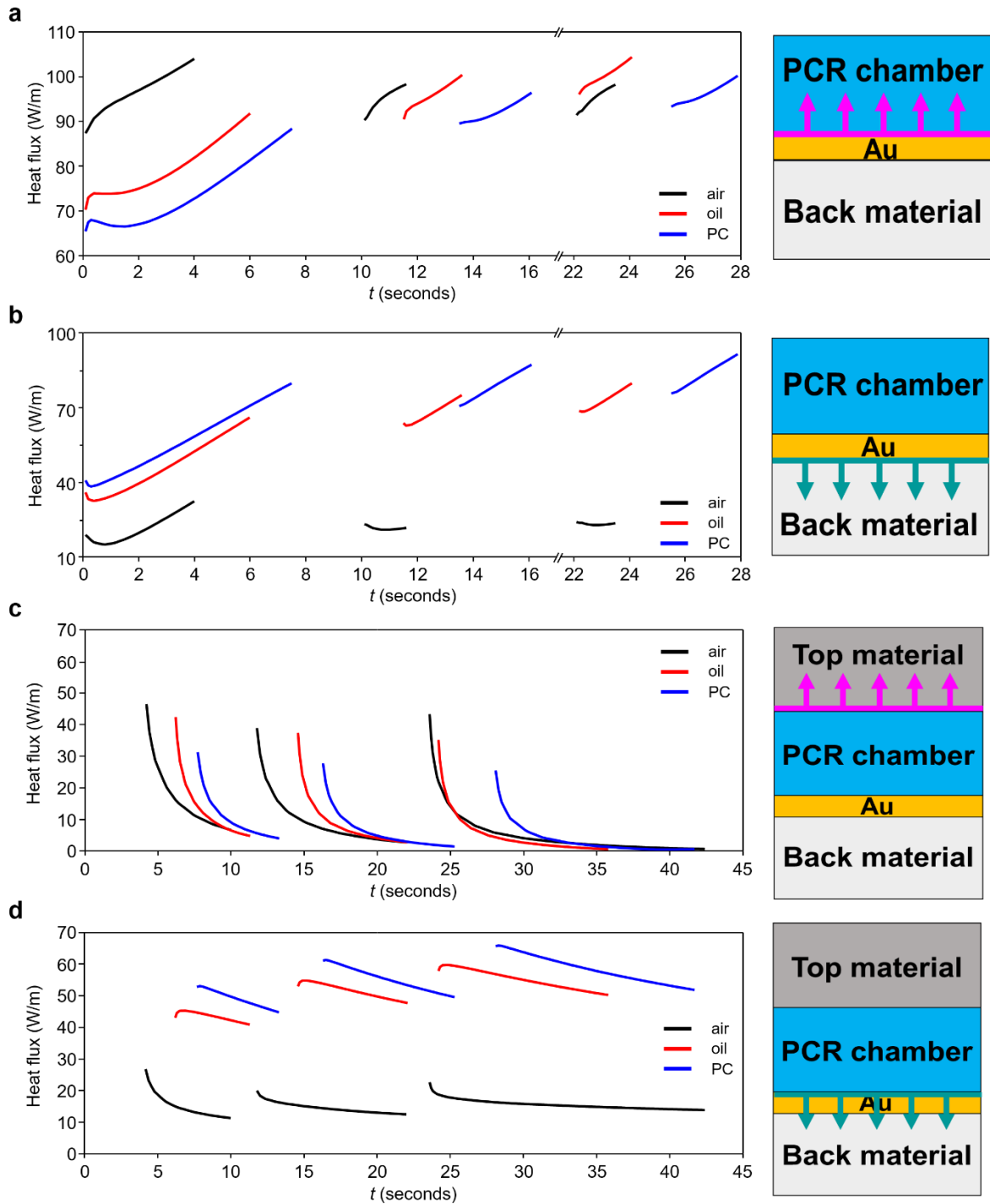
Figure 4.8 Heat flux of the first three cycles with different back materials. Heat flux from Au to PCR chamber (a) and back material (b) on heating thermal cycle. Heat flux from PCR chamber to top material (c) and back material (d) on cooling thermal cycle. The thermal properties of PCR chamber and top materials were taken as water and Poly(methyl methacrylate) (PMMA) in calculation, respectively.
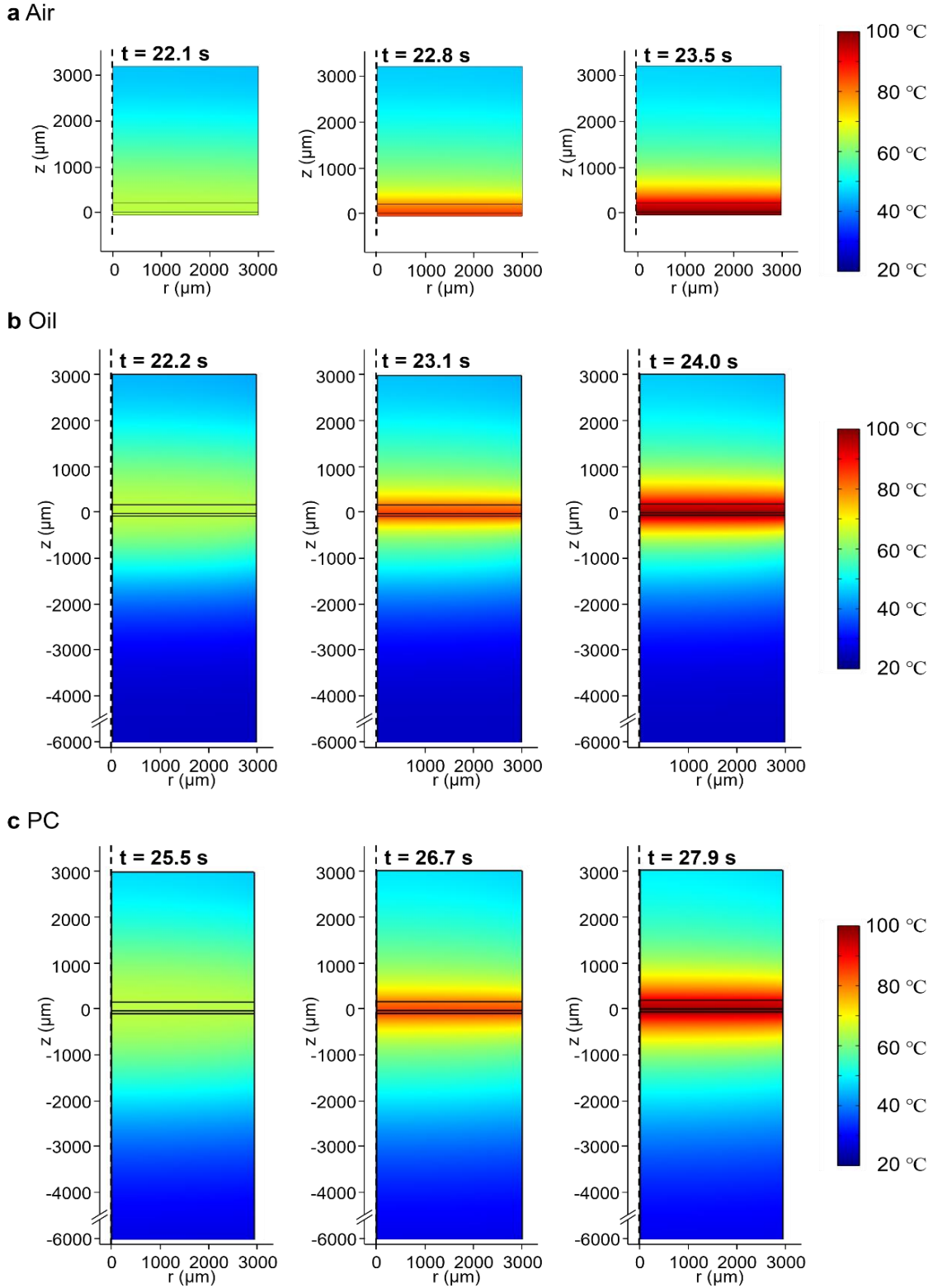
Figure 4.9 Temperature distribution of the photonic PCR in the third heating thermal cycle with back materials as air (a), oil (b), and PC (c) when the center of the chamber (r = 0 μm, z = 100 μm) was 95 °C (first column), 80 °C (second column), and 65 °C (third column).
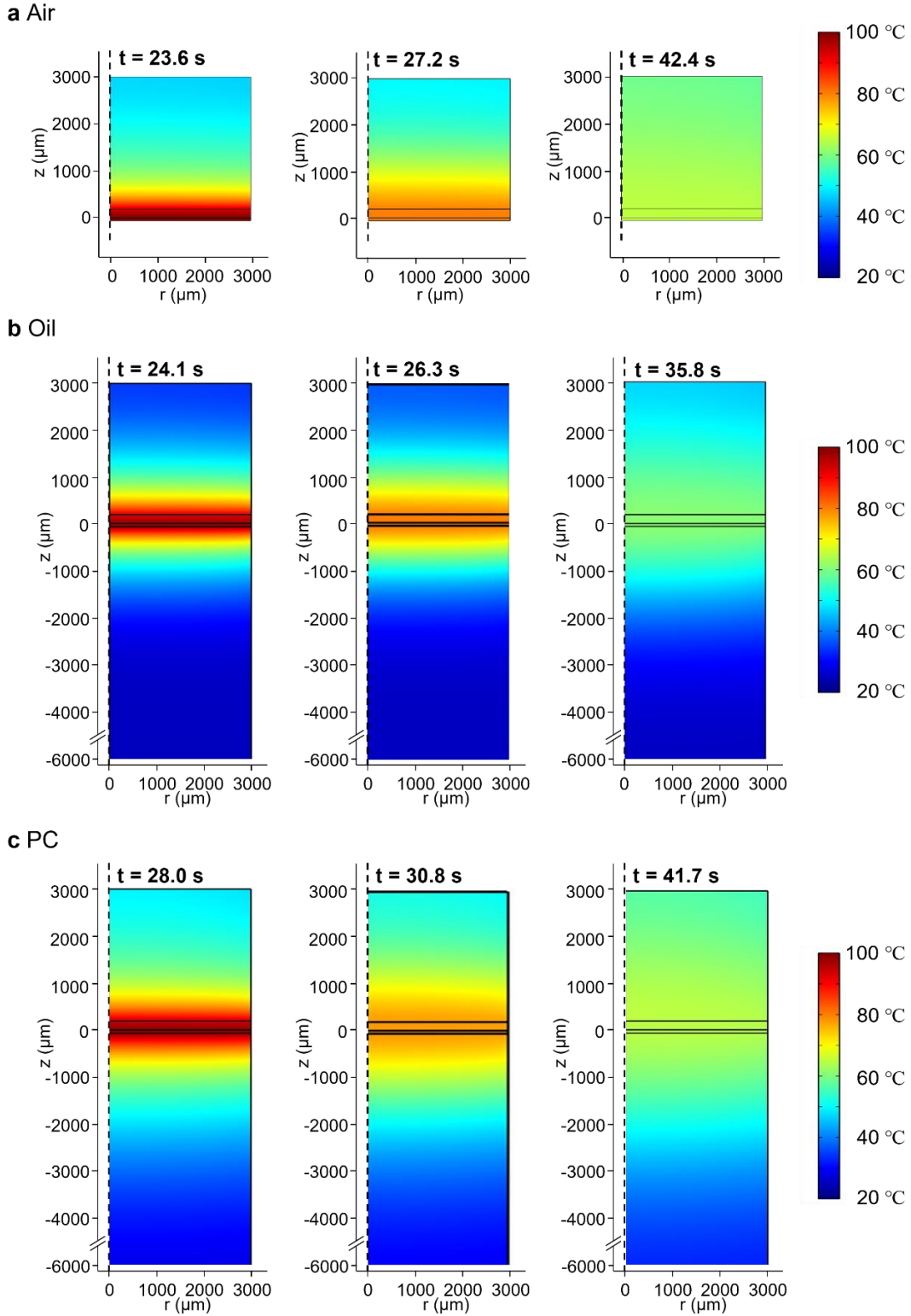
70

Figure 4.10 Temperature distribution of the photonic PCR in the third cooling thermal cycle with back materials as air (a), oil (b), and PC (c) when the center of the chamber (r = 0 μm, z = 100 μm) was 95 °C (first column), 80 °C (second column), and 65 °C (third column).

71

cooling of the first 4 cycles of photonic PCR device with back materials. At the first heating cycle, it took only 4 s (air), 6.1 s (oil) and 7.5 s (PC). The difference of heating cycle time of air and polycarbonate was 3.5 s. At the fourth heating cycle, the heat cycling time was 1.5 s (air), 2.0 s (oil) and 2.6 s (PC). The difference of heating cycling time between air and oil was only 0.5 s. However, at the fourth cooling cycle, the cooling times were 42.6 s (air), 16.5 s (oil) and 16.7 s (PC) and the difference of cooling cycle times between air and oil was 26.1 s. Also, the larger the number of thermal cycles, the larger the different cooling cycle time between air and oil. Therefore, the cooling cycles become more important that the heating cycles for optimizing the photonic PCR and the thermal conduction cooling of back materials such as oil or PC was more effective than the thermal convection (air). Figure 4.8a and b show the heat flux generated by Au layer with different back materials on heating cycles. When light comes to Au, Au absorbs light and converts light to heat. Heat generated by Au can be transmitted to either PCR chamber or back material. As shown in Fig. 4.8a, heat flux from Au to PCR chamber with air was highest among three materials. However, on the next two heating thermal cycles, heat energy transferred from Au to PCR chamber was almost the same among three materials, which is the reason why the heating ramping rates were almost the same. Figure 4.8b shows the heat flux from Au to back materials, which means the heat loss of the photonic PCR on heating thermal cycle. Heat loss of air was smallest among three materials. Figure 4.8c and d show the heat flux on cooling thermal cycles. As shown in Figure 4.8, top materials became ineffective for cooling. Thus, the heat flux from the PCR chamber to back materials was a major source of cooling (Fig. 4.8d). Figure 4.9 and 4.10 demonstrate the temperature distribution of the photonic PCR at the third thermal cycle. Because the govern equation is $\frac{\partial T}{\partial t} = \alpha_i \nabla^2 T$ and the heat flux is a function of $\frac{\partial T}{\partial t}$, the temporal temperature change, that is the thermal cycle, is related to the spatial temperature distribution. As shown in Fig 4.9 and 4.10, the average temperature of PC was higher than that of oil due to higher heat flux from Au to the back material. Also, the heat flux from PCR chamber to top materials was exponentially decreased (Fig 4.8) because the temperature around the PCR chamber became almost same over time.

4.5   EVALUATION OF THERMAL EFFECTS OF TOP MATERIALS

The effect of the top materials is presented in Fig. 4.12. On heating thermal cycle, the ramping rate of air is the fastest among three materials because of low heat loss at the top of the PCR chamber. In addition, the heating cycles between PC and oil were not a huge different due to similar temperature gradients in Fig 4.13. The thickness of top materials also affected the temperature gradient. Comparing to the temperature distribution of back materials, the temperature gradients of the top materials were gentle. The thickness of the top material was not so long that the top materials increased internal energy instead of dissipation toward air. Heat flux from the top materials to air On the other hand, the

cooling ramping rate of oil became shortest among three materials as the number of thermal cycle increased as shown in Fig 4.12b. However, comparing to Fig. 4.3c, the difference of cooling rates between air (convection) and other materials (conduction) was smaller because the temperature gradients were similar each other in Fig 4.14 ($Q \propto \nabla^2 T$).
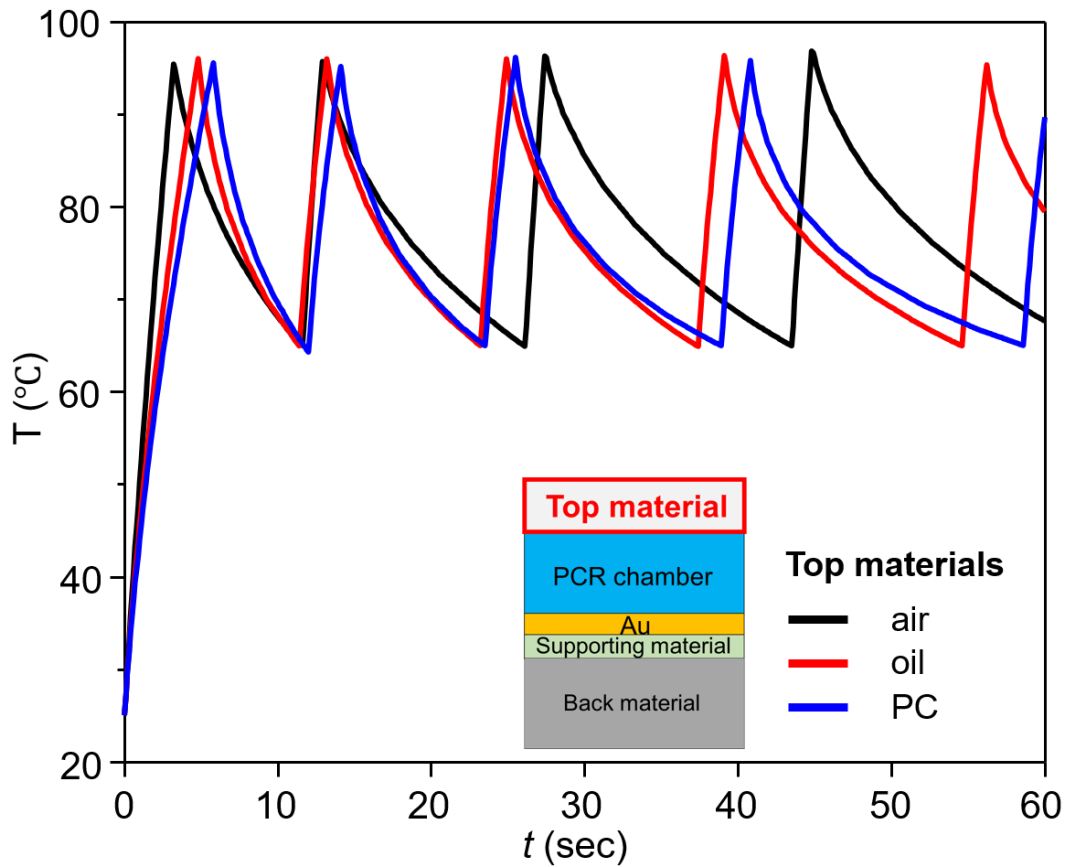

Figure 4.11 Calculated thermal cycling with different top materials from 95 ℃ (denaturation) and 65 ℃ (annealing / extension) in 1 minute.
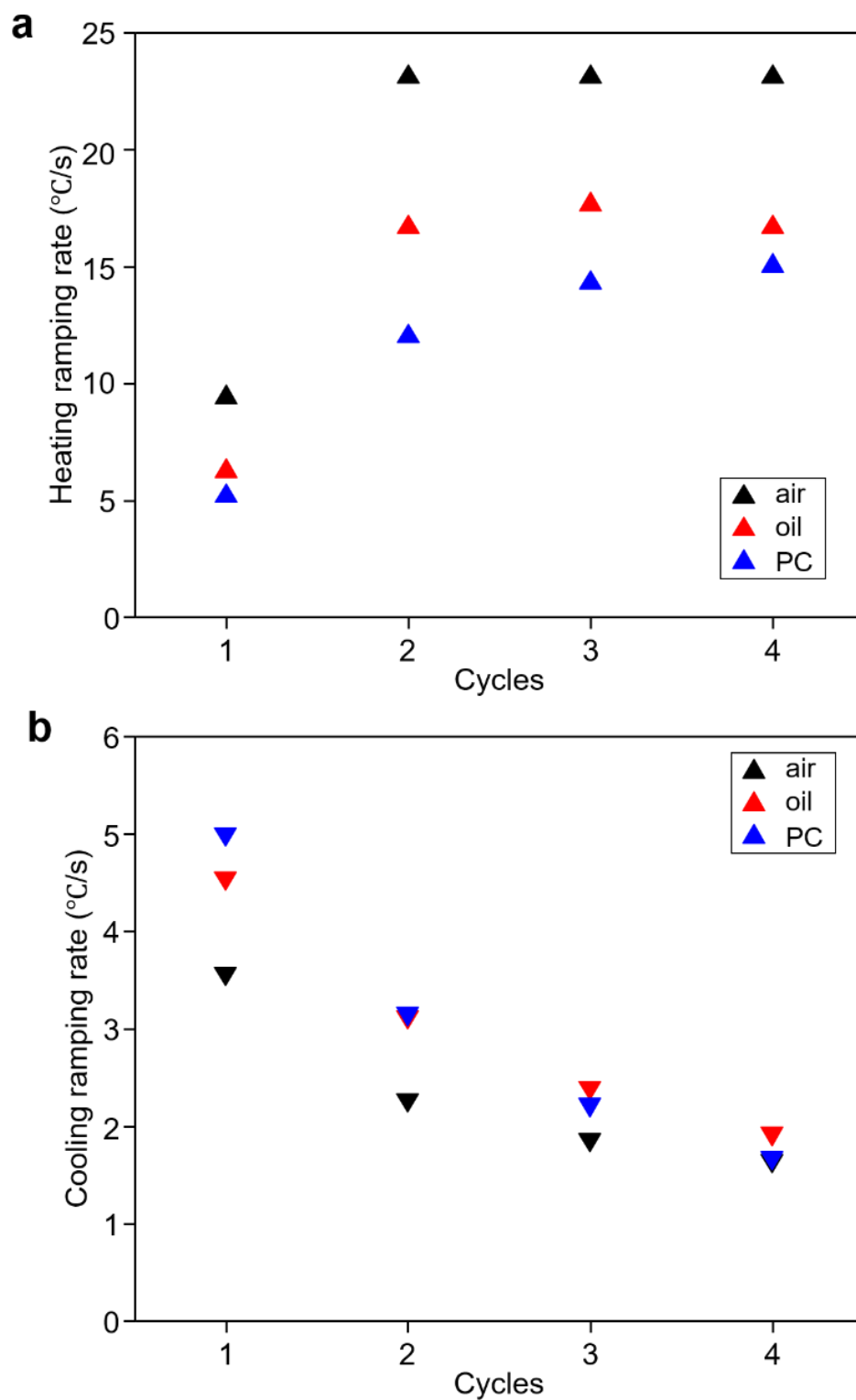
Figure 4.12 Calculated thermal cycling with different absorption of Au. (a) The thermal cycle of the photonic PCR from 95 ℃ (denaturation) and 65 ℃ (annealing / extension) in 1 minute. The heating ramping rate (b) and the cooling ramping rate (c) of the photonic PCR
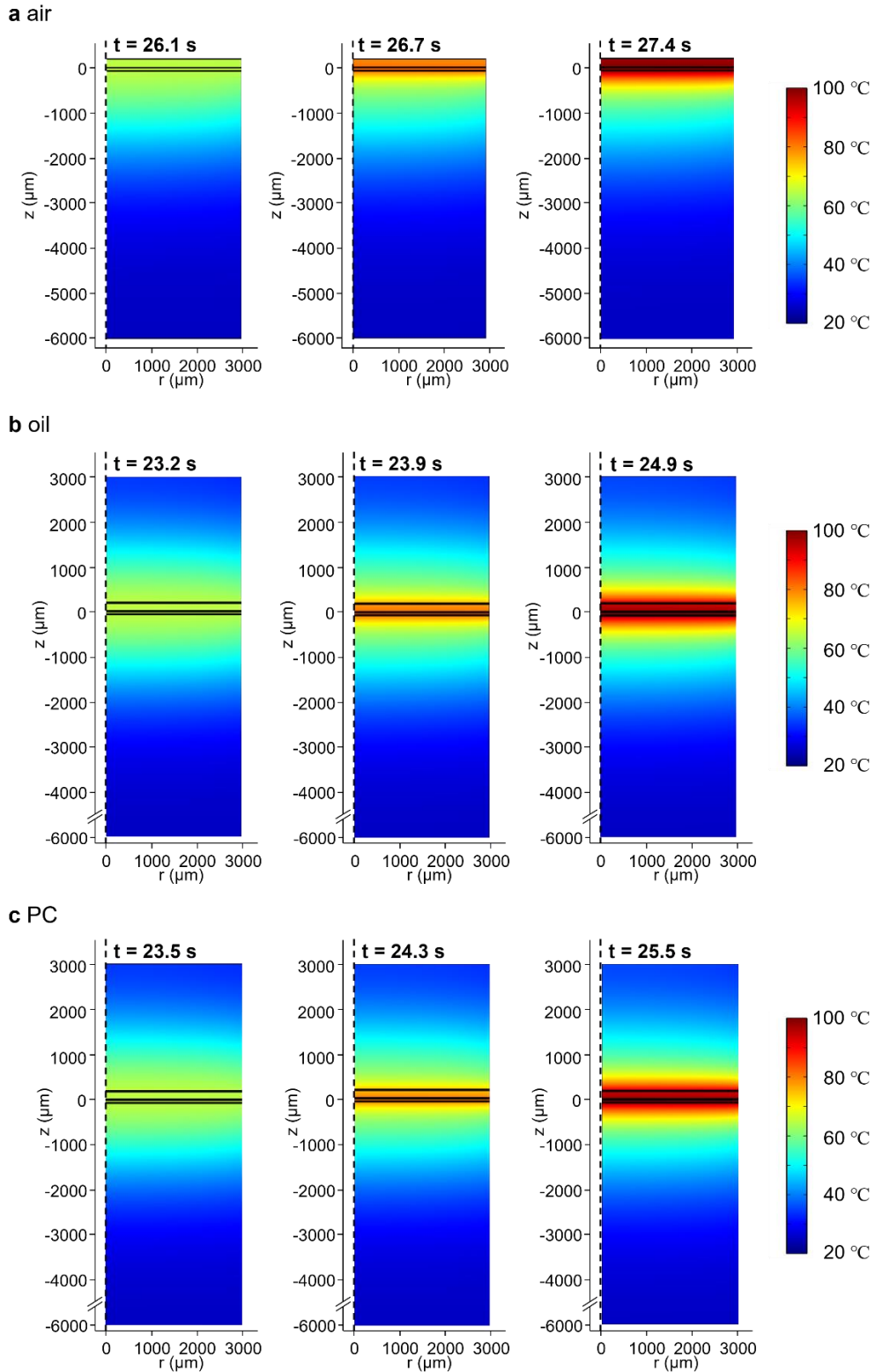
Figure 4.13 Temperature distribution of the photonic PCR in the third heating thermal cycle with different top materials, air (a), oil (b), and PC (c) when the center of the chamber (r = 0 μm, z = 100 μm) was 95 ℃ (first column), 80 ℃ (second column), and 65 ℃ (third column).
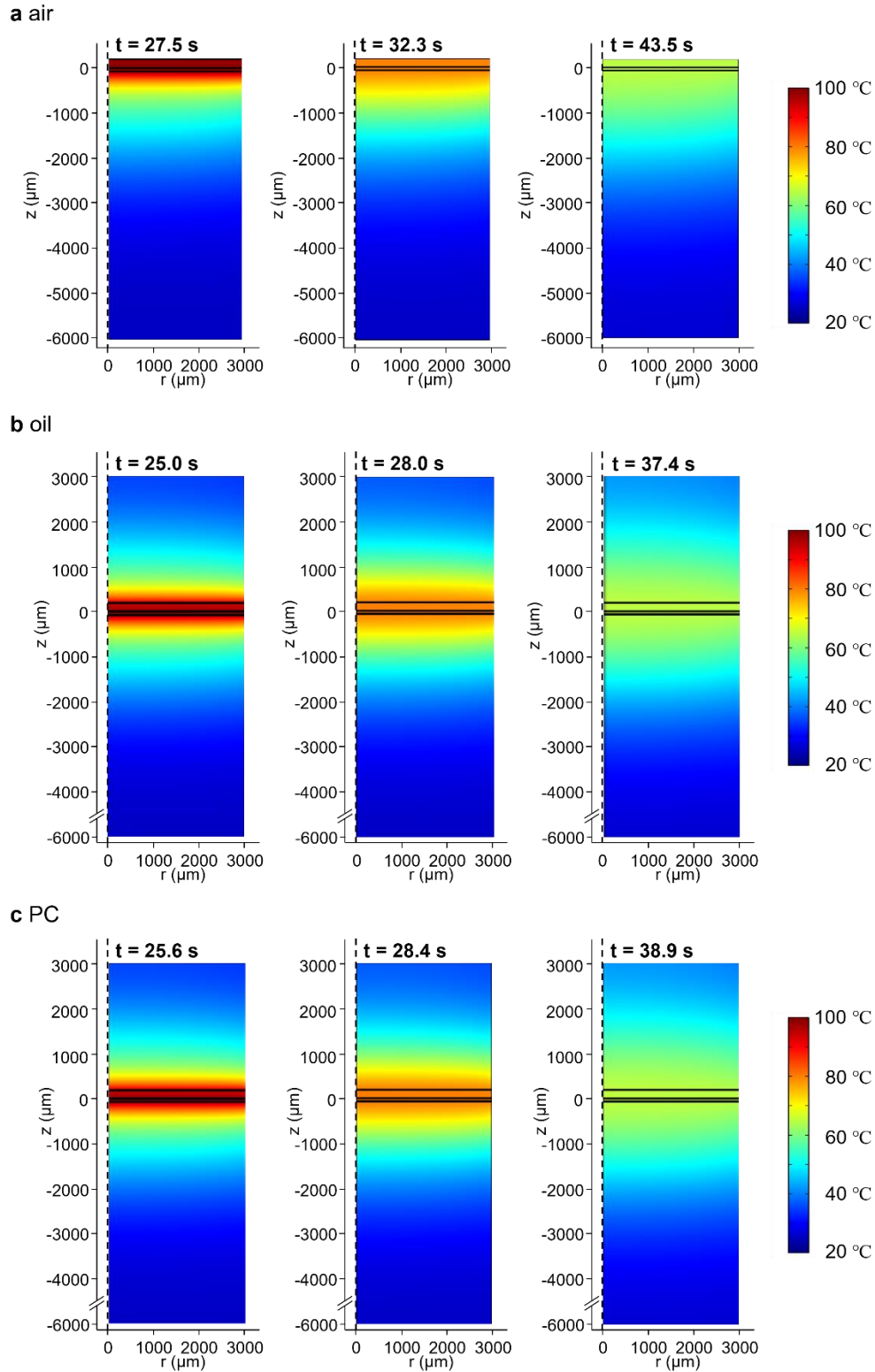
Figure 4.14 Temperature distribution of the photonic PCR in the third cooling thermal cycle with different top materials, air (a), oil (b), and PC (c) when the center of the chamber ($r = 0$ μm, $z = 100$ μm) was 95 ℃ (first column), 80 ℃ (second column), and 65 ℃ (third column).

4.6 CONCLUSION

We demonstrated a comprehensive, thermal computational model of the photonic PCR with aluminum anodized oxide (AAO) to improve the performance of the photonic PCR. The absorption of Au is one of critical factors to decrease total thermal cycling time. For the heating ramping rate, the higher absorption of Au generates more heat energy. Furthermore, the short heating time makes the steep temperature gradients in the system, which affects the cooling ramping rate. This is because the heat dissipation is related to the temperature gradient. Thermal diffusivity of materials also affects the thermal cycles. The lower thermal diffusivity, the higher temperature gradient as shown in Fig. 4.5 or Fig. 4.10. This comprehensive simulation results will pave a way to design the photonic PCR device.

4.7 REFERENCES

1. Erlich, H. A., Gelfand, D. & Sninsky, J. J. Recent advances in the polymerase chain reaction. Science (80-.). 252, 1643–1651 (1991).
2. Maltezos, G. et al. Exploring the limits of ultrafast polymerase chain reaction using liquid for thermal heat exchange: A proof of principle. Appl. Phys. Lett. 97, (2010).
3. Wheeler, E. K. et al. Under-three minute PCR: Probing the limits of fast amplification. Analyst 136, 3707 (2011).
4. Terazono, H., Takei, H., Hattori, A. & Yasuda, K. Development of a high-speed real-time polymerase chain reaction system using a circulating water-based rapid heat-exchange. Jpn. J. Appl. Phys. 49, (2010).
5. Wittwer, C. T., Fillmore, G. C. & Garling, D. J. Minimizing the time required for DNA amplification by efficient heat transfer to small samples. Anal. Biochem. 186, 328–31 (1990).
6. Farrar, J. S. & Wittwer, C. T. Extreme PCR: Efficient and specific DNA amplification in 15-60 seconds. Clin. Chem. 61, 145–153 (2015).
7. Yoon, D. S. et al. Precise temperature control and rapid thermal cycling in a micromachined DNA polymerase chain reaction chip. J. Micromechanics Microengineering 12, 813–823 (2002).
8. Fuchiwaki, Y., Nagai, H., Saito, M. & Tamiya, E. Ultra-rapid flow-through polymerase chain reaction microfluidics using vapor pressure. Biosens. Bioelectron. 27, 88–94 (2011).
9. Roper, M. G., Easley, C. J. & Landers, J. P. Advances in polymerase chain reaction on microfluidic chips. Analytical Chemistry 77, 3887–3893 (2005).
10. Sackmann, E. K., Fulton, A. L. & Beebe, D. J. The present and future role of microfluidics in biomedical research. Nature 507, 181–189 (2014).
11. Lee, D.-S. et al. Bulk-micromachined submicroliter-volume PCR chip with very rapid thermal response and low power consumption. Lab Chip 4, 401–407 (2004).

12. Cao, Q., Kim, M. C. & Klapperich, C. Plastic microfluidic chip for continuous-flow polymerase chain reaction: Simulations and experiments. Biotechnol. J. 6, 177–184 (2011).
13. Sadler, D. J., Changrani, R., Roberts, P., Chou, C. F. & Zenhausern, F. Thermal management of bioMEMS: Temperature control for ceramic-based PCR and DNA detection devices. IEEE Trans. Components Packag. Technol. 26, 309–316 (2003).
14. Erickson, D., Sinton, D. & Li, D. Joule heating and heat transfer in poly(dimethylsiloxane) microfluidic systems. Lab Chip 3, 141 (2003).
15. Kossoy, A. et al. Optical and Structural Properties of Ultra-thin Gold Films. Adv. Opt. Mater. 3, 71–77 (2015).
16. Bae, K. et al. Flexible thin-film black gold membranes with ultrabroadband plasmonic nanofocusing for efficient solar vapour generation. Nat. Commun. 6, 10103 (2015).

CHAPTER 5

INTEGRATED MOLECULAR DIAGNOSTIC SYSTEM

5.1 ABSTRACT

Rapid, precise identification of pathogens in urine samples is important for the clinical management of community-acquired urinary tract infections (UTIs) or sexually transmitted diseases (STDs). However, a conventional culture-based diagnostic method is time-consuming, pushing physicians to use antibiotics without adequate clinical data. Here, we present a rapid and simplified molecular diagnostic system to identify pathogens in 15 minutes. Our integrated molecular diagnostic system includes bacterial enrichment, cell lysing step, and PCR in a single platform. We achieve a 40,000-fold bacterial enrichment on the Au-coated porous membrane from 1 ml sample in 2 minutes without any external force. We accomplish a photothermal lysis of concentrated bacteria within 1 minute using ultrafast light-to-heat conversion of nanoplasmonic optical antenna. Finally, we demonstrate the end-point detection of up to 10^3 CFU ml^{-1} of *Escherichia Coli* in 10 minutes. This integrated molecular diagnostic system will provide rapid pathogenic detection in both developing and developed countries.

5.2 INTRODUCTION

Infectious diseases are one of the leading causes of death worldwide[1]. Despite advances in medical technology, infectious diseases continue to contribute significantly to the global disease burden. Growing drug and antibiotic resistance is compounding the problem, which has become a major public health concern[2]. Among infectious diseases, community-acquired urinary tract infections (UTIs) are one of the most common types of infections[3,4]. According to a 2006 survey, the U.S. alone accounted for 1.7 million emergency room visits, 11 million physician visits, and half a million hospitalizations due to UTIs, causing 3.5 billion dollars of health care costs[5]. Furthermore, one-third of women suffered UTI before the age of 24 and an estimated half of the female population will experience UTIs during their life[6]. Clinical management of community-acquired UTIs, therefore, requires a diagnostic test that can be performed rapidly and simply in an outpatient setting.

79

Currently, the standard method for identifying most bacterial pathogens is a culture-based method, which has a long turn-around time because it requires overnight culturing and bacterial isolation[7,8] (Fig. 5.1a). Therefore, in patients suspected to have community-acquired bacterial infections such as UTI or STI, clinicians are forced to make initial treatment decisions empirically[9]. Antibiotics are prescribed before any pathogen is identified, which results in the overuse of antibiotics followed by an increase in antibiotic-resistant pathogens.

Fast and precise diagnoses from clinical samples provide clinicians with the information to make rapid and appropriate medical decisions and also to prevent the overuse of antibiotics and the selection of drug resistance. From this point of view, Point-of-Care (POC) tests have shown significant potential in both the developing and developed countries. The easy-to-use, rapid, and precise POC devices provide the necessary diagnostic tools in low-resource settings where general laboratory infrastructures are unavailable[10] as well as in developed country settings where personalized healthcare can be established to reduce costs (i.e. at-home diagnostics)[11]. In addition, POC tests can reduce unnecessary burden on hospital laboratories [12].

Many novel approaches have emerged for the rapid detection of bacteria recently. Using time-resolved luminescence signal, *Escherichia coli (E. coli)*-specific bacteriophages can detect *E. coli* with concentrations as low as $10^3 – 10^4$ cells/ml within 25 minutes[13]. Matrix-assisted laser desorption ionization-time of flight mass spectrometry (MALDI-TOF MS) has been suggested to identify pathogens[14]. This method demonstrated 94.6% success rate in a high bacterial concentration. Raman spectrometry can also be employed in a centrifugal microfluidic platform[15]. They handle large volumes of sample (5-10 mL) and require short detection time (1.5 min) to achieve reliable detection. However, these methods require complicated sample preparation and necessitate the use of bulky instruments, like centrifuges, or microscopes, which are not ideal for a POC setting. Lateral flow assay is a good test for POC but this method also requires centrifuging to achieve reproducible results[16]. Thus, an effective, rapid, and precise POC system for diagnosing UTI is yet to be developed.

Recently, polymerase chain reaction (PCR) have shown great potential to quickly identify bacterial pathogens with high sensitivity and specificity[17]. In particular, PCR facilitates a decreased turn-around time and may also enable clinicians to make the appropriate treatment decision. However, PCR requires labor-intensive complicated protocols as well as well-trained personnel to run the test. PCR combining microfluidic technologies have opened up possibilities of molecular diagnostics available for POC testing (POCT) and towards improving the speed and performance of microfluidic-based
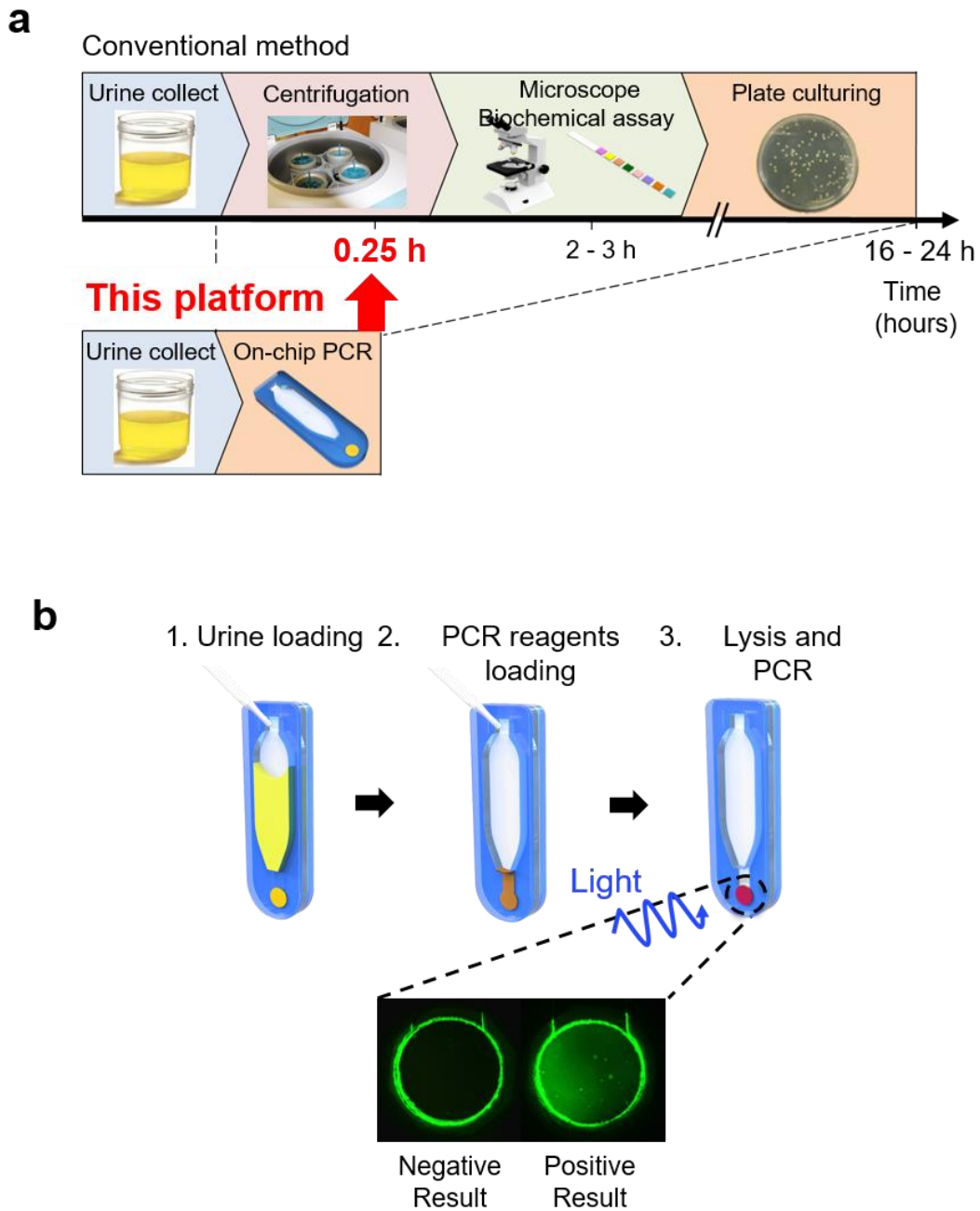
Figure 5.1 Integrated molecular diagnostic platform for rapid bacterial detection. (a) Comparison of a conventional culture-based method and the integrated molecular diagnostic platform (iMDx) for bacterial detection. (b) Workflow of iMDx. 1 ml of patient's urine is loaded into the diagnostic platform followed by loading of PCR reagents and SYBR green. After on-chip PCR amplification, resulting fluorescence of the sample is measured.
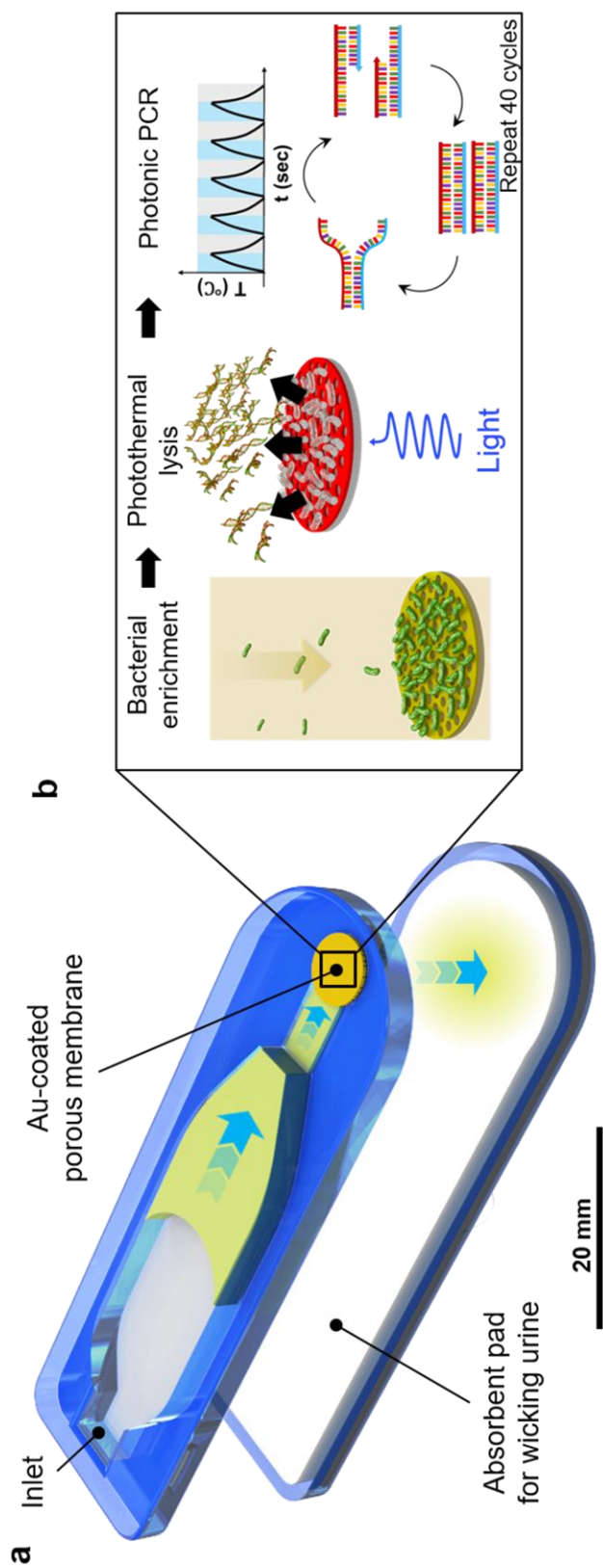
Figure 5.2 Schematics of integrated molecular diagnostic platform. (a) This platform consists of detection and absorbing compartments. Gravity and capillary force of the absorbent pad enable a urine sample to flows in the detection chamber of the platform without any external equipment. The absorbent pad assists a sample to flow and facilitates the pre-concentration of the pathogen by absorbing the water content in the urine. (b) Au-coated membrane of the detection chamber has three roles: 1) Bacteria are enriched on the porous membrane because the size of the pore is smaller than that of bacteria. 2) Au on the porous membrane absorbs the light and converts it into heat energy. As a result, pathogens are thermally lysed. 3) Then, PCR is performed by turning a light on and off repeatedly to achieve thermal cycling.

82

PCR methods[18–22]. However, several important issues still need to be addressed. First, highly efficient and high-throughput sample preparation methods need to be integrated on-chip. For example, the concentration of bacteria in the early stages of a UTI is usually lower than 10^4 CFU/ml. Some current devices depend on other sample preparation equipment or reagents such as a centrifuge or a chemical lysis kit. In addition, microfluidic devices generally handle less than 10 µl of samples or isolated pathogen suspensions, which means that the bacterial preconcentration step is necessary. Therefore, the integration of on-chip, simple, effective and high-throughput sample preparation methods is a key component of a device-based system. Second, most devices require bulky instruments such as lasers, syringe pumps, and AC signal generators. This bulky equipment increases the complexity and cost, which is not ideal for POC settings.

Here, we present an integrated molecular diagnostic system to identify pathogens in 15 minutes (Fig. 5.1 and 5.2). For a sample preparation, we physically capture bacteria on a porous membrane from the sample (1 ml) within 2 minutes using capillary force of an absorbent pad behind the membrane and gravitational force of the sample itself. The photothermal effect of the Au-coated porous membrane enables the thermal lysis of cells as well as a photonic PCR-based nucleic acid amplification to identify *E. coli*. We expect that this molecular diagnostic system will provide a solution for the rapid diagnosis of pathogen infection and contribute to POC diagnostics in both developing and developed countries.

5.3   METHODS

Materials and Reagents

All chemicals purchased from commercial sources were used as received unless otherwise indicated. Phosphate buffered saline (PBS) 10× solution was purchased from Corning (Manassas, VA). LB broth was purchased from EMD Millipore (Billerica, MA). Agar, bovine serum albumin (BSA), and nuclease-free water were purchased from Fisher Scientific (Pittsburgh, PA). All primers were ordered from Integrated DNA Technologies (Coralvilla, IA). PrimeSTAR GXL DNA Polymerase (1.25 U/µl), 5X PrimeSTAR GXL Buffer (5mM Mg^{2+} at 5X) and dNTP mixture (2.5mM each) were purchased from Takara Bio USA, Inc (Mountain view, CA). SsoFast™ EvaGreen® Supermix (2X) was purchased from BIO-RAD Laboratories (Hercules, CA). Simulated urine consisted of 8.2 g of NaCl, 0.64 g of $CaCl_2$, 1.14 g of $MgSO_4$, 20 g of urea, and 33 ounces of distilled water[23].

Design and fabrication of photonic PCR membrane

The device, with dimensions 18 mm × 62 mm × 6.5 mm, was designed as a disposable platform (Fig. 1b, 1c and Schematic 1). The polycarbonate sheets for the top and bottom layers of the device and the polymethylmethacrylate (PMMA) sheets for the middle layer of the device were cut using a laser cutting system (VersaLASER VL-200,

Schematic 1. Exploded view of the device.

Legend:
- Absorbent pad
- Double-sided tape
- Porous membrane
- Polycarbonate
- PMMA

Universal Laser System, Inc., Scottsdale, AZ, USA). The chip was cleaned with 30% ethanol, washed with deionized water, and dried with nitrogen gas. The top, middle, and bottom layers were bonded with 80-µm-thick double-sided tape (ARcare® 90445, Adhesives Research, Inc., Glen Rock, PA, USA). Polycarbonate porous membranes (Cyclopore 1 µm pore size, GE Healthcare Bio-Sciences, PA, USA) were loaded in an electron beam evaporator to deposit Au. Polycarbonate membrane were deposited with 5 nm of titanium, followed by an 80-nm deposition of Au under a base pressure of 8 x 10^{-7} Torr. Then, 6-mm circular pieces of Au-coated membrane were prepared with a punch (Biopsy Punch 6.0, Health link, FL, USA). One circular piece of Au-coated membrane was bonded to the device with 80-µm-thick double-sided tape.

LED-based miniaturized thermal cycler development

Two LEDs (Luxeon Rebel, Lumileds, CA, USA, royal blue with a peak wavelength of 447.5 nm, maximum optical power of 890 mW) were used, one for the measurement of the temperature and the other for PCR detection of *E. coli* plasmonic photothermal heating of the thin Au film. Power for LEDs was supplied from a constant current LED driver (2008B PowerPuck 1000 mA, LuxDrive, VT, USA). To focus the light from the LEDs, a Carclo 20 mm fiber coupling optic (part number: 10356, CarcloOptics, PA, USA) was employed. The temperature of the solution was monitored and recorded in real time by a type-K insulated theromocouple purchased from OMEGA Engineering (part number, 5SC-TT-K-40-36) for thermal cycling. Temperature cycling using an LED, source meter, and thermocouple was controlled through an Arduino.

Bacteria growth

The original *Escherichia coli* (*E. coli*) K12 W3110 strain was kindly provided by Professor Lee Riley from the University of California, Berkeley. GFP-expressing recombinant *E. coli* was also used for the imaging of bacteria captured on the porous membrane of devices. *E. coli* suspended in DI water was used for evaluating the capture efficiency. *E. coli* was grown in Luria–Bertani (LB) broth and plated on LB agar plates during the log phase growth. Microbial cells were prepared by inoculating 5 mL of LB with a single colony and allowing it to grow overnight at 37 °C. The cells were centrifuged at 8000 rpm for 5 min and suspended in DI water.

Preparation of PCR reagents, DNA for PCR amplification

The primers for PCR were designed to produce short amplicons ranging from 100 to 200 bp that would be suitable for rapid PCR. The forward (GCCTAACACATGCAAGTCGAA) and reverse (CAGGCAGTTTCCCAGACATTAC) primers were purchased from Integrated DNA technologies. The PCR reagents for this system comprised of 2 µl of PrimeSTAR GXL DNA Polymerase (1.25 U/µl), 4 µl of 5X PrimeSTAR GXL Buffer (5mM Mg^{2+} at 5X), 2 µl of dNTP mixture, 1 µl each of forward

and reverse primers (final concentration: 500 nM), 2 µl of BSA (final concentration: 3 mg/ml), 4 µl of glycerol (final concentration: 10%), and 4 µl of PCR grade water. BSA was used to prevent the adsorption of *Taq* polymerase and the reagents. A CFX96 real-time thermocycler (Bio-rad, Hercules, CA, USA) was used as the reference. The crude extract as a template from bacteria was used for species identification. DNA was extracted with the QIAamp DNA blood mini kit (Qiagen). The assay was performed according to the manufacturer's instructions. DNA was quantified using a Nanodrop 2000 (ThermoScitific, USA). Thermal cycle conditions consisted of denaturation at 95°C and annealing and extension at 62°C with a two-step amplification procedure for 40 cycles.

5.4 DESIGN OF INTEGRATED MOLECULAR DIAGNOSTIC PLATFORM

We report a rapid molecular diagnostic system that can capture and detect Gram-negative bacteria (GNB) from a large volume of urine sample including sample enrichment, photothermal lysis, and photonic PCR in a single platform. First, we designed, fabricated, and characterized the integrated platform to preconcentrate GNBs from an urine sample (1 ml) as shown in Fig. 5.1 and 5.2. Our molecular diagnostic system is mainly made by PMMA and double-sided tapes for manufacturing (Schematic 1). The chip consists of PMMA top and bottom layers, a dead-end PCR reaction chamber, an Au-coated polycarbonate membrane with 1-µm diameter of pores, and a sliding bar attached with an absorbent pad. Our platform consists of sample preparation chamber, Au-coated membrane for *on-site* photothermal lysis, *on-chip* PCR chamber, and absorbent pad. In Fig. 5.2a, a urine sample containing GNBs is loaded in the sample inlet, from which it moves to on-site detection chamber, which includes the track-etched polycarbonate membrane filter to physically capture GNBs. Behind the membrane filters, we connected an absorbent pad as a capillary force generator and waste reservoir. The capillary force of the absorbent pad and gravitational force of a sample by vertical sample chamber allow the sample to flow into the device by itself. Finally, GNBs could concentrated on the surface of porous membrane filter because the size of bacteria is smaller than that of the pore size. The high-density of pores in the polycarbonate membrane prevent the sample from flowing toward the lower layer of the device because of the high fluidic resistance. However, an absorbent pad provides sufficient capillary force to enable the fluid to flow. After manually removing the absorbent pad, it is difficult to reinstate flow on the surface of membrane. Therefore, we are able to attain concentrated bacterial isolates from a large volume of urine sample and our device does not require any external equipment (i.e. centrifugation, syringe pump) for sample enrichment, suitable for POCT applications.

5.5   PRECONCENTRATION OF PATHOGENS

To physically capture and concentrate *E. coli*, we embedded a porous membrane into the device (Fig. 5.3). Before *on-site* bacterial capturing, we investigated the flow rate-related parameters such as a pore-size and no. of stacked absorbent pads for efficient bacterial capturing. First, to validate the feasibility to facilitate the outflow of sample solution using an absorbent pad, a computational simulation was carried out using COMSOL Multiphysics. As illustrated in Fig. 5.4a, the forces that contribute to this system, such as the gravitational force (F_G), and surface tension (F_T) between the sample solution and the device wall were considered. The numerical simulations show that the sample solution with the absorbent pad can completely flow out within approximately 1 *min*, while
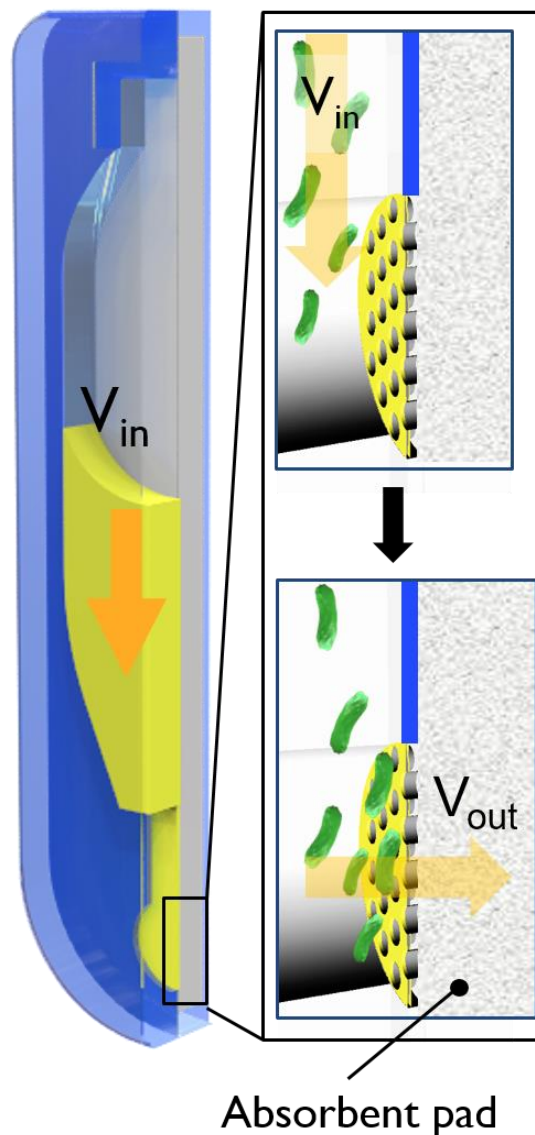

Figure 5.3 Schematic illustration of pathogen concentration on the membrane.

a lot of solution still remained in the chamber without the absorbent pad in the same time (Fig. 5.4b). Fig. 5.4c and 5.4d show the quantitative result about the time that the sample solution is completely flowed out. As shown in Fig. 5.4c and 5.4d, the chamber without the absorbent pad spent the approximately 10 *min* to completely flow out the sample solution. On the other hand, the time of complete spill of solution was considerably reduced in 1 *min* when the chamber had the absorbent pads that can provide the outflow of over 15 µl/s. Then, we experimentally investigated flow rate through the membranes in the devices with and without absorbent pad (Fig. 5.5a). As shown in Fig. 5.4c and 5.5a, good agreement between experimental and simulated results was obtained. It took 190, 110, and 90 seconds on average for a 1 ml bacterial suspension to pass through the 0.4, 1.0 and 2.0 µm pore membranes, respectively (Fig. 5.5a, inset). Then, we examined the relationship between the number of pads and the flow rate. We attached the stacked absorbent pad (n = 1, 2, 3)
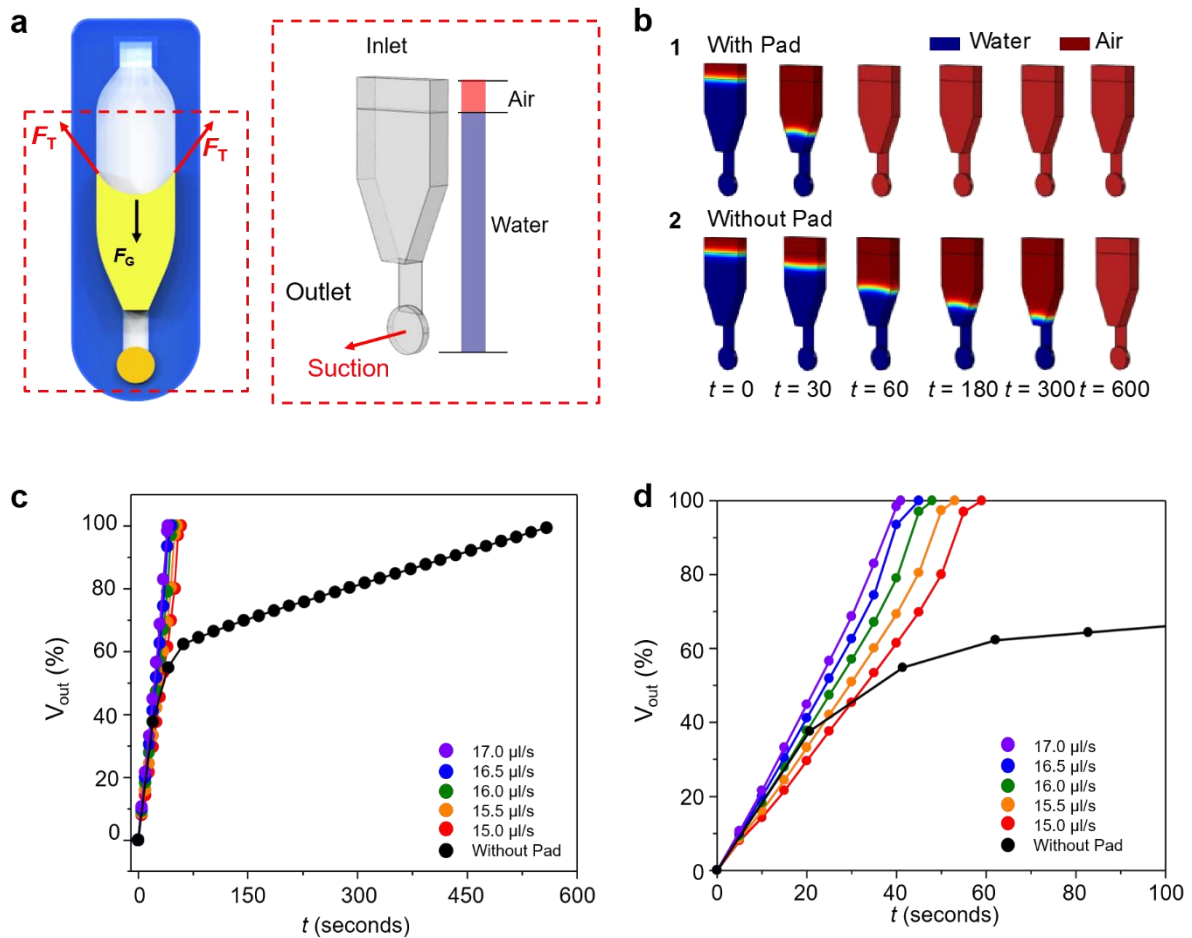

Figure 5.4 Fluid dynamic simulation of outflow though absorbent pad. (a) Three-dimensional geometry of pathogen concentration chamber with the forces acting on the system depicted: gravitational force (F_G) and surface tensions (F_{ST}) between the sample solution and the device wall. (b) Fluid dynamic simulation results of sample solution without and with absorbent pad. (c) and (d) Rates of outflow of sample solution with different absorption rates.
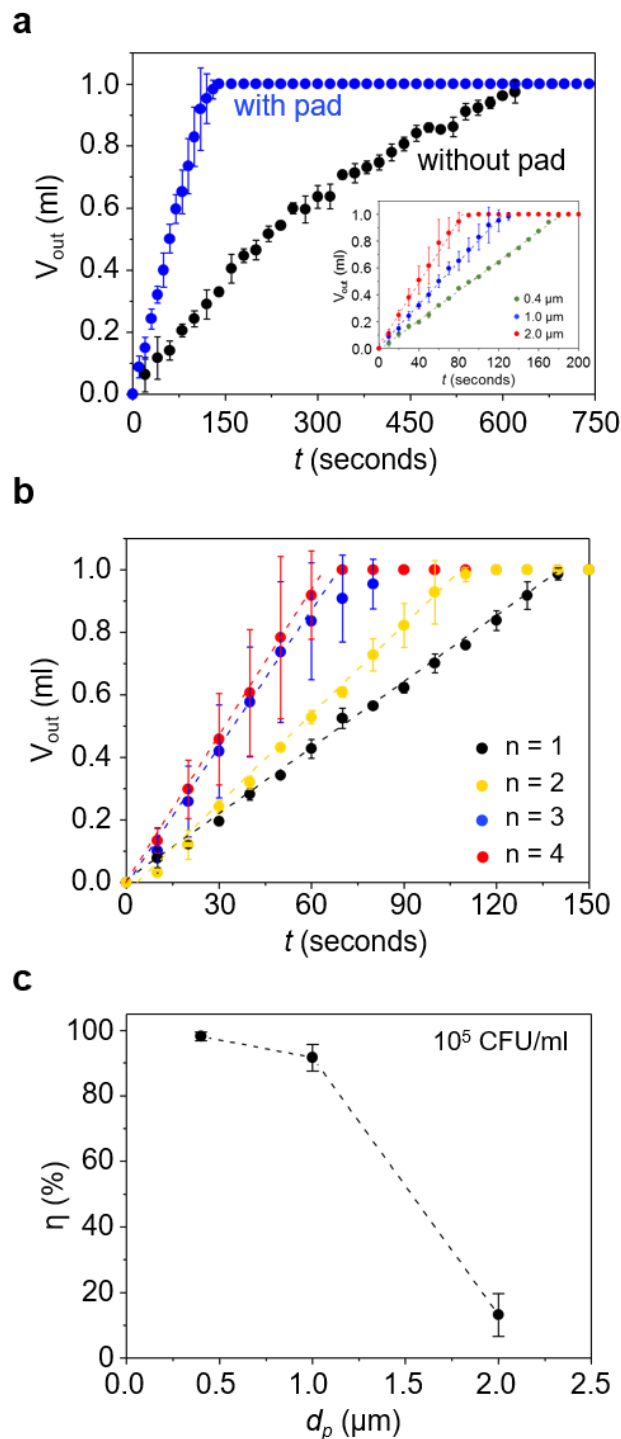
Figure 5.5 Characterization of flow rate and capture efficiency. (a) The volume of sample passing through the membrane inside the chamber over time (rate of sample flow) with and without pad. Inset: The volume of sample passing through the membrane inside the chamber over time different pore sizes of porous membrane with pad. (b) The volume of sample passing through the membrane inside the chamber over time with different numbers of pads stacked. (c) The capture efficiency of E. coli with different pore sizes.

behind the porous membrane (pore size: 1 μm). Then, a 1-ml of sample was introduced through the sample inlet. In Fig. 5.5b, flow rate increased linearly as the number of pads increased. However, the flow rate (14.6 μl/sec for n =3 and 15.6 μl/sec for n =4) is not significantly different between n = 3 and n = 4. For a 1-ml sample, three pads in series were optimal for this platform.

To ensure the rapid and efficient capture of *E. coli*, we tested the porous membranes with different pore sizes on the devices under the optimized pre-concentration conditions. A 1 ml of 10^5 CFU/ml *E. coli* suspension was passed through the devices to quantify the number of bacteria captured on the membrane of the devices. Then, the bacteria were collected and quantified at the inlet and outlet of the device using the plate count method. The capture was quantified per area of the chip using the following equation,

$$\text{Catpure efficiency } (\eta) = \frac{Total\ number\ of\ injected\ cells - The\ number\ of\ cells\ that\ passed\ through\ devices}{Total\ number\ of\ injected\ cells} \quad (1)$$

In Fig. 5.5c, 2.0-μm-pore membranes successfully captured only 17.5% of total bacteria. Most of the bacteria passed through the membrane of the device because the pore size of the membrane was larger than the average bacteria size. In 0.4 and 1.0 μm-pore membranes, over 90 % of bacteria were captured. Considering the capture efficiency and flow rate, we decided to select the 1.0 μm-pore membrane for bacterial preconcentration. Next, we analyzed the capture efficiency at various bacterial concentrations to evaluate the clinical applicability. As expected, the time needed to finish concentrating the pathogens increases as a function of the bacterial concentration. Fig. 5.6a shows the flow rate of samples passing through the membranes at different bacterial concentrations. For bacterial concentrations of 10^1 to 10^3 CFU/mL, the sample volume increased linearly over time, meaning that the flow rate was constant. This means that the bacteria hardly affected the flow rate. However, the flow rate of the sample decreased after 150 seconds at 10^5 CFU/ml. This might be attributed to the bacteria captured on the membrane. A 1-ml bacterial suspension was collected after passing through the membranes of the device for quantification of capture efficiency. It was found that the capture efficiencies were more than 95% for bacterial concentrations from 10^1 to 10^5 CFU/ml (Fig. 5.6b). As shown in Fig. 5.7, *E. coli* were 1.8 ± 0.5 μm in length and 0.9 ± 0.3 μm in diameter.

We evaluated the porous membrane-based bacteria enrichment. From 1-ml of bacterial suspension at an initial concentration of 10^4 CFU/ml, all bacteria were trapped on the membrane. The final volume was calculated at a 0.025 μl assuming that the height was 2 μm. The enriched bacterial concentration was therefore calculated to be approximately 4×10^8 CFU/ml. This indicates that a 40,000-fold concentration enhancement can be achieved within 2 minutes (max. flow rate, $Q_{max} = 584$ μl /min) with more than 90 % capture efficiency.
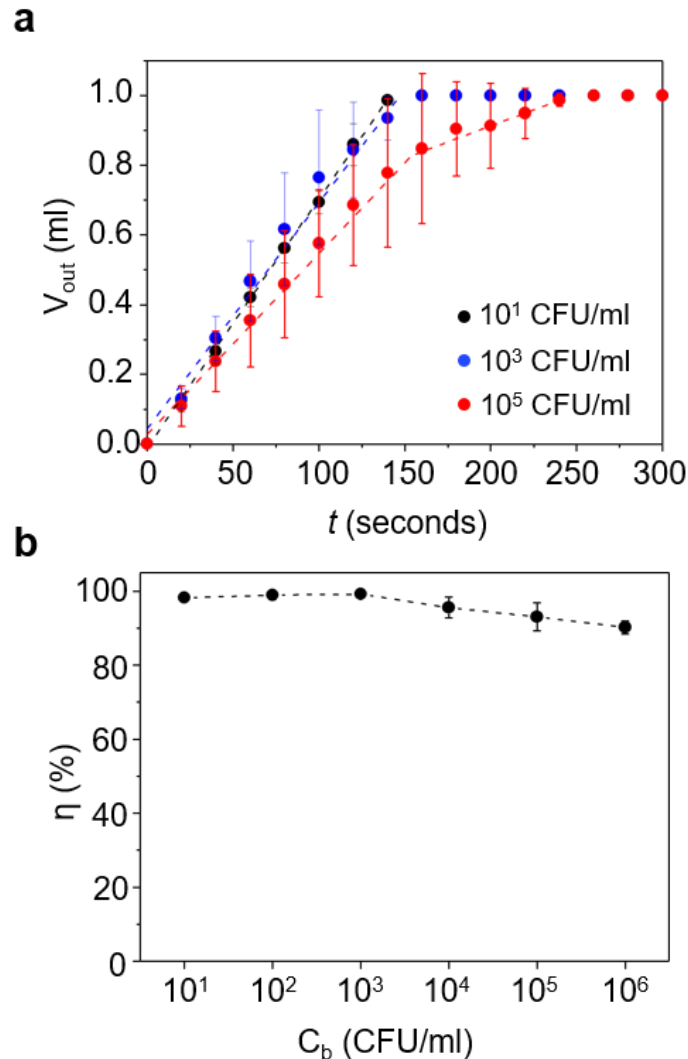
Figure 5.6 Characterization of flow rate and capture efficiency with different bacterial concentration. (a) The volume of sample passing through the membrane inside the chamber over time (rate of sample flow) with different bacterial concentrations. (b) The capture efficiency of *E. coli* with different bacterial concentrations.

5.6 RAPID PHOTOTHERMAL LYSIS OF PATHOGENIC BACTERIA FOR NUCLEIC ACID EXTRACTION

After pathogenic bacterial capture and preconcentration from the sample, cell lysis is necessary to release the nucleic acids into solution for further analysis[24]. After enrichment, we performed LED-driven photothermal lysis of *E. coli* in the same chamber (Fig. 5.8). We exploited Au-coated porous membranes not only as a bacterial concentrator, but also as a photothermal actuator. To analyze the temperature distribution of the chamber

with different heights, numerical simulations were performed using a commercial software (COMSOL Multiphysics). Figures 5.9a shows the temperature distribution of a chamber with a height of 300 μm when the temperature of the Au film reaches at 95°C. Even if the temperature is not uniform in the entire area of the detection chamber, the temperature was over 90 °C near the surface of the Au-coated membrane, where most of bacteria were captured. Thus, most of bacteria were photothermally lysed efficiently. Next, we characterized the light-to-heat conversion of the thin Au film. In Figure 5.9b, we plotted the time required to raise the temperature from 25°C (ambient temperature) to 55, 65, 75, 85, and 95°C with different optical powers from an LED. To analyze the results, conservation of energy was applied and the governing equation is expressed as follows:

$$mC_p \frac{\partial T}{\partial t} = Q_{abs} - Q_{ext} \tag{2}$$

, where m and C_p are the mass and the specific heat of components in the system, T is the temperature, t is the time, Q_{abs} is the energy of the Au film absorbed by the LED light, $Q_{abs} = I(1 - 10^{-A_\lambda})\eta$ (where I is the incident optical power from an LED, A_λ is the absorbance of the Au film, and η is the efficiency of light-to-thermal energy conversion), and Q_{ext} is the energy dissipated by the environment, $Q_{ext} = hS(T - T_{amb})$ (where h is a heat transfer coefficient, S is the cross-sectional area perpendicular to conduction, and T_{amb} is an ambient temperature). Equation 2 can be simplified using $\Theta = T - T_{amb}$,
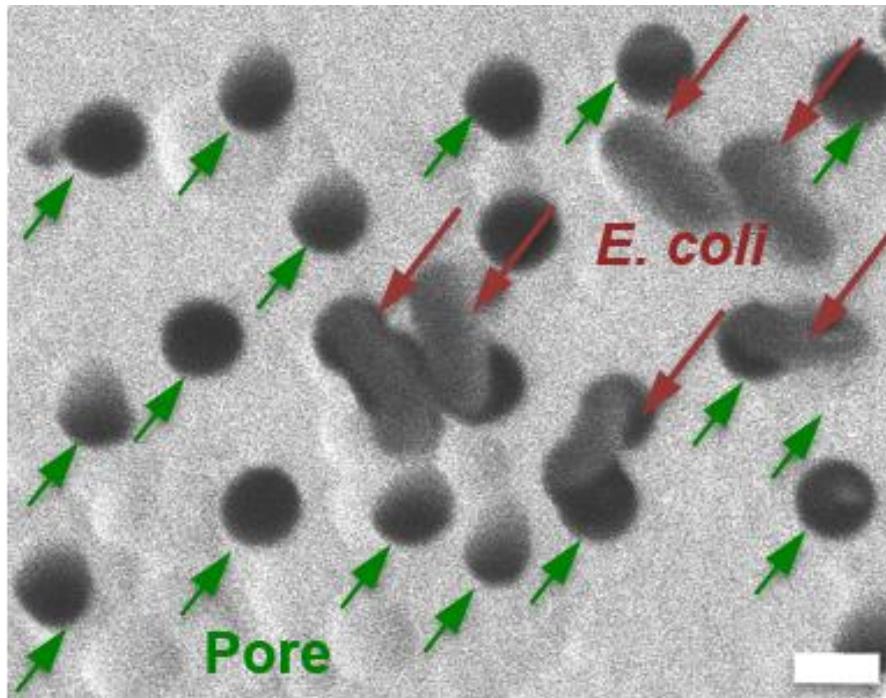

Figure 5.7 The SEM images of *E. coli* on the membrane (pore size: 1 μm). Scale bar is 1 μm.

$$\frac{d\theta}{dt} = aI + b\theta \qquad (3)$$

, where $a = \frac{(1-10^{-A\lambda})\eta}{mC_p}$ and $b = \frac{hS}{mC_p}$. The solution of Eq. (3) is expressed as $\theta = \frac{aI}{b}(1 - e^{-bt})$. Therefore, Eq. (3) can be reformed to $\frac{1}{I} = \frac{a}{b\theta}(1 - e^{-bt})$. The dashed lines in Fig. 5.9b are our model fitted to the data. Using the fitting equation, a and b are determined to be 8.716 and 0.03438 on average, respectively. Then, we investigated the efficiency of cell lysis on the Au-coated membranes with different optical powers of an LED. Figure 5.9c shows the measured temperature profiles of a cell suspension inside the chamber. The temperature inside the chamber could rise from 25°C (ambient temperature) to 95°C in only 15 seconds with an optical power of 0.75 W. Then, we examined the number of cells
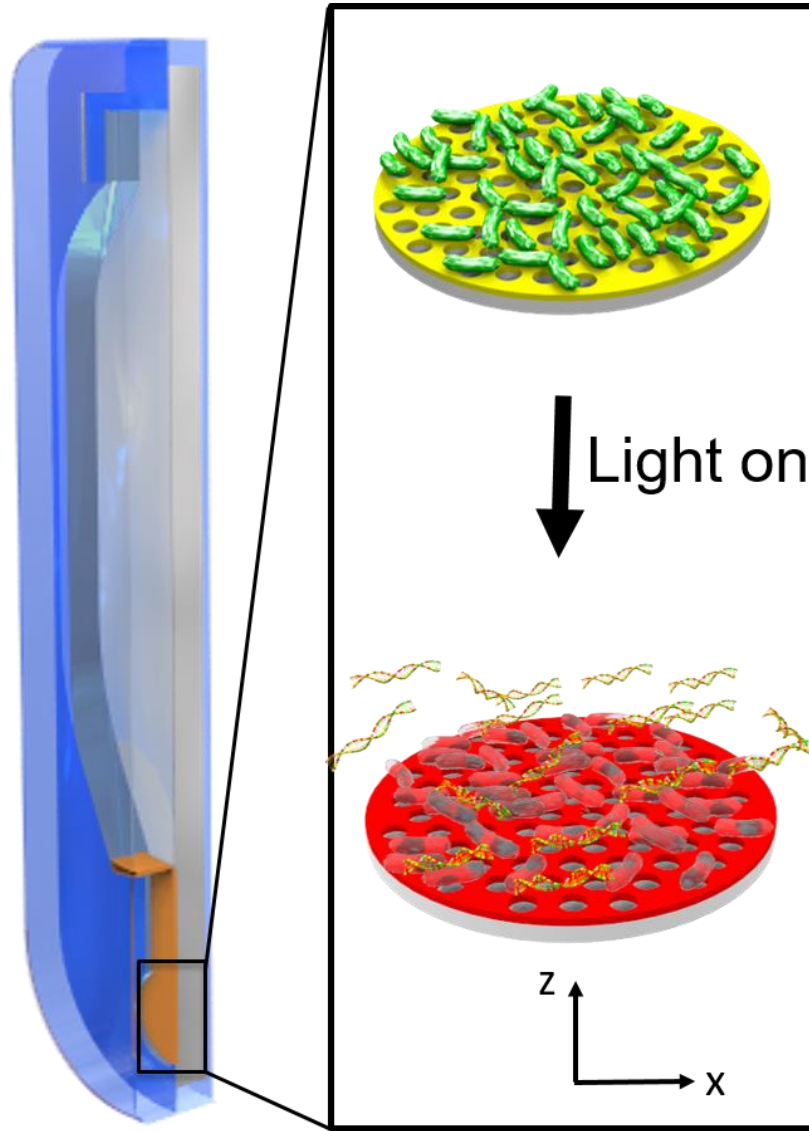

Figure 5.8 Schematic illustration of photothermal lysis of bacteria on the membrane.

lysed quantitatively. After irradiation with an LED (Fig. 5.9c), *E. coli* were stained with a fluorescent indicator for lysis efficiency quantification (Fig. 5.9d). As shown in Fig. 5.9d, only 17.5 % of *E. coli* were dead at an optical power of 0.149 W after irradiation for 2 minutes whereas 99.1 % of *E. coli* were dead after only 0.5 minutes of irradiation at 0.75 W. This demonstrates that cell viability can be significantly reduced with blue light exposure for only 0.5 minutes.
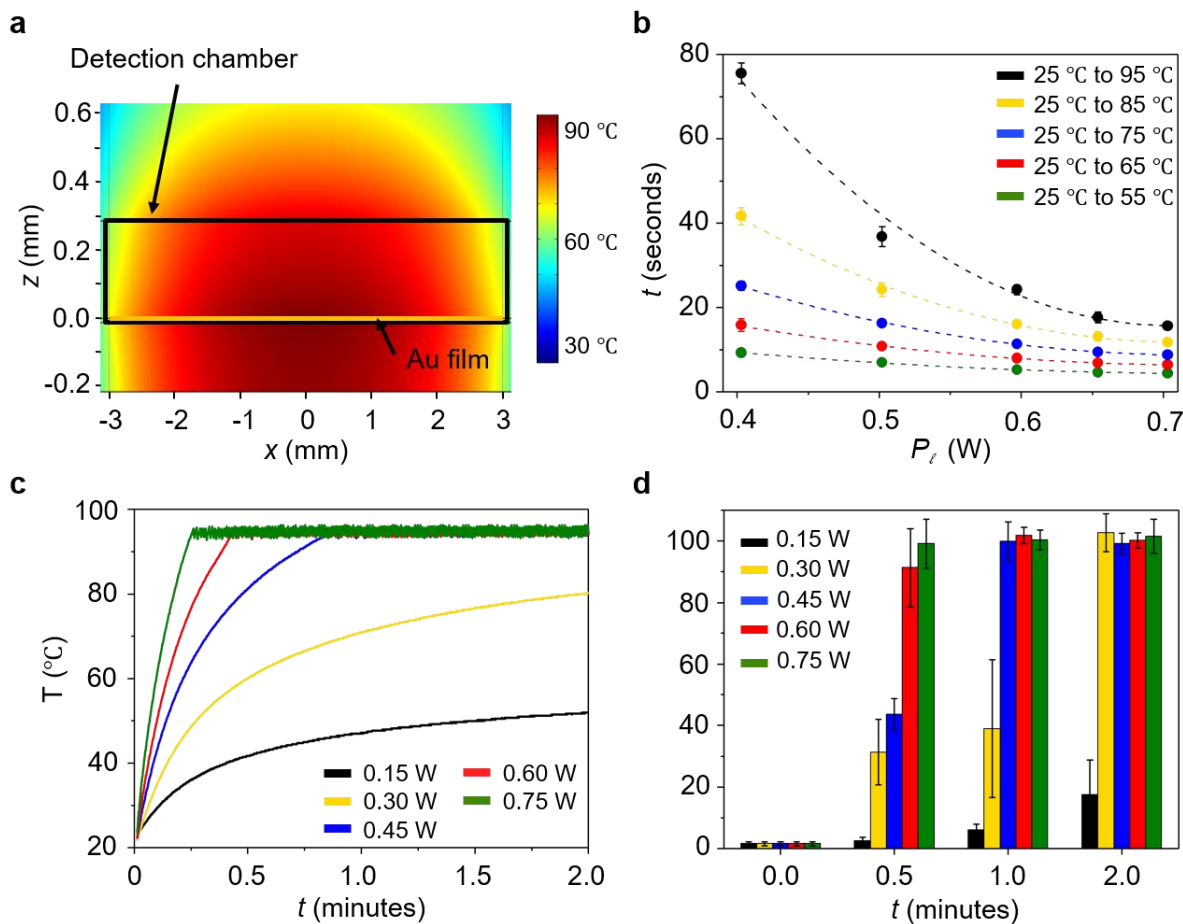

Figure 5.9 Characterization of photothermal lysis with the Au-coated membrane. (a) The calculated temperature distribution of the chamber and its surroundings when the temperature of the surface of Au-coated membrane reaches 95°C. (b) Relationship between optical power from an LED and the time required to raise the temperature inside the chamber. (c) The temperature profiles inside the chamber with different optical powers after turning on the LED. (d) Viability of E. coli after photothermal lysis over time.

5.7 ULTRAFAST LED-BASED QPCR FOR IDENTIFICATION OF *E. COLI*

Figure 5.10 illustrates the procedure of on-chip PCR. After enrichment of bacteria, PCR reagents are introduced into the device. Then, the back of the membrane is blocked with PCR sealing tape to prevent evaporation. Instead of using a laser, we resonate the frequency of plasmonic excitation of Au with a light emitting diode (LED) to reduce power consumption and cost for the photothermal lysis unit. Lastly, concentrated bacteria were photothermally lysed at 98°C for 3 minutes inside the chamber containing PCR reagents. Then, as shown in Fig. 5.11a, PCR thermocycles conducted at 98°C and 62°C for denaturation and annealing/extension over 40 cycles, respectively. We increased the lysis time up to 3 minutes to completely lyse the bacteria as well as to achieve initial denaturation of DNA. Due to the fast ramping rate of the LED-driven heating and dissipation during this initial stage, some overshoot and undershoot of the temperature occurred. We evaluated the temperature accuracy for photonic PCR that the denaturation temperatures were maintained in the range of 98 to 100.75, and the annealing/extension temperatures were 60 °C during thermocycles. The total PCR run time required was only 10 minutes for 40 cycles.

Next, we tested PCR amplification of whole bacteria with different bacterial concentrations. After whole processing such as bacteria capturing, photothermal lysis, PCR amplification of *E. coli* suspension, the identification of the amplified product was performed by gel electrophoresis as shown in Fig. 5.11b. We successfully detected bacteria with PCR on this system at concentrations as low as 10^3 CFU/ml. Compared to the results from a bench-top thermocycler (lane 8), the gel intensity of the specific band (Lane 1) from
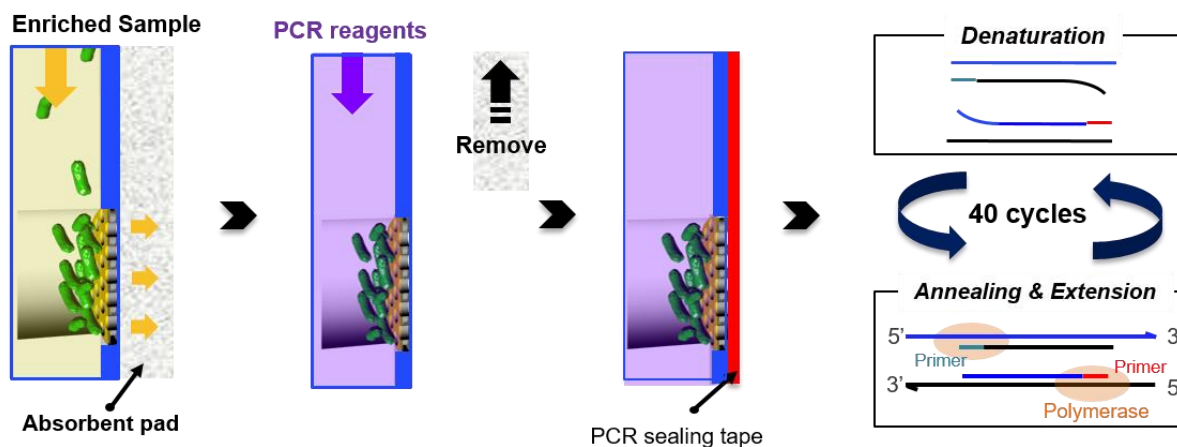

Figure 5.10 Schematics of steps for PCR: 1. Add sample. Bacteria are captured and concentrated on the membrane. 2. Remove absorbent pad and add PCR reagents. 3. Seal the back of the membrane using a PCR sealing tape. 4. Thermocycling by turning on and off a LED.
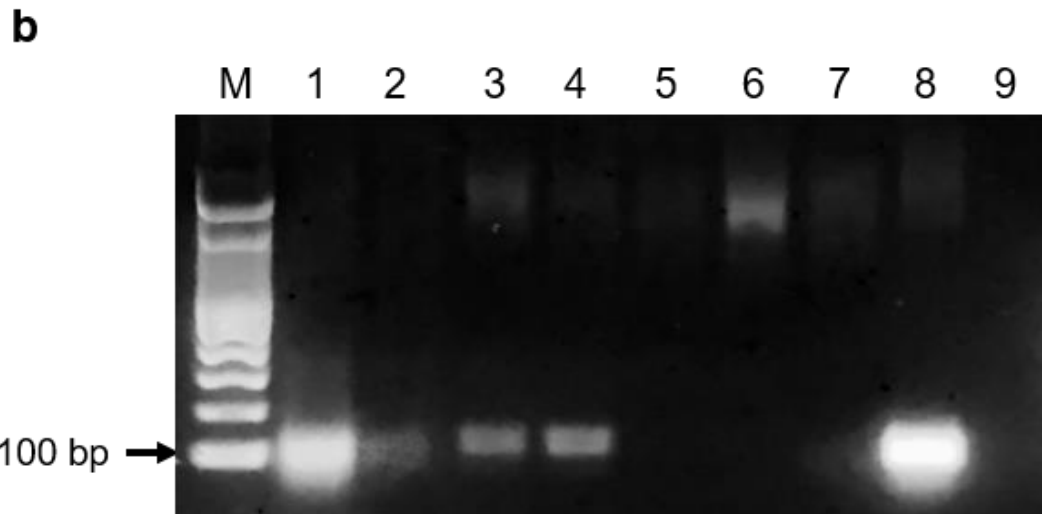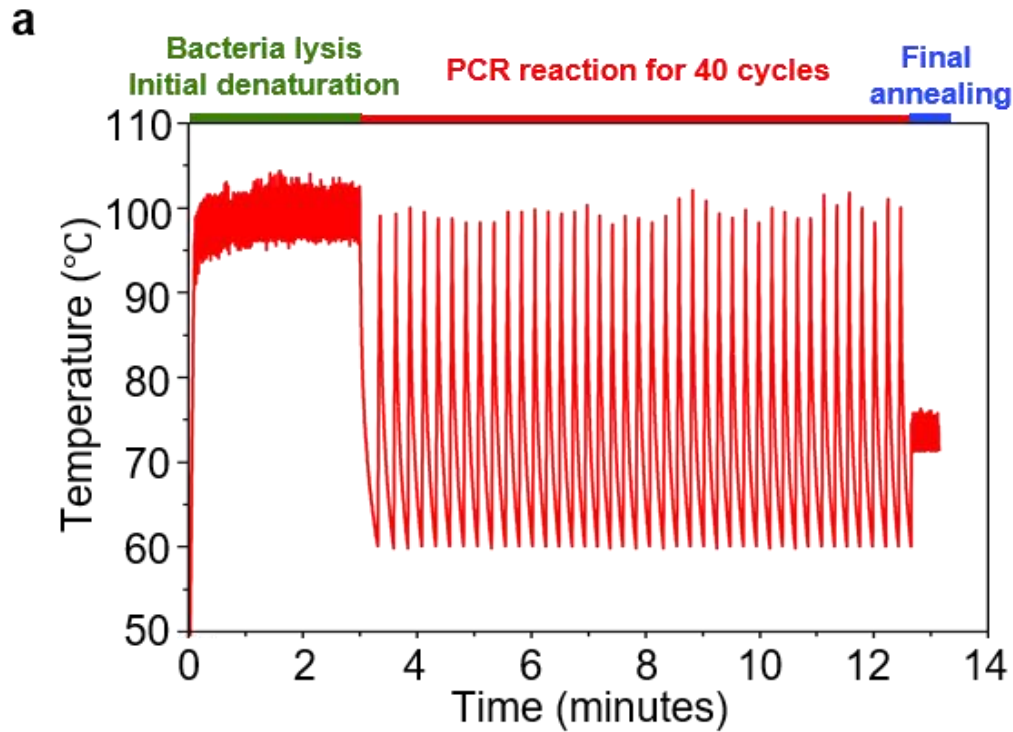
Figure 5.11 Characterization of performance of thermocycler in this platform. (a) The representative temperature profile for PCR. For the first 4 minutes, the temperature of PCR chamber in the platform is maintained at 98 ± 3 °C for complete bacterial lysis and initial denaturation of DNA. After 4 minutes, the thermal cycles were run: 95 ± 1.25°C for denaturation and 62 ± 0.25°C for annealing and extension. (b) Verification of PCR products of the platform by gel electrophoresis. Lane 1, 106 CFU/ml; Lane 2, 105 CFU/ml; Lane 3, 104 CFU/ml; Lane 4, 103 CFU/ml; Lane 5, 102 CFU/ml; Lane 6, 101 CFU/ml; Lane 7, 100 CFU/ml; Lane 8, Bench-top amplification (106 CFU/ml); Lane 9, negative control.

this system was lower, which might result from the lower amplification efficiency, which in turn was a result of the two-step (denaturation and annealing/extension) fast thermocycling. Then, we added 5 µl of 100x SYBR green dye in the device and took fluorescent images of the detection chamber after 0 to 40 cycles. The representative fluorescent images and their intensities are shown in Fig. 5.12. We will integrate a fluorescent detection module to detect the amplified product to complete this molecular diagnostic system for its ultimate application in POC settings.

5.8 CONCLUSION

We have demonstrated a rapid molecular diagnostic system that takes less than 15 minutes from sample to answer. Our integrated molecular diagnostic system allows autonomous sample enrichment (2 min), on-site photothermal lysing and initial denaturation (3 min), and NA amplification 10 min) in a single platform. The Au-coated porous membrane played two critical roles: a concentrator of pathogen on the membrane, and a photothermal converter. From a relatively large volume of urine sample (1 ml), a 40,000-fold increase in bacterial concentration was achieved within 2 minutes with >90 % capture efficiency. Using ultrafast and highly efficient light-to-heat conversion of Au, bacteria on the membranes were photothermally lysed in 1 minute. By turning on and off a LED, photonic PCR was performed on the membrane to detect pathogens. To validate this system, the detection of *E. coli* at 10^3 CFU/ml was demonstrated. This simple and integrated system will be a good candidate for POC diagnostics. Future work will focus on the integration of fluorescent detection modules, i.e. smartphone detection, into this system.
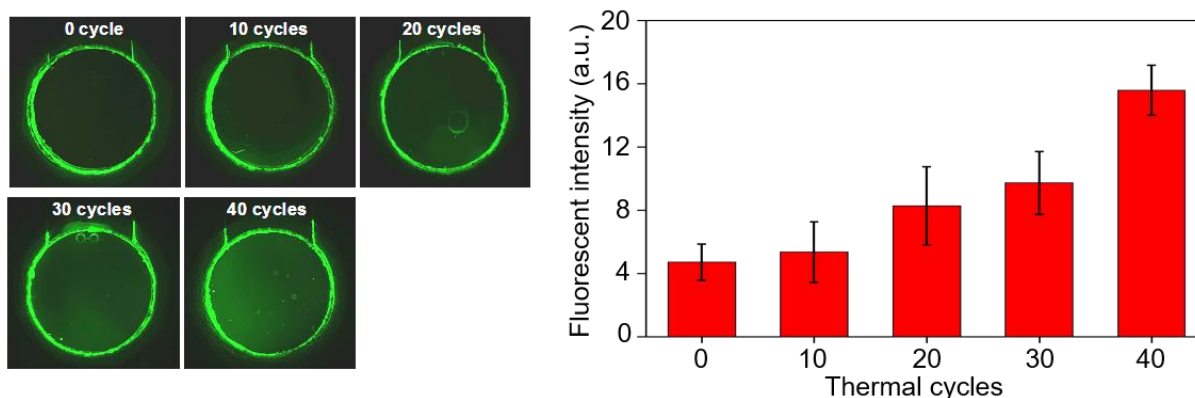

Figure 5.12 Florescent images (left images) and fluorescent intensity (right figure) of the detection chambers after PCR amplification from 0 cycle to 40 cycles after adding SYBR green dye. Bacterial concentration was 104 CFU/ml.

5.9 REFERENCES

1. Marquet, K., Liesenborgs, A., Bergs, J., Vleugels, A. & Claes, N. Incidence and outcome of inappropriate in-hospital empiric antibiotics for severe infection: a systematic review and meta-analysis. Crit. Care 19, 63 (2015).

2. Laxminarayan, R. et al. Antimicrobials: access and sustainable eff ectiveness 1 Access to eff ective antimicrobials: a worldwide challenge. Ser. 168 www.thelancet.com 387, (2016).

3. Schappert, S. M. & Rechtsteiner, E. A. Ambulatory medical care utilization estimates for 2007. Vital Health Stat. 13. 13, 1–38 (2011).

4. Flores-Mireles, A. L., Walker, J. N., Caparon, M. & Hultgren, S. J. Urinary tract infections: epidemiology, mechanisms of infection and treatment options. Nat. Rev. Microbiol. 13, 269–284 (2015).

5. Nielubowicz, G. R. & Mobley, H. L. T. Host-pathogen interactions in urinary tract infection. Nat. Rev. Urol. 7, 430–441 (2010).

6. Foxman, B., Barlow, R., D'Arcy, H., Gillespie, B. & Sobel, J. D. Urinary tract infection: Self-reported incidence and associated costs. Ann. Epidemiol. 10, 509–515 (2000).

7. Kerremans, J. J. et al. Rapid identification and antimicrobial susceptibility testing reduce antibiotic use and accelerate pathogen-directed antibiotic use. J. Antimicrob. Chemother. 61, 428–435 (2008).

8. Wang, S. et al. Portable microfluidic chip for detection of Escherichia coli in produce and blood. Int. J. Nanomedicine 7, 2591–2600 (2012).

9. Leekha, S., Terrell, C. L. & Edson, R. S. General principles of antimicrobial therapy. Mayo Clin. Proc. 86, 156–67 (2011).

10. Lafleur, L. et al. A rapid, instrument-free, sample-to-result nucleic acid amplification test. Lab Chip 52, 3377–3383 (2016).

11. Pai, N. P., Vadnais, C., Denkinger, C., Engel, N. & Pai, M. Point-of-Care Testing for Infectious Diseases: Diversity, Complexity, and Barriers in Low- And Middle-Income Countries. PLoS Med. 9, (2012).

12. Patel, H. D., Livsey, S. A., Swann, R. A. & Bukhari, S. S. Can urine dipstick testing for urinary tract infection at point of care reduce laboratory workload? J Clin Pathol 58, 951–954 (2005).

13. Kulpakko, J., Kopra, K. & Hänninen, P. Time-resolved fluorescence-based assay for rapid detection of Escherichia coli. Anal. Biochem. 470, 1–6 (2015).

14. Ferreira, L. et al. Direct identification of urinary tract pathogens from urine samples by matrix-assisted laser desorption ionization-time of flight mass spectrometry. J Clin Microbiol 48, 2110–2115 (2010).

15. Schröder, U. C. et al. Rapid, culture-independent, optical diagnostics of centrifugally captured bacteria from urine samples. Biomicrofluidics 9, (2015).

16. Cho, S., Park, T. S., Nahapetian, T. G. & Yoon, J.-Y. Smartphone-based, sensitive microPAD detection of urinary tract infection and gonorrhea. Biosens. Bioelectron. 74, 601–611 (2015).

17. Ahmad, F. & Hashsham, S. a. Miniaturized nucleic acid amplification systems for rapid and point-of-care diagnostics: A review. Anal. Chim. Acta 733, 1–15 (2012).

18. Zhang, C. & Xing, D. Miniaturized PCR chips for nucleic acid amplification and analysis: Latest advances and future trends. Nucleic Acids Res. 35, 4223–4237 (2007).

19. Czilwik, G. et al. An integrated lab-on-a-chip system with DNA extraction, pre- and main PCR amplification for automated detection of low concentrated pathogens. in Proceedings of the 17th conference on miniaturized systems for chemistry and life science 1607–1609 (2013).

20. Cai, D., Xiao, M., Xu, P., Xu, Y. & Du, W. An Integrated Microfluidic Device Utilizing Dielectrophoresis and Multiplex Array PCR for Point-of-Care Detection of Pathogens. Lab Chip 14, 3917–3924 (2014).

21. Angus, S. V., Cho, S., Harshman, D. K., Song, J. Y. & Yoon, J. Y. A portable, shock-proof, surface-heated droplet PCR system for Escherichia coli detection. Biosens. Bioelectron. 74, 360–368 (2015).

22. Park, K. S. et al. Rapid identification of health care-associated infections with an integrated fluorescence anisotropy system. Sci. Adv. 2, e1600300–e1600300 (2016).

23. S. Ravindra , Y. Murali Mohan , K. Varaprasad , N. Narayana Reddy, K. V. & Raju, & K. M. Surfactant-Modified Poly(acrylamide-coacrylamido propane sulphonic acid) Hydrogels. Int. J. Polym. Mater. Polym. Biomater. 58, 278–296 (2009).

24. Niemz, A., Ferguson, T. M. & Boyle, D. S. Point-of-care nucleic acid testing for infectious diseases. Trends in Biotechnology 29, 240–250 (2011).

CHAPTER 6

CONCLUSIONS

6.1 CONCLUSION

This dissertation describes an effort to develop the noble microfluidic-based components for molecular diagnostic platform at point-of-care (POC) setting. In Chapter 1, a review of the current state of point-of-care microfluidic molecular diagnostic is summarized. Even though the advancement of microfluidic molecular diagnostic techniques have been achieved, only few of commercialized microfluidic POC molecular diagnostics platforms have been launched. That is mainly because of complicated sample preparation, high power consumption, and expensive reagents. Hence, this dissertation focused on the development of components to solve these problems. In Chapter 2, a microfluidic device with porous materials for sample preparation was extensively studied. First of all, theoretical analysis of flow with a porous wall in a microchannel provided the distribution of bacteria with flow velocity profiles. Using porous materials and a 3D microfluidic device, bacteria could be enriched and selectively captured on the antibody-mediated porous materials from whole blood. In addition, chemical or photothermal method enabled to lyse bacteria on a chip for further analysis. In Chapter 3, a new thermocycling method, called "photonic PCR", was introduced. Gold (Au) absorbs a blue light efficiently and converts light energy into heat energy rapidly. Using this principle, we developed a simple thermocycler including only thin Au film, plastic, and a single LED. Furthermore, in Chapter 4, comprehensive theoretical analysis of heat transfer model in the photonic PCR. Generally, in photonic PCR, the total time of thermal cycles mainly depends on cooling cycles. Absorption of Au affects not only the heating ramping rate but also the cooling ramping rate of photonic PCR system. Furthermore, the lower thermal diffusivity of materials in the system, the steeper the temperature gradient at the interface between the PCR chamber and its surroundings, which increases the cooling ramping rate of the system. Finally, in Chapter 5, the integrated molecular diagnostic platform was developed for uropathogenic diagnostics. Absorbent pad unnecessitated the external equipment for generating flow in microchannel. Total analytic time was only 15 minutes from a sample to its result with 10^3 CFU/ml detection limit. Multiplex analysis and portable fluorescent detection system should be developed in the future.

In summary, my research during PhD program allowed me to study on a variety of topics towards the development of microfluidic POC platforms. I believe that POC diagnostic platforms open a new chapter of personalized health care and revolutionize

global health. I am thankful to my advisor, lab members and collaborators for supporting my research and intend to continue a multi-disciplinary research for global health.